The Effect of Tidal Interactions On Hot Subdwarf B Stars and Their Pulsations

Holly Preece

Supervisors: Prof. Christopher A. Tout & Prof. C. Simon Jeffery

Institute of Astronomy, University of Cambridge
Armagh Observatory & Planetarium

This dissertation is submitted for the degree of

Doctor of Philosophy

Churchill College

July 2019

Declaration

I hereby declare that, except where specific reference is made to the work of others, the contents of this dissertation are original and have not been submitted in whole or in part for consideration for any other degree or qualification in this, or any other University. This dissertation is the result of my own work and includes nothing which is the outcome of work done in collaboration, except where specifically indicated in the text. Those parts of the dissertation which have been published or accepted for publication are as follows.

- The results from section 2.3 were incorporated into the binary_c code and used for Izzard, R. G, Preece, H., Jofre, P., Halabi, G. M., Masseron, T., and Tout, C. A. (2018). Binary stars in the Galactic thick disc. MNRAS, 473:2984–2999

- Chapter 3 is Preece, H. P., Tout, C. A., and Jeffery, C. S. (2018). Tidal Interactions of Close Hot Subdwarf Binaries. MNRAS, 481:715–726.

- Chapter 4 is Preece, H. P., Tout, C. A., and Jeffery, C. S. (2019). Convection physics and tidal synchronization of the subdwarf binary NY Virginis. MNRAS, 485(2):2889–2894.

- Chapter 5 is Preece, H. P., Jeffery, C. S., and Tout, C. A. (2019a). Asteroseismology of tidally distorted sdB stars. MNRAS, 489(3):3066–3072.

This dissertation contains fewer than 60,000 words including appendices, bibliography, footnotes, tables and equations and has fewer than 150 figures.

Holly Preece
July 2019

Acknowledgements

Dedicated to all those who have supported me over the years. I couldn't have done it without you.
My supervisors Christopher Tout and Simon Jeffery for their support, patience and expertise.
My chosen family Charlie, Debi and Sheh for never being further away than a phone call.
My endless family for their endless encouragement Nicky, Dad, Mum, Charlie, Max, Florence, Miranda, Asher, Granny, John, Granddad, Fiona, Bone, Andy, Greg, Julia, Grandma, Robert, Elizabeth, Tracy, Kevin, Bob, Sheron, Danielle, Scott, Clare, Alex, Alex, Alice, Robin, Laura, Mark, Paul, Lynette, Aunty Marggie and Uncle John.
The Dublin crazies for keeping me sane Alex, Iarla and Eoin, Melodie, Andrew, Sean, Sammie, Luka, Noemi, Roko, Petra, Dino, Mirko, Manon, Siofra, Rolf, Monica, Kevin, Mate, Brian, Szandi, Andris, Tammi, Jacob, Barbi, Sasha, Chriostóir, Oggy, Darran, Charlie, Chloe, Hannah, James, Ste, Avril, Steve, Niamh, Crosby, Irene, Renan, Marko, Knives, Adz, Sue, Erin, Sinead, Sisco, Bruna.
My many, many friends for the great conversations and great times, some of which I even remember! Josh, Sarah, Mark, Jen, Jimmy, James, Luca F., Tim, Loren, Rob, Dean, Otis, Andrew, Glen, Tom, Cat, Aliss, Colin the Night Porter, Alex, Lucy, Nalini, Steve, Clara, Sam, Edward, Vinicius, Tom A., Jack, Lucy, Janosz, Mia, Marti, Suzannah, Freya, Jannat, Angela, Tom, Ellen, Ben, Arthur, Christian, Ninon, Akshath, Max, Julie, Fabien, Thiago, Sacha, Chiara, Vivek, Malavika, Jay, Alex, Alice, Josh, Tilly, Max, Matt, Joanna, Sophie, Julie.
My colleagues Rob, Ghina, Anna, Sverre, Phil, Elliot, Tom, Simon and Matt for their insights.
My fellow astronomy PhD students for making sure I didn't work too hard Sid (The Gandhinator), Cameron, Adam, Andy, Aneesh, Laura, Pablo, Tom W., Erin, Lauren, Phil, Pamela, Yanina, Conor, Rok.
Churchill College Boat Club for teaching me that 6am can be a time for waking up, not just going to bed Kathryn, George, Beth, Xanthe, Karen, Vicky, Katy, Fan, Kluane, Katie, Giorgio, Gabi, Lizzie, Elre, Katie-Lou, Elizabeth, Jeanie, Alexis, Blake, Ffion, Danny and Oscar.
To Silvia Breu for believing in me even when I didn't believe in myself.
Paul Hewitt, Vasily Belokurov, Debbie Peterson, Nikku Madhusudhan, Barry Kingston and Rebecca Swalmeh for helping me get back up when gravity had other ideas.
Addenbrooks Hospital, Brookfields Community Dentist and Regent's Street Dental Practice for putting my face back together and making sure I still had a smile.

“It was the best of times, it was the worst of times, it was the age of wisdom, it was the age of foolishness, it was the epoch of belief, it was the epoch of incredulity, it was the season of Light, it was the season of Darkness, it was the spring of hope, it was the winter of despair, we had everything before us, we had nothing before us, we were all going direct to Heaven, we were all going direct the other way...
It is a far, far better thing that I do than I have ever done; it is a far, far better rest that I go to than I have ever known."

– Charles Dickens, *A Tale of Two Cities*

Abstract

Hot subdwarf B (sdB) stars are evolved core He-burning stars. The sdBs are formed by binary interactions on the red giant branch (RGB) which cause the stars to lose most of their H envelopes. Over half of all observed hot subdwarf B stars are found in binaries, many of which are found in close configurations with orbital periods of 10 d or less. These short period systems are formed by common envelope evolution.

In order to estimate the companion masses in these predominantly single-lined systems, tidal locking has frequently been assumed for sdB binaries with periods less than half a day. Observed non-synchronicity of a number of close sdB binaries challenges that assumption and hence provides an ideal testbed for tidal theory. The stars have convective cores and radiative envelopes. Tidal dissipation in such systems is not particularly well understood. We solve the second-order differential equations for detailed 1D stellar models of sdB stars to obtain the tidal dissipation strength and hence to estimate the tidal synchronization time-scale owing to Zahn's dynamical tide and the equilibrium tide. The results indicate synchronization time-scales longer than the sdB lifetime in all observed cases using standard input physics.

Asteroseismological analysis of NY Vir suggests that at least the outer 55 per cent of the star (in radius) rotates as a solid body and is tidally synchronized to the orbit. Detailed calculation of tidal dissipation rates in NY Vir fails to account for this synchronization. Recent observations of He core burning stars suggest that the extent of the convective core may be substantially larger than that predicted with theoretical models. We conduct a parametric investigation of sdB models generated with the Cambridge STARS code to artificially extend the radial extent of the convective core. These models with extended cores still fail to account for the synchronization. Tidal synchronization may be achievable with a non-MLT treatment of convection.

Several sdB stars have been both predicted and observed to pulsate with multiple frequencies. Asteroseismological analysis of the observed pulsations shows that they do not quite fit with the theoretical models, especially in the close binary systems. We present a method for computing tidal distortion and associated frequency shifts. Validation is by application to polytropes and comparison with previous work. For typical sdB stars, a tidal distortion of less than 1% is obtained for orbital periods greater than 0.1 d. Application to numerical helium

core-burning stars identifies the period and mass-ratio domain where tidal frequency shifts become significant and quantifies those shifts in terms of binary properties and pulsation modes. Tidal shifts disrupt the symmetric form of rotationally split multiplets by introducing an asymmetric offset to modes. Tides do not affect the total spread of a rotationally split mode unless the stars are rotating sufficiently slowly that the rotational splitting is smaller than the tidal splitting.

Table of contents

Chapter 1

Introduction

A star is an object which is bound by its own gravity and radiates energy from an internal source. For most of their life they have nuclear fusion reactions in their inner regions which generate large amounts of energy. Typically, the energy is transported from the inner regions to the surface where it is radiated away. During the life of a star its chemical composition and structural properties undergo substantial changes. The nuclear reactions change the composition of the star and ultimately the composition of the universe. The majority of stars form near to other stars and reside in binaries, triples or higher order multiples. Interactions with a companion can significantly alter the evolution of a star and create exotic objects such as hot subdwarf B (sdB) stars. Furthermore, a closely orbiting companion raises a tide in the star and distorts its structure. The internal structure of stars can be explored with asteroseismology. This dissertation explores the effect of tidal interactions on the properties of sdB stars.

1.1 Stellar Evolution

Stars are formed when clouds of interstellar molecular hydrogen gas collapse under the influence of gravity to form clusters. The fully convective protostars dynamically contract to become pre-main-sequence objects. During the contraction the internal temperature of a star increases and the luminosity and opacity both decrease. Deuterium burning commences which converts H and ^{2}H into ^{3}He. This reaction is highly sensitive to the temperature and hence drives a convective core. When the core reaches 10^7 K hydrogen burning begins in full. Stars with masses less than $1.1\,\mathrm{M}_\odot$ burn hydrogen via the p-p chain in radiative cores. More massive stars complete hydrogen fusion via the CNO cycle in convective cores. Once the hydrogen burning is in equilibrium stars are said to be zero-age main-sequence (ZAMS) stars. The minimum mass for a ZAMS star is $0.08\,\mathrm{M}_\odot$ at solar metallicity (Burrows et al., 1997; Fernandes et al., 2019). Stars below this mass threshold are brown dwarfs. The main-sequence phase is extremely stable and is the evolutionary stage in which stars spend most of their lifetimes.

At the terminal-age main sequence (TAMS) central hydrogen reserves are fully depleted and hydrogen burning continues in a shell which moves radially out. The inert He core contracts which increases the central temperature and density. Meanwhile, the outer regions cool and expand. The stars are now red giants. On the red giant branch (RGB) first dredge up occurs. During first dredge up the envelope becomes convective and deepens mixing some of the internal material, which has previously been hydrogen burning, to the surface of the star. The outer regions of the RGB star are less tightly bound than they have been in previous evolutionary phases so the outer layers of the star are be blown away by stellar wind.

Stars with masses below $0.5\,M_\odot$ never reach the central conditions required to commence He fusion and instead settle on to a white dwarf cooling track where they steadily cool and condense to become low-mass He white dwarfs. Stars with masses between 0.5 and $2.25\,M_\odot$ have electron degenerate cores which explosively ignite He in a process called the He flash. The degeneracy of the inner material is lifted during the He flash. The stars become so-called red clump stars which has a core fusing He into C and O and a H shell burning region outside the core. If enough of the envelope is lost on the RGB the stars become extreme horizontal branch stars. Higher mass stars have non-degenerate cores which stably ignite He.

Once central He resources are fully depleted, in either the degenerate and non-degenerate ignition scenario, objects become asymptotic giant branch (AGB) stars. AGB stars have both He and H shell burning. Stars with masses below $6\,M_\odot$ do not reach central conditions to ignite carbon and so form C/O white dwarfs. Stars with masses between 6 and $9\,M_\odot$ ignite carbon which burns into neon and magnesium then become oxygen-neon white dwarfs.

The high mass stars with masses over $9\,M_\odot$ continue fusing elements until an iron or nickel core is formed. Shell burning of previous core elements continues. Once the Fe/Ni core is formed there are no further elements for which nuclear fusion is energetically profitable and so their cores collapse and the stars violently explode in the spectacular Type II supernovae. The stellar remnants are either neutron stars or black holes.

1.1.1 Stellar Variability

Variable stars have observed brightnesses which change on time-scales significantly shorter than major evolutionary changes. These changes in brightness can be intrinsic or extrinsic. Intrinsic variables change brightness owing to internal physical changes whereas extrinsic variables require some external influence. Eclipsing binaries are an example of extrinsic variables because the source of the change in their observed light output is the stars physically passing in front of one another. Ellipsoidal variables are stars which have been deformed by tidal interactions and are another example of an extrinsic variable. The photometric lightcurves of ellipsoidal variable stars are approximately sinusoidal owing to their non-spherical shapes in circular orbits. Pulsating stars are a class of intrinsic variables whose changes in luminosity are due to periodic distortions to their shapes and sizes. These modifications to the structure cause heating and cooling which is responsible for the variability on the surface.

1.1.2 Binary Interactions

If stars form sufficiently close to one another they may form binaries, triples or higher order systems. These stars are gravitationally bound to one another in elliptical orbits. The multiplicity fraction of stars is strongly dependent on the mass of the primary. Higher mass stars are far more likely to be in binaries. About 80% of O stars are in binary or higher order systems and have 1.3 companions on average. Meanwhile, only 20% of M type stars are in multiples (Duchêne and Kraus, 2013; Moe and Di Stefano, 2017). If they are sufficiently close, the stars are said to be interacting. Binary-star interactions can have a significant effect upon the evolution of stars. One of the major things that happens in the interacting regime is mass transfer between the objects. Tidal interactions cause the stars to become deformed from their spherically symmetric shape. Tides also alter the orbit and spin properties of a system.

Roche Model of Binary Evolution

Roche models define a critical potential surface called a Roche lobe, of effective radius R_{L}, for each star in a binary configuration. Outside the Roche lobe material is no longer gravitationally bound to the star. The effective radius of a Roche lobe is such that its volume $V_{\mathrm{L}} = \frac{4}{3}\pi R_{\mathrm{L}}^3$ and can be approximated (Eggleton, 1983) as

$$r_{\mathrm{L}}(q) = \frac{R_{\mathrm{L}}}{a} = \frac{0.49\,q^{2/3}}{0.6\,q^{2/3} + \ln(1+q^{1/3})}, \tag{1.1}$$

where a is the separation of the two stars. The mass ratio of the stars is denoted by q which is defined as m_1/m_2, with m_1 and m_2 labelling the primary and its secondary companion star respectively. Once a star overflows its Roche lobe mass is no longer bound and can be accreted onto the companion star. Figure 1.1 shows mass transfer from a main-sequence star to its white dwarf companion via RLOF. There are four major cases of mass transfer between binary stars. Case A mass transfer begins on the main-sequence. Early case B mass transfer occurs as the star crosses the Hertzsprung Gap whereas late case B mass transfer is on the RGB. Case C mass transfer begins after He ignition.

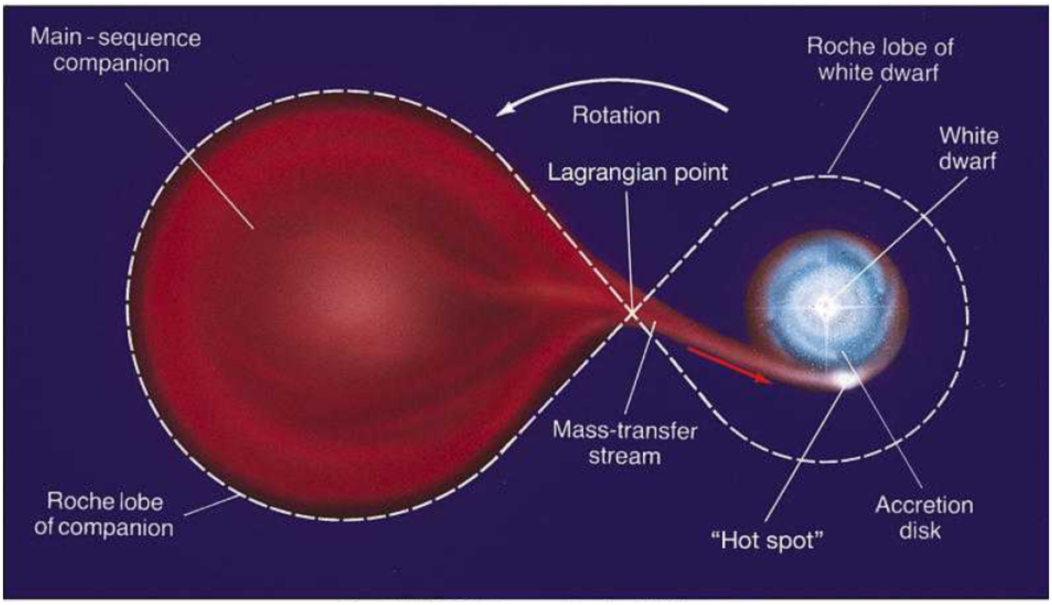

Fig. 1.1 Roche Lobe overflow and mass transfer from the more massive main-sequence companion to the white dwarf with the formation of an accretion disc. The Lagrangian point is where the mass transfers from one object to the other. Image from http://coffee.ncat.edu:8080/Flurchick/Lectures/StellarModeling/Section1/Lecture1-6.html

1.2 Hot Subdwarf B Stars

The sdB stars are extreme horizontal branch (EHB) stars which are formed by binary interactions. The sdBs are hot, with effective temperatures between 20000 and 40000 K. They are also subluminous so sit below the main sequence with luminosities of the order $10\,L_\odot$ (Heber, 2016). The objects are small, with canonical masses of $0.47\,M_\odot$ and radii between 0.1 and $0.25\,R_\odot$. With such small radii, the objects are compact with surface gravities in the range $5.0 < \log_{10}(g_{\rm surf}/{\rm cm\,s^{-2}}) < 6.0$ whereas for the Sun $\log_{10}(g_{\rm surf}/{\rm cm\,s^{-2}}) = 4.44$. They are evolved and so have He burning cores (distributed about $0.45\ M_\odot$) and have H-rich envelopes with masses less than $0.02\ M_\odot$. Binary interactions on the RGB are responsible for the loss of the H envelope. Figure 1.2 shows the position of sdBs in the Hertzsprung-Russell (HR) diagram.

A small number of sdB stars were first discovered at high Galactic latitudes in the 1950s in the photometric survey of the North Galactic Pole carried out by Humason and Zwicky (1947). Many more sdBs have since been discovered with large photometric surveys including the work of Greenstein and Sargent (1974) and the Palomar-Green survey in the 1980s (Green et al., 1986). They are generally the dominant objects in surveys searching for faint blue objects at the Galactic level.

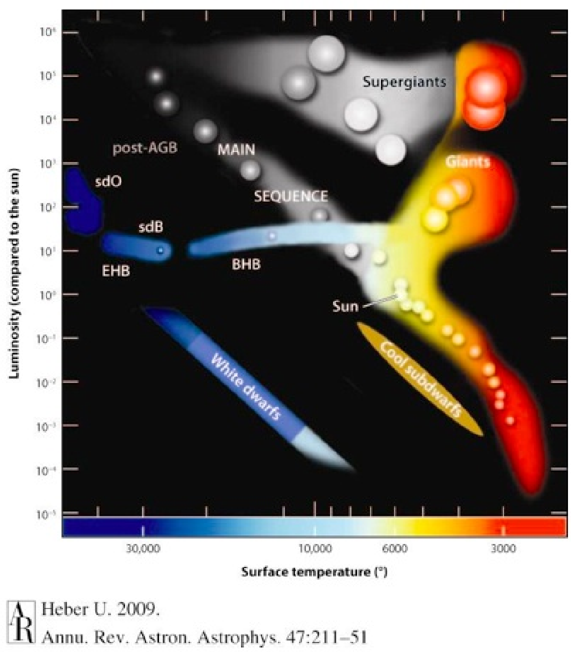

Fig. 1.2 Hertzsprung Russel diagram showing the main evolutionary phases of stars including the location of sdBs on the extreme horizontal branch (Heber, 2009)

Whilst formed by binary evolution channels the sdB stars can be single or binary with an observed binary fraction of 51% (Edelmann et al., 2005). The sdBs with white dwarf or low-mass main-sequence unseen companions are single lined spectroscopic binaries and those with G/K main-sequence companions are double lined. Many sdB binaries are close, in short orbital period configurations with $P_{\mathrm{orb}} < 10\,\mathrm{d}$, (Copperwheat et al., 2011) which would suggest that tidal interactions could be significant.

Historically it has often been assumed that any sdB with white dwarf or dM companion and orbital period of less than half a day was in synchronous rotation (Geier et al., 2010; Maxted et al., 2002). A synchronously rotating system has a spin period which is is the same as the orbital period. If the surface gravity and the rotational velocity in the line of sight are known the orbital elements can then be solved. This is usually only possible for double line spectroscopic binaries. The sdBs are also predicted and observed to pulsate. Recent asteroseismological analysis has shown that the assumption of tidal locking is incorrect in many cases (Kawaler et al., 2010; Pablo et al., 2012a,b).

1.2.1 Formation of sdB Stars

One of the earliest questions regarding sdBs was how these core He-burning stars initially lost their envelopes. Current stellar wind prescriptions alone cannot remove the required quantity of the envelope quickly enough. Many sdBs are observed to be in binaries. Mass transfer between the two stars, either by stable Roche Lobe Overflow (RLOF) or common envelope ejection, provides a mechanism to remove the envelope of a red giant (Han et al., 2002). The existence of slowly rotating single sdBs are more difficult to explain. The merging of two low-mass He white dwarfs (Han et al., 2002; Zhang and Jeffery, 2012) or a He white dwarf with a low-mass main-sequence star (Clausen and Wade, 2011) have been suggested. Merger products from either channel are expected have a broad mass distribution however asteroseismic measurements indicate that the masses of single sdB stars are peaked at the canonical mass of $0.47\,\mathrm{M}_\odot$ (Fontaine et al., 2012).

Stable Roche Lobe Overflow

The stable Roche lobe overflow channel is the simplest mechanism for sdB formation. The sdBs produced in this manner are in wide binaries with long orbital periods, between 400 and 1500 d. They have thick H-rich envelopes and a mass distribution peaked around $0.46\,\mathrm{M}_\odot$. The companions can be high mass white dwarfs or G/K main-sequence stars and are more massive than the sdB progenitor. The mass transfer is assumed to be non-conservative and mass lost from the system carries away orbital angular momentum. The mass loss occurs on the nuclear time-scale so thermal and hydrodynamic equilibrium are maintained. Mass transfer begins on the red giant branch (RGB) when a low-mass giant fills its Roche lobe. It is driven by the gradual expansion of the donor star owing to the burning of its fuel (Kuiper, 1941). As the star's Roche lobe overflows mass is transferred and the binary orbit widens causing mass transfer to be temporarily halted. The star continues to expand so it's Roche Lobe overflows again which restarts the mass transfer. Mass transfer stops once the H-rich envelope is depleted to the extent that the star begins to shrink of its own accord. The degenerate core ignites in a He-flash shortly after the mass loss is quenched if the mass of the core is sufficiently large. Han et al. (2002) demonstrated that progenitor stars between 0.8 and $1.6\,\mathrm{M}_{\odot}$ can experience dynamically stable mass transfer and form an sdB star. Vos et al. (2019a) observed several wide binary sdBs formed by stable RLOF and found that the close period systems have lower masses companions and smaller eccentricities (Vos et al., 2019b). He found two populations. The shorter orbital period population are thought to originate from more massive progenitors which undergo non-degenerate He ignition.

Common Envelope Ejection

The common envelope ejection channel produces sdBs in close binaries with thin H-rich envelopes and a mass distribution similar to those stars formed in the RLOF channel. The companions are low-mass white dwarfs, low-mass main-sequence stars or brown dwarfs. The sdB envelopes from common envelope ejection are thinner than those formed by stable RLOF (Han et al., 2002) because the stars are in more compact binaries and hence less of the envelope remains bound to the degenerate core. The thinner envelope results in sdB stars which are hotter and more compact (Han et al., 2002).The donor star first fills its Roche lobe close to the tip of the RGB when its radius increases more quickly than the Roche radius. A common envelope is formed when the envelope of the giant engulfs its low-mass companion. The orbit of the cores shrinks, owing to the friction between the motion of the stars and the common envelope. If sufficient orbital energy is released during the spiral-in phase, the envelope is ejected. Once the envelope has been ejected the $0.45\,M_{\odot}$ core ignites. The mass loss experienced is unstable and occurs on a dynamical time-scale.

It has been suggested that common envelope ejection can be described by the following five phases (Ivanova et al., 2013).

- The common envelope evolution begins with the loss of corotation. The stars start off in a circularized binary with the donor star synchronized to the orbit and ends with spiralling in binary cores. The spiral-in occurs on a dynamical time-scale and may be triggered by unstable mass transfer.

- During the plunge-in phase there is a rapid inward spiral of the stars with the orbital energy deposited in the envelope. This again occurs on a dynamical time-scale.
- After the plunge in there is a period of self-regulated spiralling in. The orbital energy from the spiral-in is transported to the surface and radiated away.
- The termination of the spiral-in operates over several thermal time-scales. Generally speaking, this is when the common envelope is ejected.
- Post common envelope evolution commences.

Common envelope ejection is the most plausible mechanism to form the sdBs in close binary configuration because it shortens the orbit whereas stable Roche lobe overflow widens the orbit. The theory behind common envelope ejection is still rather uncertain and strongly depends upon the efficiency of the release of the orbital energy. The sdB stars may prove to be useful to help understand this process. Schaffenroth et al. (2014)'s observations of the system J162256+473051 confirm that brown-dwarf companions with masses as low as $0.064 M_{\odot}$ are capable of removing the sdB envelope and surviving the common envelope phase. The *EREBOS* project aims to constrain the lowest mass companion which can still remove the sdB envelope (Schaffenroth et al., 2017). Results so far suggest that planet-mass companion objects cannot remove the H envelope.

Helium White Dwarf Merges

Merging double He white dwarf systems are the most likely mode for single sdB formation (Han et al., 2002). The resulting stars have very thin H envelopes and masses distributed between $0.4\,\mathrm{M}_{\odot}$ and $0.7\,\mathrm{M}_{\odot}$ (Han et al., 2003). The required progenitor system of a close white dwarf binary is formed by one or two episodes of CE ejection. If the orbital period is sufficiently short, gravitational wave radiation removes angular momentum from the system causing the orbit to shrink further. Dynamically unstable mass transfer begins once the lower mass star fills its Roche lobe. At this stage the binary has an orbital period on the order of minutes. The unstable mass transfer leads to dynamical disruption of the lower mass object which is then smeared out to form an accretion disc around the more massive white dwarf. Most of disc is accreted on to the white dwarf quickly although some of the disc may persist. If the white dwarf is massive enough after the accretion of the disc, He ignites in its core. The upper mass limit of the merged product is the sum of the original masses of the two white dwarfs, although it is likely that some mass is lost during the process. Any H from the envelopes of either white dwarf is mixed with the He and deeply embedded in the merged product. It is then violently burned once the core ignites.

This channel may be dominant for He rich sdBs (Zhang and Jeffery, 2012) and stars with masses over $0.5\,M_{\odot}$. One would generally expect these stars to be rapidly rotating owing to conservation of angular momentum during the merge. However the majority of sdBs are found to be slow rotators meaning that AM must be transported away during formation or lost soon afterwards. The loss of AM is likely due to magnetic braking because we might expect the merge to produce a strong magnetic field (Tout et al., 2008). Unlike WDs in which the field freezes in, the core He burning driven convection in the sdB can cause it to dissipate.

Helium White Dwarf and Low-Mass Main-Sequence Merges

It has also been proposed that merging a He white dwarf and a low-mass MS companion could produce an sdB (Clausen and Wade, 2011) via accelerated stellar evolution. Single low-mass stars evolve directly onto the EHB with mass-loss on the RGB. Unfortunately, the universe is not old enough for sufficiently low mass stars to have evolved of the main-sequence. The merger product of a He white dwarf and a low-mass main-sequence star makes an evolved star with masses between 0.53 and $0.84\,M_{\odot}$. One of the assumptions of this channel is that the H-envelope must be entirely lost via unstable mass transfer on the RGB. On the RGB Reimers mass-loss removes 0.1 to $0.3\,M_{\odot}$ of material from the merger product. The ejected mass interacts with the magnetic field of the star which slows down the wind and exerts a torque. Angular momentum is transferred from the star to the wind which spins the star down. The sdB models created with this formation channel are naturally slow rotators. This channel has been investigated less rigorously and so many of the details of the evolution are still unknown. The system can also start as a hierarchical triple with the inner binary consisting of a low-mass main-sequence star and a He white dwarf. Dynamical interactions of the triple can cause the inner binary to merge leaving a wide binary with a low-mass MS companion.

Single sdB Formation

Single sdB stars are observed to rotate slowly (Geier and Heber, 2012) and to have a mass distribution peaked at $0.47\,M_{\odot}$ (Fontaine et al., 2012). The merging of a white dwarf with either another white dwarf or a low-mass main-sequence star predicts a broad mass distribution of the resulting sdB star and the initial components can have a range of masses. Furthermore, the merging of two white dwarfs predicts a very rapidly rotating merger product. Single star evolution reproduces the observed mass distribution, because it reflects the mass of the He core in a red giant star, and produces a slowly rotating object. Enhanced mass-loss on the RGB (D'Cruz et al., 1996) produces a single sdB with the desired properties however the reason for this enhanced mass-loss is unclear.

1.2.2 Pulsating sdBs

Non-radial pulsations in sdBs driven by the κ mechanism with iron group elements have been both predicted (Charpinet et al., 1996a) and observed (Green et al., 2003; Kilkenny et al., 1997). The majority of sdBs pulsators have long period gravity (g) mode pulsators with brightness variations on the order of hours. Some sdBs displaying pressure (p) modes with periods of minutes have also been found as well as a small number of hybrid pulsators with both p and g-modes. The hybrid pulsators have oscillation modes which propagate both through their cores, although not through convective regions, and though the outer regions of the star and so are of particular scientific interest. Generally speaking the stars with g-modes are observed to be cooler and have lower surface gravities than those with p-modes as demonstrated in Figure 1.3. The two heavy-metal rich stars LS IV-14°116 (Ahmad and Jeffery, 2005) and Feige 46 (Latour et al., 2019) are both g-mode pulsators with high surface temperatures and surface gravities. The ε mechanism offers a partial solution (Battich et al., 2018; Miller Bertolami et al., 2011). Saio and Jeffery (2019) show that the pulsations can be driven by the κ mechanism in partially ionized regions with C and O opacity bumps.

The observations of low-amplitude p-mode oscillators, also known as V361 Hya pulsators, fit well with the theoretical models in terms of mode excitation Charpinet et al. (2007). The first models for the g-mode pulsators, or V1093 Her stars, were less successful at predicting the excitation boundaries. The observed temperatures of these V1093 Her stars are found to be about 5000 K hotter than the detailed stellar models which reproduced the observed pulsation instability regions. Boosting Ni abundances in the driving regions resolves the so called blue edge problem (Jeffery and Saio, 2006, 2007). The required Ni and Fe abundances have since been naturally created in models with improved atomic diffusion processes (Bloemen et al., 2014).

Pulsations in stars are described with spherical harmonics and have three associated wave-numbers k, l, m. Two of these come from the spherical harmonics $Y_{lm}(\theta, \phi)$. The third comes from the radial part of the solution $R(r)$ such that $\psi_{klm} \propto R(r) Y_{lm}(\theta, \phi)$. If the stars are rotating the degeneracy associated with the azimuthal order m is broken. This manifests as a multiplet splitting in the observed frequency power spectrum. If the split multiplet spacing can be resolved, the rotation rate of a star can accurately be determined independently of the inclination of the system.

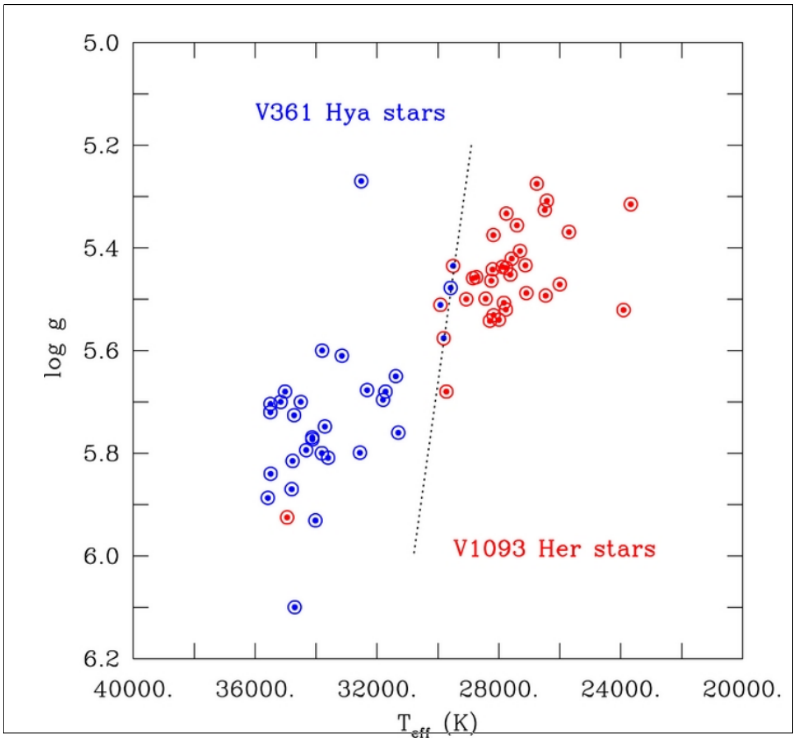

Fig. 1.3 The locations of the V361 Hya and V1093 Her stars on a $\log_{10}(g_{\rm surf}/{\rm cm\,s^{-2}}) - {\rm T_{eff}}$ plane. The V361 Hya stars, marked in blue, are hotter and more compact than the V1093 Her stars which are coloured in red. The hybrid pulsators are displayed with red circles filled in blue and all sit close to the boundary. This figure is from Green et al. (2011).

1.2.3 Rotation and Tidal Locking in sdB Stars

Post-common envelope sdB binaries are good potential laboratories to test tidal theories. The systems may have synchronized on the RGB. During the common envelope evolution the binary separation rapidly shrinks and this breaks any synchronization which has previously occurred. The stars arrive on the EHB shortly after this common envelope phase. Recent observations of sdBs put some constraints on the expected results. A significant fraction of the radius of the star is convective because so much of the envelope has been removed. Tidal synchronization is a controversial topic for stars with convective cores and radiative envelopes such as the sdBs as the details of the dissipation mechanism remain elusive. Most observational studies quote Zahn (1977)'s theory of the dynamical tide. However the synchronization time-scales predicted by this theory are comparable to those of the core helium burning lifetime which is 10^8 yr. The main results studying tidal synchronization are as follows.

Geier et al. (2010) examined the spectroscopic rotational broadening and inclinations of 31 close sdB binaries and then solved the orbits under the assumption of tidal synchronization. Using Tassoul and Tassoul (1992)'s theory they argued that all post-common envelope systems should be tidally synchronized in times shorter than their evolutionary time-scales. The systems with low-mass companions and orbital periods of less than half a day could be solved consistently under the assumption of synchronization owing to Zahn (1977)'s dynamical tide. The sdBs with massive binary companions reveal a surprising dearth of systems with high inclinations suggesting that the assumption of synchronization may be incorrect. Pablo et al. (2012a) observed and analysed B4 which is a spectroscopically confirmed sdB star in the open cluster NGC 6791. The star is in sub-synchronous rotation and exhibits g-mode pulsations. It has an orbital period of 0.398 d and a rotation period of 9.63 d. Pablo et al. (2012b) also analysed the *Kepler* data of two close sdB+dM binary systems with g-mode pulsations. Neither of these systems are synchronized. Both sdBs have orbital periods of 0.4 d and they have spin periods of 10.3 d and 7.4 d. Kawaler et al. (2010) observed another two sdB + dM stars, which were again found to be rotating sub-synchronously. Charpinet et al. (2008) found the pulsating sdB + dM system NY Virginis to be both synchronized and rotating as a solid body in its outer half by radius. In light of these results, Charpinet et al. (2013) suggest that synchronization may be efficient for $P_{\mathrm{orb}} < 0.125\,\mathrm{d}$ for sdB + dM binaries.

Schaffenroth et al. (2014) observed SDSS J162256.66+473051 which is an eclipsing system with an sdB with brown dwarf companion. The orbital period of the system is 0.069 d, or 103.68 min, but the star has a projected rotational velocity of $74\,\mathrm{km\,s^{-1}}$. This is a sub-synchronous system since a rotational velocity of about $100\,\mathrm{km\,s^{-1}}$ would be required for synchronization. If this sdB has a mass of $0.47\,\mathrm{M_\odot}$ the most likely companion mass is $0.064\,\mathrm{M_\odot}$. Maxted et al. (2002) observed PG $1017-086$ which has an orbital period of 0.073 days or 105.12 minutes. The rotational velocity of this object was found by least squares fitting of the Hα line and was measured as $v_{\mathrm{rot}} \sin i = 118\,\mathrm{km\,s^{-1}}$. They then assume synchronous rotation, as do many other studies, to constrain the inclination i so this isn't really a confirmation of synchronization. The lack of eclipses constrains the inclination to <72°. The companion mass derived from the study is $0.0687(250)\,\mathrm{M_\odot}$.

Observational results suggest that tides are active in the sdB stars and that they are spun up relative to the wide orbit or single sdB stars, who's spin periods are similar to those of red giants, but that the systems are not tidally locked. The discovery of pulsations in sdBs and the recent advances in the precision of photometric measurements gathered with telescopes have made these objects good asteroseismology candidates. Asteroseismology has led to the more accurate measurement of rotation rates so more systems can be studied and their synchronization status can be confirmed or denied.

1.3 Asteroseismology

Pulsating stars can be thought of as resonant spheroids with natural frequencies of oscillation, which can be excited when perturbed. Not all stars are pulsators although those that are can be categorised by their location on the Hertzsprung–Russell diagram. Figure 1.4 shows the known classes of pulsating star and their locations. The majority of physical processes involved with the evolution of stars occur deep within their interiors. Unfortunately, with most observational techniques, it is only possible to learn about the surface properties of a star. Asteroseismology is the study of the internal properties of a star by analysing its observed pulsation oscillation frequency spectra. The word asteroseismology, as discussed by Gough (1996), comes from the Greek words *Aster* ($\alpha\sigma\tau\eta\rho$), *seismos* ($\sigma\varepsilon\iota\sigma\mu o\varsigma$) and *logos* ($\lambda o\gamma o\varsigma$), meaning star, tremor and logic respectively. The technique was first used for helioseismology by Christensen-Dalsgaard and Gough (1976) to determine the internal properties of our Sun.

1.3.1 Driving Mechanisms

Hydrostatic equilibrium balances pressure with gravity and restores stability from structural perturbations on the dynamical time-scale. To have periodic variation pulsating stars must have a driving mechanism. The four major proposed driving mechanisms are the ε mechanism, the κ mechanism, convective blocking and stochastic excitations (Aerts et al., 2010).

The ε Mechanism

In the ε mechanism variations in the nuclear reaction rate drive pulsations (Rosseland and Randers, 1938). An increase in the nuclear reaction rate produces more energy. In response to this extra energy the pressure increases and the star expands. During the expansion the pressure drops and so the rate of nuclear reactions drops. The star begins to cool and contract, causing an increase in the average pressure and temperature and the nuclear reaction rate rises again. The periodic repetition of this process drives pulsations. Despite this being one of the earliest proposed mechanisms for stellar pulsation there is still a dearth of supporting observational evidence. Most stars have stable nuclear reaction rates. Even the unstable thermal pulses seen in AGB stars happen on time-scales which are too long to result in dynamical pulsations via this mechanism.

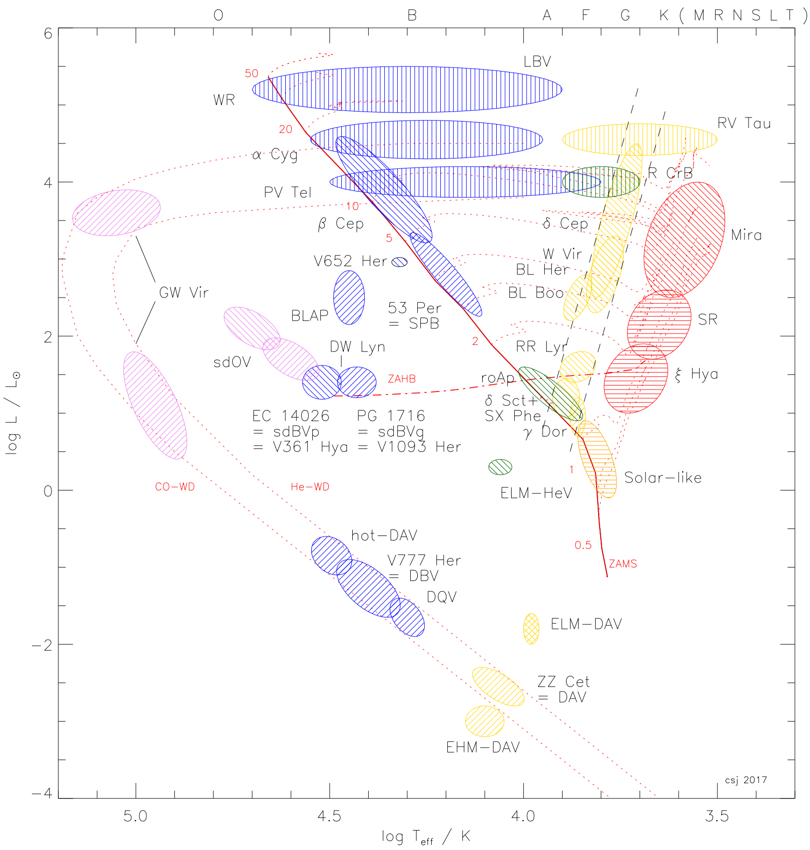

Fig. 1.4 The different classes of known pulsators and their location on the H–R diagram. The regions in dotted lines are predicted instability regions. This figure is from (Jeffery, 2008), modified to include recent discoveries (priv. comm.)

The κ Mechanism

Opacity κ describes how efficient stellar material is at absorbing incident radiation. The κ mechanism, or the Eddington valve, relies on variations in the opacity in certain regions of the star. These variations come in the form of opacity bumps which are local peaks in the temperature profile of the opacity (Baker and Kippenhahn, 1962). Opacity bumps form in the partially ionized regions of stars. They are usually caused by H and He but heavier elements can also provide the same effect. Partial ionization of the stellar material raises the opacity which then blocks the radiation and heats the surrounding gas. The pressure increases and the star expands past its equilibrium point. The expansion reduces the ionization fraction of the gas and thence the opacity so that radiation escapes with fewer interactions with the surrounding material. The gas then cools and contracts under gravity. During the contraction phase the gas recombines and the temperature and opacity rise, returning the gas to its initial state and the cycle restarts. The κ mechanism was first used to describe the variations seen in δ Cephei stars. Other classes of star seen to oscillate with this mechanism are β Cephei, δ Scuti stars and some sdB stars (Charpinet et al., 1996a).

Convective Blocking

Convective blocking occurs if a composition transition region is just above the base of a convective region (Brickhill, 1991; Pesnell, 1987). The transition region produces a small amount of driving. Radiative luminosity rapidly drops off in convective regions so the energy coming from the inner regions of the star cannot be moved by radiative transport any more. It is assumed that the convective region does not instantaneously adjust to changes in the incident luminosity. The extra luminosity from the pulsations driven in the transition region is temporarily trapped. The radiation heats the surrounding material causing it to expand. As the material expands, energy is released and the star eventually cools and contracts. With the contraction, the temperature rises and the radiation is trapped again. This process repeats cyclically to drive pulsations in γ Doradus (Guzik et al., 2000) stars.

Stochastic Excitation

Pulsations in solar-like stars are induced by stochastic excitations (Goldreich et al., 1994). These stars have turbulent convective surfaces. The vigorous motion generates significant acoustic noise over a broad range of frequencies. The acoustic noise can resonate with the otherwise stable normal oscillation modes of the star. Owing to the complexity of the turbulent surface convection the pulsations excited in this manner are random in nature.

The balance between the complex excitation and the intrinsic damping of the pulsations determines the amplitudes.

1.3.2 Radial Linear Adiabatic Stellar Oscillations

Radial modes are the simplest form of pulsations. The stars radially expand and contract periodically whilst maintaining spherical symmetry. For the fundamental mode, the entire star expands and contracts. The overtones have radial nodes, which are stationary, and periodically expanding and contracting regions everywhere else. Mathematically, the displacement of the star owing to the oscillations can be treated as an eigenvalue problem with differential equations of Sturm–Liouville form. If the perturbations are small the equations are linear. The fundamental pulsation period Π of a star is of the order

$$\Pi \approx \frac{2R}{\bar{c}_{\mathrm{s}}}, \tag{1.2}$$

here R is the radius of the star and $\bar{c}_{\mathrm{s}}$ is the mean sound speed defined by $\bar{c}_{\mathrm{s}} = \sqrt{\Gamma_1 P/\rho}$ where P is the pressure and ρ is the density. The adiabatic exponent is

$$\Gamma_1 = \left(\frac{\partial \ln P}{\partial \ln \rho}\right)_S, \tag{1.3}$$

with the derivative at constant entropy S. Following Cox (1967) and Gough (priv. comm.) the linear adiabatic wave equation for stellar oscillations can be derived from the mass continuity equation

$$\frac{dm}{dr} = 4\pi\rho r^2, \tag{1.4}$$

where m is the mass enclosed within radius r. The Lagrangian equation for hydrostatic support which balances the inward gravity with the pressure is such that

$$\frac{dP}{dm} = -\frac{1}{4\pi r^2}\left(\frac{Gm}{r^2} + \ddot{r}\right), \tag{1.5}$$

where $\ddot{r}$ is the acceleration at fixed m. The energy equation states that for radial nodes

$$\dot{P} - \frac{\Gamma_1 P}{\rho}\dot{\rho} = (\Gamma_3 - 1)\rho\left(\varepsilon - \frac{1}{\rho}\frac{\partial L_r}{\partial m}\right), \tag{1.6}$$

where the dots are derivatives with respect to time, ε is the energy generated from the nuclear reactions L_r is the internal luminosity and

$$\Gamma_3 - 1 = \left|\frac{\partial T}{\partial \rho}\right|_{\mathrm{ad}} = \left|\frac{\partial P}{\partial(\rho E)}\right|_{\rho}, \tag{1.7}$$

where ρE is the internal energy per unit volume. Generally with stellar oscillations one considers the relative displacement

$$\zeta = \delta r / r_0, \tag{1.8}$$

where r_0 is the equilibrium radius and the instantaneous radial distance of the mass shell is

$$r = r_0(1+\zeta), \tag{1.9}$$

and the instantaneous value of a relative Lagrangian variation of a given element f is

$$f = f_0\left(1 + \frac{\delta f}{f_0}\right). \tag{1.10}$$

The general form for linearizing equations, to first order, is

$$\frac{dy}{dt} = f(y,u) \approx f(\bar{y},\bar{u}) + (y-\bar{y})\left.\frac{\partial f}{\partial y}\right|_{\bar{y},\bar{u}} + (u-\bar{u})\left.\frac{\partial f}{\partial u}\right|_{\bar{y},\bar{u}}, \tag{1.11}$$

where the bars denote the equilibrium values. The linearized form of Eq. 1.4, if only considering first order terms and dropping zero subscripts, is

$$\frac{\delta\rho}{\rho} = -3\zeta - r\frac{\partial\zeta}{\partial r}. \tag{1.12}$$

The linearized form of 1.5 is

$$\frac{\partial \delta P}{\partial r} = -4\frac{dP}{dr}\zeta - r\rho\ddot{\zeta}. \tag{1.13}$$

Finally, Eq. 1.6 can be expressed as

$$\delta\dot{P} - \frac{\Gamma_1 P}{\rho}\delta\dot{\rho} = (\Gamma_3 - 1)\rho\left(\delta\varepsilon - \frac{\partial \delta L_r}{\delta m}\right), \tag{1.14}$$

where L_r is the internal luminosity. The time derivatives of the linearized pressure and mass continuity equations can be substituted into the energy equation, if radius derivatives of the energy equation are taken, to give

$$-4\frac{dP}{dr}\dot{\zeta}-r\rho\dddot{\zeta}-\frac{\partial}{\partial r}\left\{\Gamma_1 P\left(-r\frac{\partial\dot{\zeta}}{\partial r}-3\dot{\zeta}\right)+(\Gamma_3-1)\rho\left(\delta\varepsilon-\frac{\partial\delta L_r}{\delta m}\right)\right\}=0. \quad (1.15)$$

Isolating the first term in the curly brackets from Eq. 1.15, expanding the derivatives, dividing through by r^3 then re-factorising the resulting expression gives

$$\frac{\partial}{\partial r}\left\{\Gamma_1 P\left(-r\frac{\partial\dot{\zeta}}{\partial r}-3\dot{\zeta}\right)\right\}=\frac{1}{r^3}\frac{\partial}{\partial r}\left(\Gamma_1 P r^4\frac{\partial\dot{\zeta}}{\partial r}\right)+3\frac{d(\Gamma_1 P)}{dr}\dot{\zeta}. \quad (1.16)$$

Substituting Eq. 1.16 back in to Eq. 1.15 gives

$$\frac{\partial}{\partial r}\left(\Gamma_1\rho r^4\frac{\partial\dot{\zeta}}{\partial r}\right)+r^3\left\{\frac{d}{dr}\left[(3\Gamma_1-4)P\right]\dot{\zeta}-r\rho\dddot{\zeta}\right\}=r^3\frac{\partial}{\partial r}\left\{(\Gamma_1-1)\rho\left(\delta\varepsilon-\frac{\partial\delta L_r}{\partial m}\right)\right\}, \quad (1.17)$$

in the adiabatic case the right hand side is zero and several of the terms simplify. One considers solutions of the form

$$\zeta(r,t)=\xi(r)e^{i\omega t}, \quad (1.18)$$

where ω is the eigenfrequency of the mode, t is time and $\xi(r)$ is the spatial component of the solution. The linearized adiabatic wave equation becomes

$$\frac{d}{dr}\left(\Gamma_1 P r^4\frac{d\xi}{dr}\right)+\left\{r^4\frac{d}{dr}\left[(3\Gamma_1-4)P\right]+r^4\rho\omega^2\right\}\xi=0. \quad (1.19)$$

The $\omega=0$ solution is discarded because it is just the static case. Solutions which have real $\xi(r)$ describe standing waves.

Non-Radial Modes

Oscillations in stars are analogous to oscillations on a string if generalised to the spherical, three dimensional case. The natural oscillation modes can have nodes in any of the r, θ or ϕ directions of spherical polar co-ordinates. The oscillations are treated as small perturbations to the equations of stellar structure which disrupt the spherical symmetry of the star. Stars with non-radial modes break spherical symmetry because the star physically changes shape. The eigenfunctions in this case are proportional to the spherical harmonics.

Solutions can be expressed as

$$\zeta(r,\theta,\phi,t) = \xi(r,\theta,\phi)e^{i\omega t}, \tag{1.20}$$

where the orthogonal components of the Lagrangian displacement are

$$\begin{aligned}
\zeta_r(r,\theta,\phi,t) &= a(r)Y_l^m(\theta,\phi)exp(i\omega t),\\
\zeta_\theta(r,\theta,\phi,t) &= b(r)\tfrac{\partial Y_l^m(\theta,\phi)}{\partial\theta}exp(i\omega t),\\
\zeta_\phi(r,\theta,\phi,t) &= \tfrac{b(r)}{\sin\theta}\tfrac{\partial Y_l^m(\theta,\phi)}{\partial\phi}exp(i\omega t).
\end{aligned} \tag{1.21}$$

The spherical harmonics are

$$Y_l^m(\theta,\phi) = (-1)^m N_l^m P_l^m(\cos\theta)e^{im\phi}, \tag{1.22}$$

where P_l^m is the associated Legendre polynomial which can be generated by

$$P_l^m(\cos\theta) = \frac{1}{2^l l!}(1-\cos^2\theta)^{m/2}\frac{d^{l+m}}{d\cos^{l+m}\theta}(\cos^2\theta-1)^l, \tag{1.23}$$

and N_l^m is a normalisation constant which ensures that Y_l^m integrates to one over all directions. It is

$$N_l^m = \sqrt{\frac{2l+1}{4\pi}\frac{(l-m)!}{(l+m)!}}. \tag{1.24}$$

Three quantum numbers k, l and m describe the geometry of a given eigenmode. The number of radial nodes of the mode is denoted k. The degree of the mode states how many surface nodes exist and is labelled l. Finally m is the azimuthal order of the pulsation and dictates how many of the surface nodes cross the equator of the star. Figure 1.5 shows the spherical harmonics for different l and m. The zonal modes are the $m=0$ modes and have no node lines intersecting the equator. The sectoral modes have $m=l$ and all the node lines pass through the equator. Tesseral modes are a combination of the two and have $0<m<l$.

To derive the adiabatic wave equation for stars with non-radial pulsations, we start with the Euler equation

$$\rho\frac{d\boldsymbol{u}}{dt} = -\nabla P + \rho\nabla\Phi, \tag{1.25}$$

where $\boldsymbol{u} = d\boldsymbol{\zeta}/dt$, $P = P_0 + P'$, $\rho = \rho + 0 + \rho'$ and $\Phi = \Phi_0 + \Phi'$ so the linearized momentum equation is

$$\rho \frac{\partial^2 \boldsymbol{\zeta}}{\partial t^2} = -\omega^2 \rho \xi = -\nabla P' + \rho' \nabla \Phi + \rho \nabla \Phi', \tag{1.26}$$

where Φ is the potential and primes are the perturbation to a quantity. Cowling (1941) shows that the Φ' term can be ignored if l and the radial order $|k|$ are large. The continuity equation is

$$\delta \rho = \rho' + \frac{d\rho}{dr} \xi_r, \tag{1.27}$$

the pressure equation gives

$$\delta P = c^2 \left(\rho' + \frac{d\rho}{dr} \xi_r \right), \tag{1.28}$$

and the momentum equation in the radial direction is

$$\frac{\partial P'}{\partial r} + \frac{gP'}{c^2} = \rho(\omega^2 - N^2)\xi_r, \tag{1.29}$$

where N is the Brunt-Väilsälä frequency which dictates the rate of oscillation of a packet of gas radially about its equilibrium location within the star such that

$$N^2 = g\left(\frac{1}{p_0 \Gamma_1} \frac{dp_0}{dr} - \frac{1}{\rho_0} \frac{d\rho_0}{dr} \right). \tag{1.30}$$

The adiabatic wave equation for non-radial pulsations is

$$\frac{1}{r^2} \frac{\partial}{\partial r} \left(r^2 \zeta_r \right) - \frac{g}{c^2} \zeta_r = -\frac{P'}{P} - \frac{\nabla_h^2 P'}{\omega^2}, \tag{1.31}$$

in terms of spherical harmonics the adiabatic wave equation becomes

$$\frac{1}{r^2} \frac{\partial}{\partial r} \left(r^2 \zeta_r \right) - \frac{g}{c^2} \zeta_r = -\frac{1}{\Gamma_1 P} \left(1 - \frac{L_l^2}{\omega^2} \right) P', \tag{1.32}$$

where ∇_h is the horizontal motion. The L_l is the Lamb frequency which is the inverse of the time taken to travel one horizontal wavelength within the star and defined

$$L_l^2 = \frac{l(l+1)c_s^2}{r^2}. \tag{1.33}$$

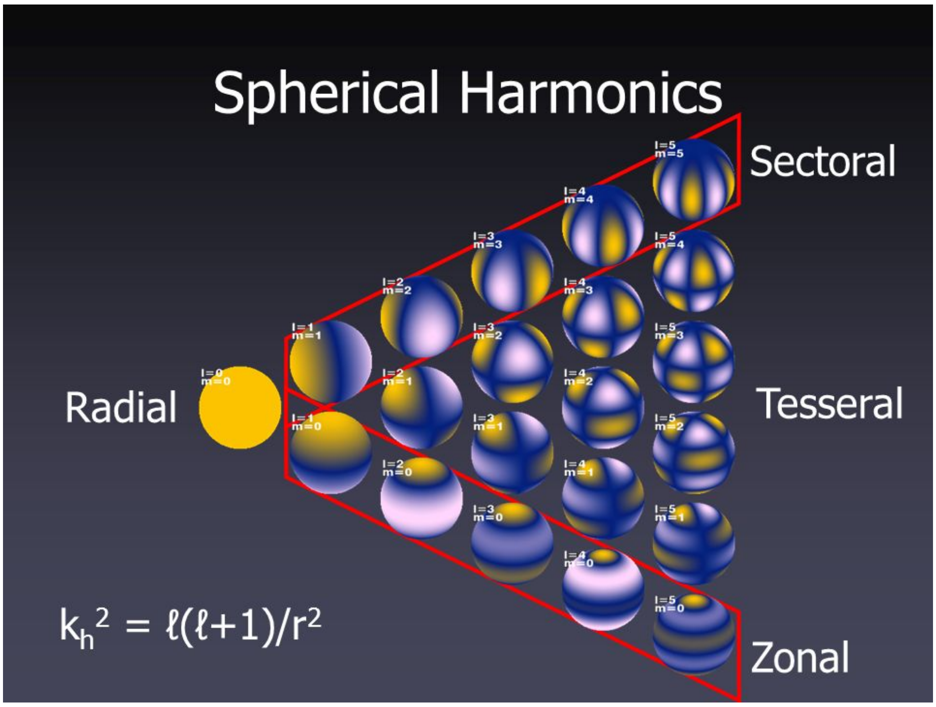

Fig. 1.5 The spherical harmonics with different values of the wavenumbers l and m. The l dictates the number of surface nodes and m dictates how many of these cross the equator of the star. Image from Townsend ESO Chile November 2006 Presentation Slides

1.3.3 Pressure and Gravity Modes

The Lamb frequency L_l and the Brunt-Väilsälä frequency N dictate the propagation of the pulsation modes within the stellar interior. These two frequencies can be compared to the stellar oscillation frequency ω to find the main restoring force in the region considered. If ω is greater than the Lamb and Brunt-Väilsälä frequencies the restoring force is pressure. Pressure modes are acoustic waves which are short in period and propagate in the same direction as the oscillation. The waves are located in the outer regions of the star and start at the surface moving radially towards the centre. The speed of sound increases with proximity to the centre of the star which causes the waves to be refracted back towards the surface. Once at the surface the waves are reflected by the sharp drop in density. This pattern of motion continues around the star. Conversely, if ω is smaller than L_l and N g-modes are in operation and the restoring force is gravity, specifically the buoyancy. The g-modes propagate orthogonally to the direction of motion with long period oscillations and penetrate deep within the stellar interior. The propagation of p and g-modes through the star is displayed in Figure 1.6. Pulsations are quickly damped and fizzle out when ω is between the two frequencies. Figure 1.7 shows the effect of l on the frequency of pulsations.

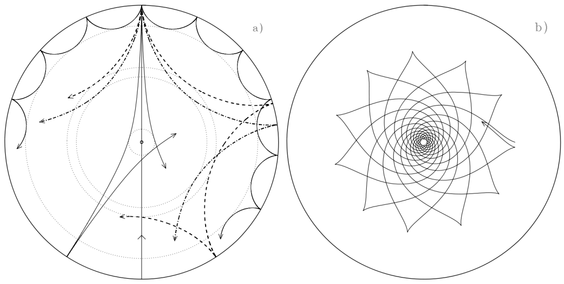

Fig. 1.6 The propagation of p-modes (left) and g-modes (right) through the interior of a 1 $M_\odot$ star. Figure from Aerts et al. (2010).

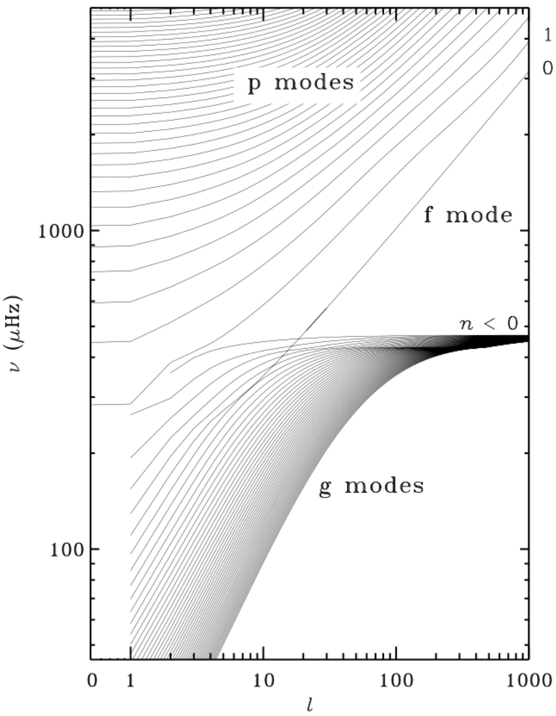

Fig. 1.7 The frequencies of stellar oscillation as a function of spherical degree l for a solar type star. This image is from Aerts et al. (2010)

1.3.4 Observations

Asteroseismology uses observational time series measurements made with either photometry, to detect changes in the apparent luminosity, or spectroscopy, to see surface velocity variations (Aerts et al., 2010). Photometric light-curves which show periodic variation owing to pulsations can be Fourier transformed to obtain power spectra in frequency space. The peaks in the power spectra correspond to the observed eigenfrequencies. The stars must be observed for many pulsation cycles to obtain precise measurements because the frequency resolution, $\Delta\nu$, is given by

$$\Delta\nu \propto \frac{1}{\Delta t}, \tag{1.34}$$

where Δt is the total time of all observations. Space based photometry has revolutionised the field because it allows continuous measurements to be taken whilst bypassing several of the undesirable effects associated with ground based observation including clouds and atmospheric turbulence. Frequency analysis is carried out on the measured light curves to find the frequencies of pulsation and identify the modes. The highest frequency which can reliably be inferred corresponds to the Nyquist frequency which is defined as half of the sampling rate. For example, if 100 samples are taken per second the corresponding Nyquist frequency is 50 Hz. Data is generally converted to the frequency domain with a discrete Fourier transform of the form

$$F_N(\nu) = \sum_{k=1}^{N} x(t_k) e^{i2\pi\nu t_k}, \tag{1.35}$$

where $x(t_k)$ is the time series, N is the number of measurements and ν is the frequency. Once a frequency power spectrum has been obtained the modes can be identified. Mode identification aims to assign the quantum numbers k, l and m to the observed frequencies. The k is the radial overtone, l is the number of node lines on the surface and m is the number of node lines which pass through the equator. If the star is spherically symmetric and not rotating the m mode frequencies are degenerate. The g-modes have periods which are linearly spaced and the p-modes have frequencies that are linearly spaced for increasing l. The difference in frequency of two adjacent l modes is called the larger frequency separation. When the stars are rotating the degeneracy of the m modes is broken. To first order and assuming that the star rotates as a solid body the frequency separation between the m modes is equal and called the rotational splitting. The frequency separation of a rotationally split multiplet is

$$\Delta\nu_{kl} = V_{\mathrm{rot}}(1 - C_{kl}) \tag{1.36}$$

where $V_{\mathrm{rot}} = 1/P_{\mathrm{rot}}$ and the Ledoux coefficient (Ledoux, 1951) is defined

$$C_{kl} = \frac{\int_0^R (\varepsilon_h^2 + 2\varepsilon_r\varepsilon_h)\rho r^2\, dr}{\int_0^R (\varepsilon_r^2 + l(l+1)\varepsilon_h^2)\rho r^2\, dr} \tag{1.37}$$

where $\varepsilon_r(r)$ and $\varepsilon_h(r)$ are the zeroth order radial and horizontal displacement eigenfunctions of the mode. For p modes the contribution from the Ledoux coefficient is often ignored.

The spin period of the star can be determined fare more accurately than from rotational broadening of spectral lines if the spacing of a rotationally split multiplet is known.

The space missions *Kepler*, *K2* and *TESS*, and the upcoming *PLATO*, have hugely increased the precision of photometric measurements relative to ground based observations. The highest quality observations now have precision in the 1 μHz region owing to the short cadence of the observations and the long time base of continuous observations. Recent improvements to the quality of asteroseismic data have reinvigorated the field and allow for the testing and development of the understanding of the physics operating within these stars.

1.4 Tidal Interactions

Tidal interactions act to bring a binary system to the equilibrium tidally locked configuration. When tidally locked the spin of both of the objects is aligned with and synchronized to the circularized orbit. Fig. 1.8 is a schematic diagram demonstrating tidal synchronization. When a massive companion is close to the star there is a difference in the potential between the side closest to and that furthest from the companion star. This causes a bulge to form along the line connecting the centre of masses of the two stars. The star is distended both towards the companion, because the matter there is pulled towards the companion, and away from the companion, because the matter there is less tightly bound. If the system is synchronized the bulge stays in the same place on the star and always points towards the companion. If the system is not synchronized and there is no dissipation mechanism, the bulge moves around the star always pointing towards the companion. If the system is not synchronized, and there is a dissipative mechanism, the bulge moves away from the line connecting the centre of masses. This creates a torque through the star causing it to spin up or down until it is synchronized, if such a stable configuration exists. The equilibrium tide describes the instantaneous shape of the distorted star and mathematically refers to the particular integral solution of the governing differential equations. If the orbit of the system isn't synchronized the tidal bulge moves away from the line connecting the centres of masses perturbing the equilibrium tide. Mathematically this perturbation is described by the complimentary function and physically refers to the dynamical tide. Simple models examine how the changes in the equilibrium tide are dissipated.

Darwin (1879) created the earliest robust theory of tidal interactions. This theory suggested that tidal locking was achieved purely by the torque created by the tidal bulge. Unfortunately this mechanism failed to produce the torque necessary to tidally lock a system. In convective regions the bulk movement of material over large distances causes a natural turbulent viscosity. Viscosity provides a drag which prevents the bulge moving instantaneously around the star and offers a mechanism to dissipate energy via the equilibrium tide. Among others, Peter Eggleton has also written his own formalism of convective dissipation (Eggleton, 2006; Eggleton et al., 1998). Eggleton's theory is self consistent and is derived by citing only the Navier-Stokes equation, the Poisson equation and the equation of continuity but requires a local viscosity to dissipate energy. There are currently two dominant theories of tidal interactions which attempt to answer the question of how the tidal energy is dissipated in the radiative regions. One was proposed by Zahn (1975, 1977) and the other by Tassoul (1987). Zahn's theory of dynamical tides applies to stars with convective cores and radiative envelopes and suggests that the periodically varying potential in the star resonates with and excites the stars natural modes of oscillation. These oscillations are excited near the

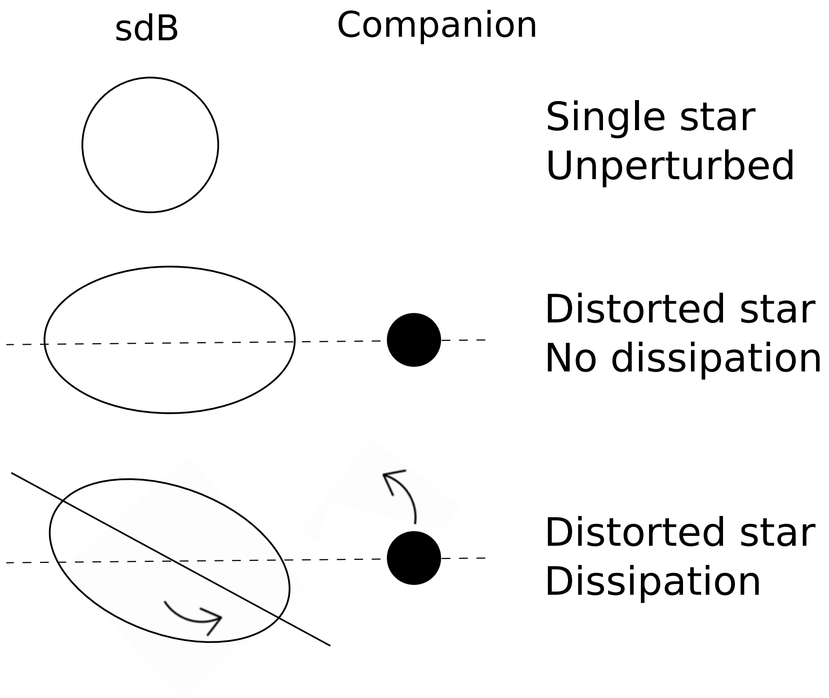

Fig. 1.8 Schematic diagram illustrating basic tidal interactions. The top panel is a single unperturbed star. In the second panel, the star has a close companion causing tidal distortion in the form of a bulge on both sides of the star. This system is either locked or has no dissipation because the bulge is along the line connecting the centres of mass of the objects. The bottom panel shows a tidally distorted star with some sort of dissipation mechanism causing the bulge to move away from the line connecting the centres of mass of the two stars. This system is rotating sub-synchronously, spinning slower than it orbits, causing the tidal bulge to lag behind the line connecting the two centres of masses. The tidal bulges then experience a torque that serves to drive the system to synchronization.

convective core boundary then damped in the radiative envelope which provides a dissipative mechanism for the tides. This theory predicts reasonable circularization time-scales but synchronization time-scales which are too long to account for the observed numbers of locked systems. Tassoul and Tassoul's hydrodynamical mechanism was proposed in an attempt to counteract these problems. It successfully predicts shorter synchronization time-scales. The tidal disruption give rise to larger scale meridional flows. Mass exchange between an Ekman boundary layer and the rest of the star allows angular momentum facilitates angular momentum exchange which can spin up or spin down ther star. In an Ekman layer the forces owing to pressure, the Coriolis force and the turbulent drag are balanced. Tassoul (1987) suggests that large-scale meridional flow very efficiently synchronizes a star. However, (Rieutord and Zahn, 1997) highly contest Tassoul (1987)'s theory by showing that incorrect boundary conditions were used to increase the efficiency of the Ekman pumping.

1.4.1 Convective Dissipation Derivation

Following (Eggleton, 2006; Eggleton et al., 1998) a theoretical framework for tidal dissipation can be derived assuming only Poisson's equation for the gravitational potential ϕ which states

$$\nabla^2\phi = 4\pi G\rho, \tag{1.38}$$

and the Navier-Stokes equation for the flow of fluid in an inertial frame of reference

$$\rho\frac{D\boldsymbol{v}}{Dt} = -\rho\nabla\phi - \nabla P + \nabla.(\rho\nu\{\nabla\boldsymbol{v}\}), \tag{1.39}$$

where t is time, $\boldsymbol{v}$ is the velocity field of the fluid, ρ is density, P is pressure and ν is the fluid viscosity.

The Effective Potential

Assuming that the mass of the star remains constant, the time derivative of the mass continuity equation for a star gives

$$\frac{dM_1}{dt} = \int_{V_1}\frac{d(\rho dV)}{dt} = 0, \tag{1.40}$$

where V_1 is the volume enclosing the star under consideration and M_1 is the mass of the tidally perturbed body. Then

$$\dot{\boldsymbol{r}} = \frac{d\boldsymbol{r}}{dt} = \frac{1}{M_1}\int_{V_1}\boldsymbol{v}\rho dV, \tag{1.41}$$

where $\boldsymbol{r}$ is a vector from the centre of mass of the system. Further assuming that P and ρ vanish outside the surface of the star and utilising the Navier-Stokes equation gives

$$\ddot{\boldsymbol{r}}_1 = -\frac{1}{M_1}\int_V \rho\nabla\phi dV. \tag{1.42}$$

The force on star 1 is

$$\boldsymbol{F_1} = M_1\ddot{\boldsymbol{r}}_1 = -\int_{V_1}\rho\nabla\phi dV, \tag{1.43}$$

and self forces $\boldsymbol{F}'_1 = -\int_{V_1}\rho\nabla\phi_1 dV$ vanish because one finds

$$\boldsymbol{F_1'} = -\int_{V_1}\frac{1}{4\pi G}\nabla^2\phi_1\nabla\phi_1 dV = \int_{S_1}\left\{\frac{\partial\phi_1}{\partial x_j}\frac{\partial\phi_1}{\partial x_i} - \frac{1}{2}\delta_{ij}\frac{\partial\phi_1}{\partial x_k}\frac{\partial\phi_1}{\partial x_k}\right\}dA_j, \tag{1.44}$$

where A is the area enclosed by the surface S_1 so $\boldsymbol{F}'_1 = -\int_{V_1} \rho \nabla \phi_2 dV$. The potential for a star follows

$$\phi_1(x) = -G \int_{V_1} \frac{\rho(\boldsymbol{x'})}{|\boldsymbol{x}-\boldsymbol{x'}|} dV, \tag{1.45}$$

where $\boldsymbol{x}$ is a vector from the centre of mass of the tidally distorted object to the companion. Taylor expanding this gives

$$\phi_1(x) \approx -G \left\{ \int_{V_1} \frac{\rho(\boldsymbol{x'})}{x} dV - \int_{V_1} \rho(\boldsymbol{x'})\boldsymbol{x'}.\nabla \frac{1}{x} dV + \frac{1}{2} \int_{V_1} \rho(\boldsymbol{x'}) x'_i x'_j \frac{\partial^2}{\partial x_i \partial x_j} \left(\frac{1}{x} \right) dV \right\}, \tag{1.46}$$

where the first term is the monopole, the second term is the dipole and the third term is the quadrupole. The dipole term vanishes to keep the star in a Keplerian orbit. One can define the trace-free quadrupole tensor

$$q_{ij} = \frac{1}{2} \int_{V_1} \rho(x')(3x'_i x'_j - x'^2 \delta_{ij}) dV, \tag{1.47}$$

Using the quadrupole tensor the potential can be expressed as

$$\phi_1 = -\frac{GM_1}{\boldsymbol{x}} - G q_{ij} l_{ij}(\boldsymbol{x}), \tag{1.48}$$

where

$$l_{ij}(\boldsymbol{a}) = \frac{a_i a_j - \frac{1}{3} a^2 \delta_{ij}}{a^5} = \frac{1}{3} \frac{\partial^2}{\partial a_i \partial a_j} \left(\frac{1}{a} \right) = \frac{l_{ij}(\hat{\boldsymbol{a}})}{a^3}. \tag{1.49}$$

The effective potential in the frame accelerating and rotating with star 1 which has angular frequency Ω is

$$\phi^{**} = \frac{GM_1}{x} - \frac{GM_2}{r} - \frac{1}{3}\Omega^2 x^2 - G q_{ij} l_{ij}(\boldsymbol{x}) - \frac{3}{2} G M_2 x^5 l_{ij}(\boldsymbol{x}) l_{ij}(\boldsymbol{r}) + \frac{1}{2} \Omega^2 x^5 l_{ij}(\hat{\boldsymbol{\Omega}}) l_{ij}(\boldsymbol{x}). \tag{1.50}$$

Properties of the Quadrupole Tensor

The star has an axis of symmetry through the tidal bulge which is the $\boldsymbol{k}$ axis. The trace-free quadrupole tensor is defined such that

$$q_{ij} = q(k_i k_j - \frac{1}{3}\delta_{ij}) = q l_{ij}(\boldsymbol{k}), \tag{1.51}$$

and

$$l_{ij}(\boldsymbol{k}) l_{ij}(\hat{\boldsymbol{x}}) = x^3 l_{ij}(\boldsymbol{k}) l_{ij}(\boldsymbol{x}) = \cos^2\theta - \frac{1}{3} = \frac{2}{3} P_2(\cos\theta), \tag{1.52}$$

where θ is the angle between $\boldsymbol{k}$ and $\boldsymbol{x}$.

The Shape of the Tidal Bulge

As posited by Darwin (1879), the tidal bulge is modelled as symmetric with a shape described by a second order Legendre polynomial. To lowest order an equipotential surface of a tidally distorted star can be approximated by

$$\bar{r} \approx r(1+\alpha(r)P_2(\cos\theta)), \tag{1.53}$$

$$r \approx \bar{r}[1-\alpha(\bar{r})P_2(\cos\theta)], \tag{1.54}$$

where $r(\theta)$ is the local radius of the equipotential, P_2 is the second order Legendre polynomial and θ is the polar angle subtended in the star. The amplitude of the Legendre polynomial distortion at a given radius of the star is defined by $\alpha(r)$ which is dimensionless and depends on the structure of the star. As α is to first order it can be treated as the same function of r or $\bar{r}$. Substituting

$$\nabla\phi = \phi'\nabla\boldsymbol{r}, \tag{1.55}$$

into Poisson's equation gives

$$\nabla^2\phi = \phi''|\nabla\boldsymbol{r}|^2 + \phi'\nabla^2\boldsymbol{r}, \tag{1.56}$$

where

$$\nabla\boldsymbol{r} = (1+(r\alpha)'P_2(\cos\theta))\boldsymbol{e}_r + \alpha\frac{dP_2(\cos\theta)}{d\theta}\boldsymbol{e}_\theta, \tag{1.57}$$

so

$$\nabla^2\phi = \phi'' + \frac{2}{r}\phi' + \left\{r\alpha'' + 4\alpha' - 2r\frac{\phi''}{\phi'}\left(r\alpha' + \alpha\right)\right\}\phi' P_2(\cos\theta) = 4\pi G\rho, \tag{1.58}$$

where θ is the angle from the axis of symmetry. Collecting the angular terms gives Clairaut's equation

$$r^2\alpha'' + 4r\alpha' - 2\alpha + 2r\frac{\phi''}{\phi'}\left(r\alpha' + \alpha\right) = 0. \tag{1.59}$$

If the density is uniform $\rho(r) =$const and $\alpha(r) =$ const. In the non-homogeneous case Clairaut's equation can be solved for an unperturbed, non-rotating, detailed 1D stellar model, such as is output by the STARS code. The solution for $\alpha(r)$ can be used to create 2D tidally distorted stars with equipotential surfaces with Eq. 1.54. On the surface

$$\alpha(R) = -\frac{2}{3}\frac{\Delta R}{R}. \tag{1.60}$$

The quadrupole tensor q_{ij} has a dimensionless moment such that $q_{ij} = QM_1 R\Delta R l_{ij}(\boldsymbol{k})$

$$Q = \int_0^R \frac{4\pi\rho r^4(5\alpha + r\alpha')}{5MR^2\alpha(R)} dr, \tag{1.61}$$

where $\rho(r)$ is the density of the star at a given r, $\alpha(R)$ is $\alpha(r)$ at the surface of the star and R is the total radius of the star. The Q is dimensionless and independent of the perturbation, it depends only on the internal structure of the tidally distorted star.

Dissipation

If the orbit of the binary is not synchronized with the rotation, a time varying velocity field is produced within the star as tides are raised and lowered. A model of the interior of the star as a fluid with constant density along equipotentials and a tidal bulge described by a Legendre polynomial allows the velocity field to be described with the equation of continuity. The shape of the tidal distortion can be expressed as

$$\bar{r} = r + \frac{\alpha(r)}{r} H, \tag{1.62}$$

where $H(r,\theta)$ is a harmonic function describing the shape of the distorted star and $\bar{r}$ is constant in θ,

$$H(r,\theta) = r^2 P_2(\cos\theta). \tag{1.63}$$

With the time derivative of H denoted by K, the continuity equation can be satisfied by the velocity field $\boldsymbol{v}$ defined as

$$\boldsymbol{v} = -\frac{1}{2}\beta(r)\alpha(R)\nabla K, \tag{1.64}$$

where

$$\beta(r) = -\frac{1}{\rho}\int_r^R \frac{\alpha(r')}{\alpha(R)}\frac{d\rho}{dr'} dr'. \tag{1.65}$$

From mixing length theory, the local turbulent viscosity can be approximated as $\nu = wl$ where w is the mean velocity of the turbulent eddies and l is the mixing length which refers to the size of the largest cells. As the tidal bulge moves around the star, this viscosity provides a dissipative mechanism for the tides. The rate of dissipation of the mechanical energy ε

through the star is

$$-\frac{d\varepsilon}{dt} = \frac{1}{2}\int \rho w l t_{ij}^2 dV = \frac{9M_2^2R^6}{2M_1^2(1-Q)^2} s_{ij}^2 \int_0^{M_1} wl\gamma(r)dm. \tag{1.66}$$

The rate of strain tensor is t_{ij} and s_{ij} is the symmetric, time dependent, space independent stress tensor. The masses of the primary and secondary stars are given by M_1 and M_2 respectively and

$$\gamma(r) = \beta^2 + \frac{2}{3}r\beta\beta' + \frac{7}{30}r^2\beta'^2. \tag{1.67}$$

The viscous time-scale of the convective region $\tau_{\rm visc}$ is defined by

$$\frac{1}{\tau_{\rm visc}} = \frac{1}{M_1R_1^2}\int_0^{M_1} wl\gamma(r)dm. \tag{1.68}$$

Care must be taken here to evaluate this only in the convective regions of the star. The tidal time-scale can be defined as

$$\tau_{\rm tide} = \frac{2\tau_{\rm visc}}{9}\frac{a^8}{R^8}\frac{M_1^2(1-Q)^2}{M_2(M_1+M_2)}, \tag{1.69}$$

where a is the binary separation. From this tidal time-scale, the rate of change of rotational angular velocity $\frac{d\Omega}{dt}$ can be found to be

$$\frac{d\Omega}{dt} = \frac{\omega}{\tau_{\rm tide}}\left(1-\frac{\Omega}{\omega}\right)\frac{M_2}{M_1+M_2}\frac{a^2}{R^2k_r^2}. \tag{1.70}$$

The radius of gyration of the star $k_{\rm r}^2$ refers to the distribution of the components of an object around its rotational axis. It is defined so that $k_{\rm r}^2 = I/MR^2$ where I is the moment of inertia of the star. Solving the first order differential equation 1.70 allows $\Omega(t)$ to be found. From this, the time taken to arrive at a synchronous state can be calculated as

$$\tau_{\rm sync} = \log\left(\frac{\omega-\Omega_0}{\omega-\Omega}\right)\frac{\tau_{\rm tide}(M_1+M_2)R^2k_r^2}{M_2a^2}. \tag{1.71}$$

It is assumed that the orbital angular velocity ω remains constant over these time-scales because the moment of inertia of an sdB star is small compared to that of the binary orbit.

The Relative Magnitude of Tidal and Rotational Distortions

Eggleton et al. (1998) calculate the distortion of a star owing to spin and tides in terms of a quadrupole tensor

$$q_{ij} = q_{\mathrm{rot}} l_{ij}(\hat{\boldsymbol{\Omega}}) + q_{\mathrm{tid}} l_{ij}(\hat{\boldsymbol{a}}), \tag{1.72}$$

where $\hat{\Omega}$ is a unit vector along the spin axis and $\hat{\mathbf{a}}$ is directed towards the companion and

$$l_{ij}(\boldsymbol{k}) = \frac{3k_i k_j - k^2 \delta_{ij}}{2k^5}, \tag{1.73}$$

for a general vector $\mathbf{k}$. The constants q_{rot} and q_{tid} can be related to the difference between the polar and equatorial radii $\Delta R_{\mathrm{rot}} \leqslant 0$ and $\Delta R_{\mathrm{tid}} \geqslant 0$ by $q = QM_1 R \Delta R$. So for the oblate spheroid rotational distortion

$$\frac{\Delta R_{\mathrm{rot}}}{R} = \frac{-\Omega^2 R^3}{2GM_1(1-Q)}, \tag{1.74}$$

where Ω is the spin frequency, R is the radius of the rotating star, M_1 is its mass and Q is the dimensionless tidal quadrupole moment obtained by solving Clairault's equation. The tidal distortion is a prolate spheroid symmetrical around the line connecting the centre of masses of the binary system and

$$\frac{\Delta R_{\mathrm{tid}}}{R} = \frac{3M_2 R^3}{2M_1 a^3(1-Q)}, \tag{1.75}$$

where M_2 is the companion mass and a is the binary separation. Kepler's second law can be used to re-express the binary separation in terms of the orbital angular velocity ω. For the tidal distortion to dominate, $|\Delta R_{\mathrm{tid}}| > |\Delta R_{\mathrm{rot}}|$, it is required that

$$M_1 < \left(3\left(\frac{\omega}{\Omega}\right)^2 - 1\right) M_2. \tag{1.76}$$

1.4.2 Zahn's Mechanism of Radiative Dissipation

Zahn (1975, 1977) developed a theory of dynamical dissipation for stars with radiative envelopes and convective cores. The periodic tidal potential induced by the companion star resonates with g-modes in the core. At the radiative boundary, these excited g-modes are damped. This provides a mechanism for tidal dissipation. The resultant characteristic synchronization time-scale is given by

$$\frac{1}{\tau_{\mathrm{sync}}} = 5 \cdot 2^{5/3} \left(\frac{g_{\mathrm{surf}}}{R}\right)^{1/2} k_r^2 \left(\frac{R}{a}\right)^{17/2} q^2 (q+1)^{5/6} E_2, \tag{1.77}$$

where $g_{\rm surf}$ is the surface gravity of the star and the mass ratio of the stars is $q = M_2/M_1$. The tidal coefficient E_2 describes the coupling between the tidal potential and the excited pulsations. It is highly dependent on the structure of the star and is defined as

$$E_2 = \frac{3^{8/3}\Gamma(\frac{4}{3})^2}{(2n+1)(2(2+1))^{4/3}} \frac{\rho R^3}{M} \left(\left(\frac{N^2}{x^2} \right)'_{\rm cc} \frac{\rho R^3}{g_{\rm surf}} \right)^{-1/3} H_2^2, \tag{1.78}$$

where $\Gamma(\frac{4}{3}) = 0.48060041894$ and x is the fractional radius r/R. The Brunt-Vaisala frequency N^2 characterises the buoyancy of material within the star. The primes denote derivatives with respect to x. The subscript cc refers to the convective boundary location. The quantity H_2 is

$$H_2 = \frac{2\times 2+1}{((n-3)Y(1)+Y'(1))X(x_{\rm cc})} \int_0^{x_{\rm cc}} \left(Y'' - 2(2+1)\frac{Y}{x^2} \right) X dx. \tag{1.79}$$

where Y is defined as

$$Y = \frac{x^2\Phi}{g}, \tag{1.80}$$

where Φ us the total gravitational potential. The Y can be described with

$$Y'' - \frac{6}{x}\left(1 - \frac{\rho}{\bar{\rho}}\right)Y' - \left(6 - 12(1 - \frac{\rho}{\bar{\rho}})\right)\frac{Y}{x^2} = 0, \tag{1.81}$$

which is evaluated throughout the star. Kopal (1989) uses the substitution

$$\eta_n(x) = \frac{x}{Y}Y', \tag{1.82}$$

in Eq. 1.81, subject to the boundary conditions $Y(0) = 0$ and $\eta_n(0) = n+1$, to find Y. The X is a structural quantity defined as

$$X = \rho x^2 \chi', \tag{1.83}$$

where χ is the sum of the perturbation to the gravitational potential and the relative density. The X is given by the solution to the differential equation

$$X'' - \frac{\rho'}{\rho}X' - \frac{6}{x^2}X = 0. \tag{1.84}$$

The requirement that $\chi(0) = 0$ and $\chi'(0) = 0$ gives the boundary conditions

$$X(0) = 0, \quad X'(0) = 0, \tag{1.85}$$

and is only evaluated in the convective region. This description of tidal dissipation doesn't consider the effect of the convective dissipation. This theory again models the tidal bulge as a second order Legendre polynomial.

1.5 Thesis Outline

The overall intention of this thesis is to use sdB stars as a laboratory to investigate tidal interactions. Chapter 2 discusses the stellar evolution code used and the methods for creating detailed stellar models. RGB stars are progenitors of sdBs and a significant portion of Chapter 2 focuses on the modelling of these stars. RGBs can straightforwardly be modelled with the STARS code without having to take intermediate stages making them good objects to study to learn how to use the code. The RGB work focuses on the first dredge up phase and the resulting chemical evolution of the surface of the stars. The RGB models created for this project were used as intermediaries for the sdB models.

Chapter 3 discusses the tidal interactions in sdB systems which have lost their envelopes via common-envelope evolution. Chapter 4 looks at what modifications to standard stellar models created with regular input physics are required in order for tidal synchronization to be achieved. In Chapter 5 the effect of tidal distortions on the observable pulsation eigenfrequencies is considered. Stellar pulsation theory relies on the assumption of spherical symmetry of the star. The sdB stars with close companions experience sufficiently substantial tidal distortions that this spherical symmetry is broken. Chapter 6 concludes this thesis and discusses the implications of the results obtained.

Chapter 2

Modelling Stars

Owing to the complexity of the physical processes occurring in stars and the non-linearity of the equations much of the theoretical work carried out in the field is computational. Stellar models are an important tool to analyse the effectiveness of a theory and the interpretation of observations.

2.1 The STARS Code

The STARS code is a stellar evolution code developed by Eggleton (1971, 1972). It has been in continuous use since its creation and has been updated a number of times over the years. It was originally written in Fortran 4 then upgraded to Fortran 77 in Pols et al. (1995). The code solves the four time-dependent equations of stellar structure, five equations governing composition changes and one of two equations for the spacing of the mesh. It treats a star as a sequence of thin concentric shells and uses an adaptive non-Lagrangian mesh to distribute the shells across the star. The code is compact and produces effective models with as few as 199 shells. The opacity is read in as OPAL (Iglesias and Rogers, 1996) style tables which allow for varying carbon and oxygen abundances (Eldridge and Tout, 2004). It is capable of evolving both stars in a binary system as well as their orbit (Stancliffe and Eldridge, 2009). With some encouragement it can also evolve thermally pulsing AGB stars. Unfortunately, the code cannot evolve stars with solar metallicity and $M < 2.25\,\mathrm{M}_{\odot}$ through He ignition without taking some intermediate steps because of the violence of the He flash. The code utilises twenty subroutines, requires two input files and produces three standard output files.

2.1.1 The Equations of Stellar Evolution

When stars form they consist of predominantly hydrogen. When nuclear reactions begin the chemical composition and structural properties of a star undergo many changes. Stellar evolution codes numerical solve the equations of stellar structure and evolution to create detailed, numerical evolutionary models. The following coupled partial differential equations dictate the properties of a star. The equation of continuity is

$$\frac{\partial r}{\partial m} = \frac{1}{4\pi r^2 \rho}, \tag{2.1}$$

where r is the radius, m is the mass and ρ is the density. The requirement of hydrostatic equilibrium of the material, where gravitational inward forces are balanced by the pressure of the stellar material, gives

$$\frac{\partial P}{\partial m} = -\frac{Gm}{4\pi r^4}. \tag{2.2}$$

where P is the pressure. The first law of thermodynamics gives the energy balance

$$\frac{\partial L_r}{\partial m} = \varepsilon_{\rm nuc} - \varepsilon_{\nu} - T\frac{\partial s}{\partial t}, \tag{2.3}$$

where L_r is the internal luminosity, T is the temperature. s is the entropy, t is time, $\varepsilon_{\rm nuc}$ is the energy generated by nuclear reactions and ε_{ν} is the energy lost in neutrinos. During the red giant phase when the temperature and density of the inert deuterium core is very high neutrinos are emitted by spontaneous weak interactions. They escape without interacting with the stellar material and carry their energy away with them which causes the region of highest temperature to drift off-centre. When He ignites it does so at $T_{\rm max}$ and thus is off-centre. The heat transport is

$$\frac{\partial T}{\partial m} = -\frac{Gm}{4\pi r^4}\frac{T}{P}\nabla, \tag{2.4}$$

where the thermodynamic gradient ∇ is dependent on whether energy transport is by convection or radiative transfer. If the material is radiative then

$$\nabla = \nabla_{\rm rad} = \frac{3\kappa P L_r}{16\pi acGmT^4}, \tag{2.5}$$

where a is the radiation constant and c is the speed of light. In convective regions $\nabla = \nabla_{\rm mlt}$ which is determined from mixing length theory (Böhm-Vitense, 1958). Two different criterion's are used to determine if the local material is stable against convection. The Schwarzschild (1958) criterion states that the material is convective if $\nabla_{\rm rad} > \nabla_{\rm ad}$. The

Ledoux (1947) criterion states that energy transport is by convection if

$$\nabla_{\rm rad} > \nabla_{\rm ad} + \frac{\Phi}{\delta}\nabla_\mu \qquad (2.6)$$

where

$$\nabla_\mu = \left(\frac{\partial \ln \mu}{\partial \ln p}\right),\ \Phi = \left(\frac{\partial \ln p}{\partial \ln \mu}\right)\Bigg|_{P,\mu},\quad \delta = -\left(\frac{\partial \ln \rho}{\partial \ln T}\right)\Bigg|_{P,T} \qquad (2.7)$$

where μ is the mean molecular weight. The Ledoux criterion stabilises regions which would be unstable with the Schwarzschild criterion. The chemical evolution of the jth element is

$$\frac{\partial}{\partial m}\left(\sigma\frac{\partial X_i}{\partial m}\right) = \frac{m_i}{\rho}\sum_j \alpha_{ij} r_j + \frac{\partial X_i}{\partial t}, \qquad (2.8)$$

where X_i is the mass fraction of the ith element, m_i the mass of a nuclide of type i, α_{ij} is the number of particles of nuclide i created in reactions of type j and r_j is the reaction rate density. The convective diffusion coefficient is labelled σ and is zero in radiative regions. In convective regions $\sigma = K(\nabla - \nabla_{\rm ad})^3 M^2/t_{\rm nuc}$ where K is a constant and $t_{\rm nuc}$ is the nuclear timescale.

2.1.2 Boundary Conditions

Solving any differential equation requires boundary conditions. The STARS code boundary conditions are set such that in the core where $m = 0$

$$r = 0, L_r = 0, \frac{\partial P}{\partial m} = 0, \sigma\frac{\partial X_i}{\partial m} = 0, \qquad (2.9)$$

where the final boundary condition ensures the composition gradient is continuous. At the surface where $m = M$

$$l = \pi acr^2 T^4, P = \frac{2}{3}\frac{Gm}{\kappa r^2}\left(1 + \frac{L_r}{L_{\rm edd}}\right), \sigma\frac{\partial X_i}{\partial m} = 0, \frac{dM}{dt} = f_{\dot{M}}(M, R, L, X_{i,s}). \qquad (2.10)$$

where $f_{\dot{M}}$ is the mass loss rate, $L_{\rm Edd}$ is the Eddington luminosity and κ is the opacity. The code has routines for Reimers, Blöcker, Vassiliadis & Wood and Wolf-Rayet (Nugis and Lamers, 2000) mass-loss prescriptions. Reimers (1975a,b) Law describes the mass-loss rate for late-type giants and supergiants. Bloecker (1995)'s prescription is for mass-loss on the asymptotic giant branch (AGB) and is based on simulations of shock-driven winds in the astomspheres of Mira-like stars. Vassiliadis and Wood (1993)'s mass-loss is also for AGB stars and is based on observations of dust-enshrouded stars OH/IR stars.

2.1.3 Differential Equation Solvers

The differential equations are solved numerically with a Heyney method and a Newton-Raphson iterative solution scheme. One assumes spherical symmetry of the star then divides the star into a series of concentric spherical shells. This set of spherical shells forms the mesh. The differential equations are solved by examining differences between adjacent meshpoints. The code automatically decides the timestep interval. Each iteration the equations need to be solved for the current model at $t = t_0 + \Delta t$, where Δt is the timestep and t_0 refers to the previous model.

The Heyney method uses implicit integration starting with an initial stellar model. The derivatives of all variables are calculated to form an invertable matrix. This is iterated over with the Newton-Raphson method to find the evolutionary model at the next timestep.

2.1.4 The Mesh Spacing Function

Some stellar evolution codes adopt a Lagrangian mesh with the spherically symmetrical shells placed at fixed mass co-ordinates. As a modelled star evolves its structure changes substantially making the Lagrangian mesh inefficient, particularly in regions with shell burning. The STARS code uses an self-adaptive non-Lagrangian mesh to position the points. The mesh spacing function

$$
\begin{aligned}
q = c_4 \ln P + c_5 \ln\left(\frac{P+c_9}{P+c_{t1}}\right) + c_2 \ln\left(\frac{P+c_{10}}{P+c_{t1}}\right) + c_7 \ln\left(\frac{T}{T+c_{t10}}\right) \\
- \ln\left[\frac{1}{c_6}\left(\frac{m}{M}\right)^{2/3} + 1\right] - c_3 \ln\left(\frac{r^2}{c_8} + 1\right),
\end{aligned}
\tag{2.11}
$$

depends on P, T , m and r. Mesh points are placed at equal intervals of q. The mesh spacing function is chosen such that regions with rapidly changing quantities contain more mesh points. The c_i mesh spacing coefficients are user defined and can be modified so the mesh responds to the desired physical property.

2.1.5 Convection

In the STARS code mixing length theory as described by Böhm-Vitense (1958) is used. Near the core the pressure scale height $H_P \to \infty$. The mixing length l is defined to be αH_P and sets the average distance travelled by convective elements. The mixing length parameter α is a user defined constant. Physically, convective elements cannot travel an infinite distance. As suggested by Eggleton (1972), the mixing length is modified such that it cannot exceed the distance to the edge of the convective zone. This also has an effect on the mixing velocity w.

Semi-Convection and Convective Overshooting

Eggleton (1972) implemented semi-convection in STARS as a diffusive process which follows Schwarzschild and Härm (1958)'s prescription. It assumes that the energy transport by convection in the semi-convective region is borderline negligible but that there is substantial chemical mixing which avoids any discontinuity in the chemical profile. The code defines semi-convective regions as those with $\nabla_{\rm r} \approx \nabla_{\rm a}$.

For convective overshooting we introduce a parameter δ such that convection occurs when

$$\nabla_{\rm r} - \nabla_{\rm a} > -\delta, \tag{2.12}$$

where $\nabla_{\rm r}$ and $\nabla_{\rm a}$ correspond to the radiative and adiabatic thermodynamic gradients $\partial \ln T / \partial \ln P$, respectively, and where the overshooting parameter δ is

$$\delta = \frac{\delta_{\rm ov}}{2.5 + 20\zeta + 16\zeta^2}. \tag{2.13}$$

Here ζ is the ratio of radiation pressure to gas pressure and $\delta_{\rm ov}$ is a user defined parameter calibrated to observations. Typically $\delta_{\rm ov} = 0.12$ gives the best fit to ζ Aur giants in well observed binary systems (Schröder et al., 1997).

2.1.6 Opacity

Opacity measures the degree to which photons are absorbed by matter. The opacity of the material is one of the dominant factors in governing whether a star transports its energy by convection or radiative transfer. There are four major sources of opacity in stars. Electron scattering occurs when photons cause electrons to oscillate and radiate in another direction. Electron scattering is important when the matter is ionized at high temperatures. Free-free absorption occurs when an electron in the vicinity of a charged ion absorbs an incident photon. Bound-free absorption is the absorption of a photon by a bound electron where the ionization energy of the atom is lower than the energy of the incident photon. The H^- ion makes an important contribution to the bound-free opacities as do H_2 and molecules such as water. Bound-bound absorption occurs when matter changes energy level and either emits or absorbs a photon. Predicting the opacity of stellar matter is a complex procedure so the STARS code uses OPAL opacity tables. Cubic splines are set up across the opacity tables which can than be interpolated for different local densities and temperatures. To reduce the size of the tables the code uses R as a proxy variable for density defined such that $R = \rho/T_6^3$. The code has been updated to track changing C/O levels. Opacity tables for varying metallicities are available.

2.1.7 The Equation of State

The equation of state relates properties of the star to each other. The STARS code uses temperature and a quantity f which relates to the electron degeneracy parameter

$$\psi = \frac{\mu_e'}{kT}, \tag{2.14}$$

where μ_e' is the electron chemical potential and k is the Boltzmann constant. The parameter f used in the equation of state is defined such that

$$\psi = 2\sqrt{1+f} + \ln\left(\frac{\sqrt{1+f}-1}{\sqrt{1+f}+1}\right). \tag{2.15}$$

To solve the equations of stellar structure and evolution $\rho(f,T)$, $S(f,T)$ and $P(f,T)$ are all required. Several sources contribute to the equation of state and so they are generally written in the form $P = P_e + P_i + P_r + P_c$ where the subscripts refer to the electron contribution, the ionic contribution, the radiation contribution and the pressure ionization plus other corrections including plasma. For a given ψ, T and composition all the thermodynamic properties of the star can be calculated.

2.2 Creating sdB Models

The sdBs are low-mass stars with burning He cores. The He can ignite degenerately in a He-flash or non-degenerately if the progenitor mass is over $2.25\,M_\odot$. Modelling sdBs in the STARS code presents two challenges, getting the stars through the He-flash and removing the envelope. The STARS code cannot ignite He in this manner without intermediate steps being taken. The established procedure for $Z = 0.02$ is to start with both a $3\,M_\odot$ and a star with the desired initial mass. Allow the higher mass star to ignite He under non-degenerate conditions and evolve the lower mass star until it breaks down on the RGB. Once the non-degenerate ignition has been achieved, the conversion of elements via nuclear reactions is stopped and mass is slowly removed from the star to get it down to the mass of the lower mass star just before it breaks down on the RGB. Next, the core which has He burning is put into the envelope of the lower mass star with the degenerate core. Larger stars have smaller He-cores so some H is allowed to fuse to get the core mass to correspond to the new mass of the star. Now, the composition of the substituted core is slowly modified to recover the H gradient of the lower mass star at the end of the main-sequence. At this stage, the star is burning He stably in its core. A very high mass loss is required to remove sufficient envelope for the star to be considered a sdB. If the mass-loss is introduced too quickly the star goes in to shock and fails to converge. To avoid this, I have updated the STARS code mass-loss routine to allow for an increasing mass-loss rate. Using the above method I have created sdBs with typically observed effective temperatures, surface gravities and masses as can be seen in Fig 2.1.

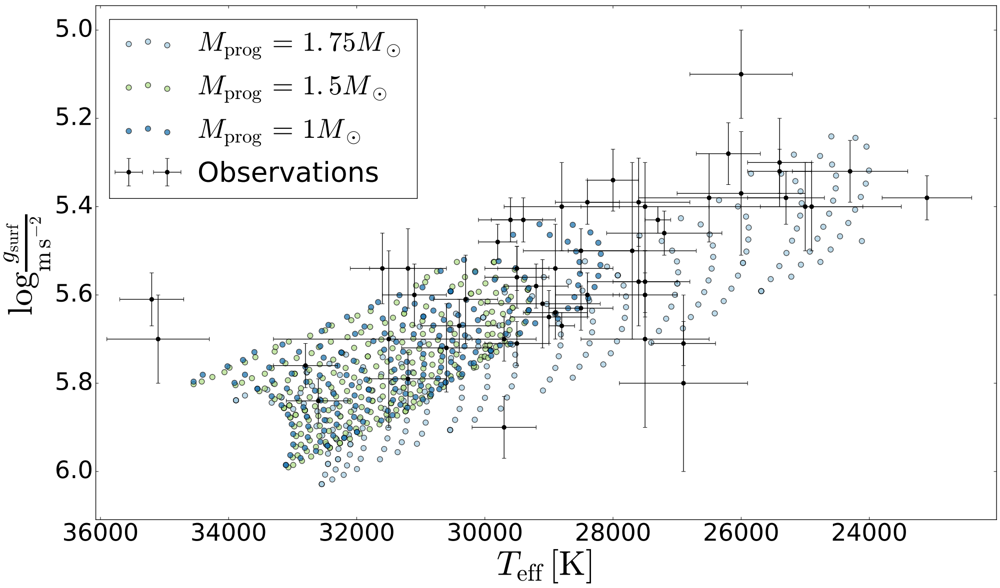

Fig. 2.1 A $T_{\rm eff}$ - $\log_{10}(g_{\rm surf}/{\rm cm\,s^{-2}})$ plot of generated sdB models.

2.3 The Red Giant Branch and First Dredge Up

RGB stars are progenitors to sdB stars and can be created with the stars code without having to take any intermediate artificial steps. First dredge up occurs as a star ascends the red giant branch after crossing the Hertzsprung gap as shown in Figure 2.2. During this phase, a convective envelope extends through the star into regions which have previously been fusing hydrogen as shown in Figure 2.3. The convective areas are then mixed, bringing the products of the fusion to the surface of the star as seen in Figure 2.4 which alters the surface composition. The dredge up also causes an internal composition discontinuity to form at the deepest extent of the convective envelope. When the H burning shell reaches this discontinuity there is a non-monotonic variation in the luminosity known as the red-giant bump (Iben, 1968).

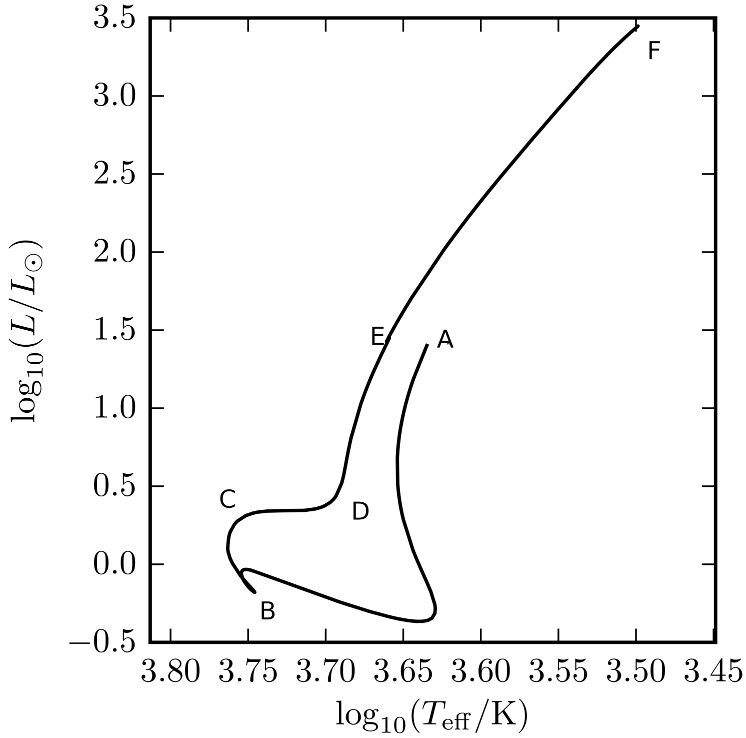

Fig. 2.2 A 0.995M$_\odot$ star evolving from its pre-main sequence, A) down the Hayashi track B) through the main sequence, C) across the Hetzsprung gap D) up the red giant branch E) through the red giant bump F) ending with breakdown just before degenerate He ignition. The deepest extent of first dredge up occurs when $\log_{10}(T_{\rm eff}/K) = 3.675$, $\log_{10}(L/{\rm L}_\odot) = 1.00$. The model breaks down just before the He flash as L approaches $10^{3.5}\,{\rm L}_\odot$. The red giant luminosity bump is visible.

2.3.1 Modelling the First Dredge Up

Using the STARS code I created a grid of 420 evolutionary models simulating the first dredge up phase. The grid had seven metallicities, $Z \in \{0.0001, 0.0003, 0.001, 0.004, 0.008, 0.02, 0.03\}$. The mass fraction of the star which is not H or He is given by Z. The intial Z distribution is that of Anders and Grevesse (1989). Each metallicity set consisted of 60 stars distributed logarithmically in mass from 0.8 $M_\odot$ to 20 $M_\odot$. The simulations were run from the pre-main sequence to beyond the first dredge up and were allowed to continue until the code broke down. For low-mass stars the code breaks down when the He flash is reached. For higher mass stars, He ignition is achieved and the code breaks down on the AGB when thermal pulses begin.

The investigated quantities were the change in the surface abundances of carbon and nitrogen as a result of dredge up [C/N], the deepest extent of the convective envelope during the dredge up, the surface gravity of the star when the envelope is fully extended and the full internal chemical composition details of each model at the terminal-age main sequence (TAMS). The TAMS corresponds to the evolutionary stage where core H is exhausted and nuclear burning is quenched. The quantity [C/N] is

$$[\mathrm{C/N}] = \log_{10} \frac{\mathrm{n_{C,f}}}{\mathrm{n_{C,i}}} - \log_{10} \frac{\mathrm{n_{N,f}}}{\mathrm{n_{N,i}}}, \tag{2.16}$$

where $n_{\mathrm{C,f}}$ is the post dredge up number fraction of the surface which is carbon, $n_{\mathrm{C,i}}$ is the initial number fraction of the surface which is carbon while $n_{\mathrm{N,i}}$ and $n_{\mathrm{N,f}}$ are defined in the same way for the nitrogen abundances before and after dredge up.

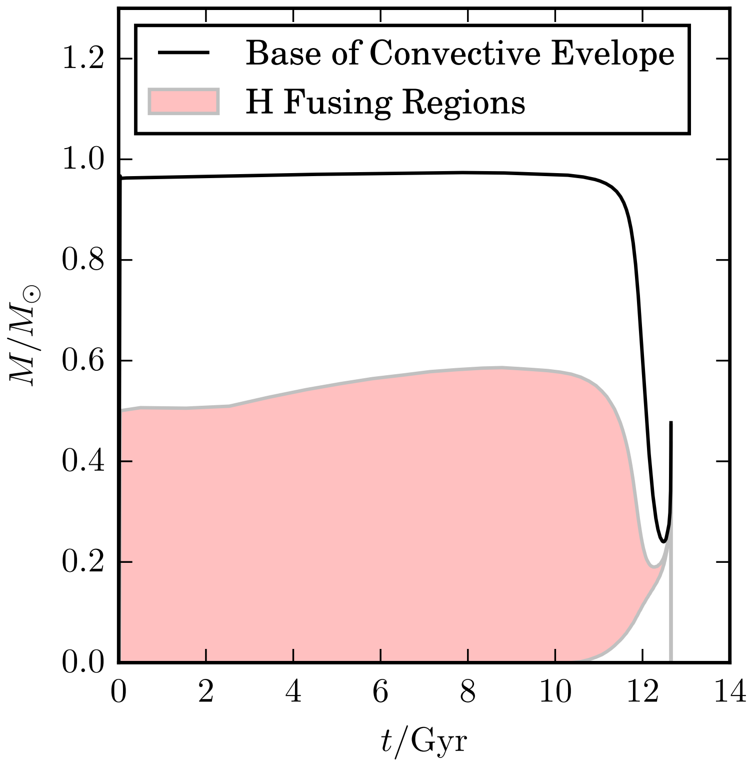

Fig. 2.3 The convective envelope boundary in a 0.995 $M_\odot$ star for same path of evolution as shown in Figure 2.2. First dredge up commences when the envelope begins to descend. The shaded region represents areas with significant nuclear burning.

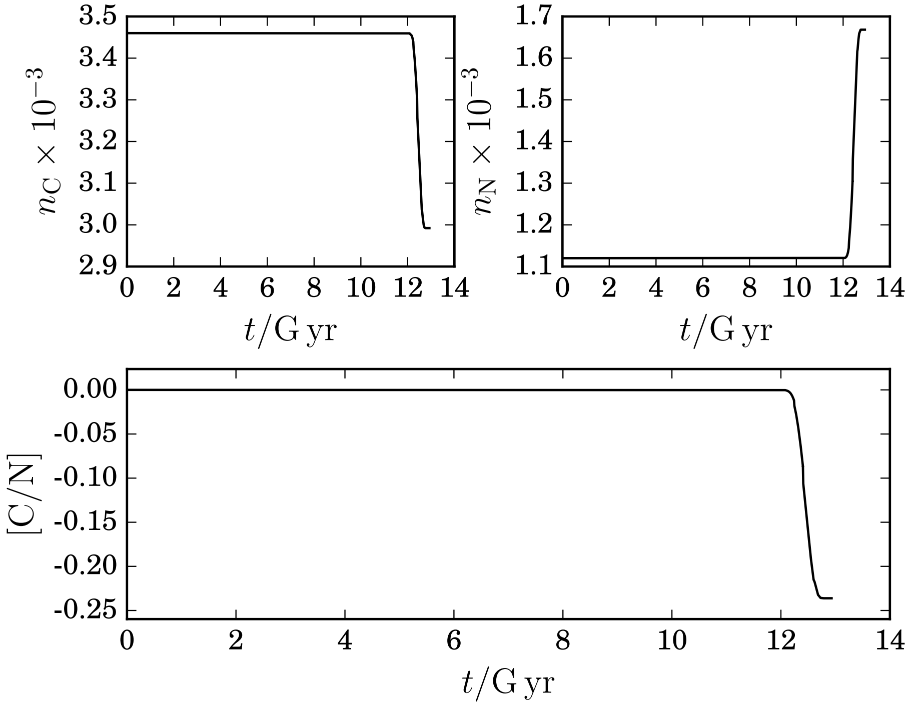

Fig. 2.4 Plot of the number fraction of surface carbon abundance (top left) number fraction surface nitrogen abundance (top right) and ratio of carbon to nitrogen (bottom) all as a function of time for a $0.995\,\mathrm{M}_{\odot}$ evolving star. The surface abundance refers to the total mass fraction of the relevant element in the outermost shell at which the photospheric boundary conditions are satisfied.

2.3.2 Metallicity

Lower metallicity stars have larger and hotter cores so they evolve more quickly. The time taken to go from the pre-MS to first dredge up is illustrated for two $0.8\,\mathrm{M}_{\odot}$ stars, with metallicities $Z = 0.02$ and $Z = 0.0001$, in Figure 2.5. The star with $Z = 0.02$ takes about twice as long to reach first dredge up.

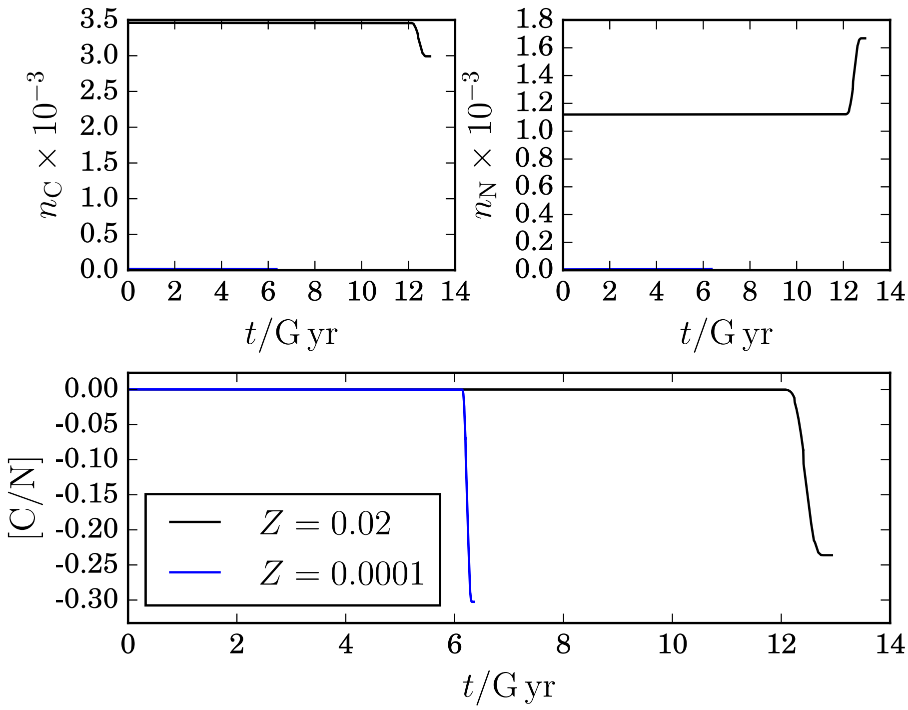

Fig. 2.5 The surface carbon abundance (top left), surface nitrogen abundance (top right) and ratio of carbon to nitrogen (bottom) all as a function of time for a $0.8\,\rm M_\odot$ evolving star. The black line shows a $Z = 0.02$ star and the blue line shows a $Z = 0.0001$ star. As observed dredge up occurs much sooner for the lower metallicity star.

Changing the metallicity also has a fairly significant effect on other phases of a star's evolution. At subsolar metallicities stars more massive than a Z dependant threshold ignite He without any first dredge up. Both of these effects are illustrated in Figure 2.6. Table 2.1 shows the highest mass at which subsolar metallicity stars experience first dredge up.

Table 2.1 Table of maximum mass of star experiencing first dredge up

Metallicity	Max Mass for First Dredge Up /$M_\odot$
0.0001	2.38229
0.0003	2.96330
0.001	6.36075
0.004	10.9764
0.008	11.5919

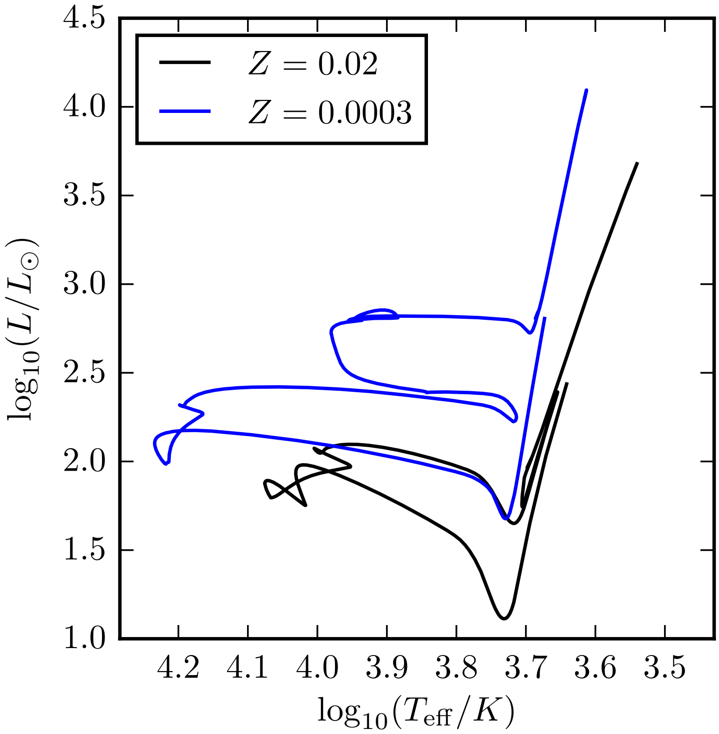

Fig. 2.6 Two $3\,M_{\odot}$ stars evolving from the pre-main sequence, through the main sequence, across the Hertzsprung gap and up the red giant branch. The plot includes $Z = 0.0001$ (blue) and $Z = 0.02$ (black). The lower metallicity star has a larger luminosity and effective temperature and at this mass does not experience a first dredge up. Instead He ignites in the Hertzsprung gap before any red giant evolution.

2.3.3 Accuracy

It quickly became clear that the C and N fractional abundances were not well calculated by the code for the sub-solar metallicity, low-mass stars as illustrated in Figure 2.7. This problem was overcome by changing the accuracy with which the equations are solved by reducing the size of the fractional difference of the increments taken during the numerical differentiation of stellar variables, for the Newton-Raphson scheme, from 10^{-6} to 3×10^{-8} and generating a new set of models.

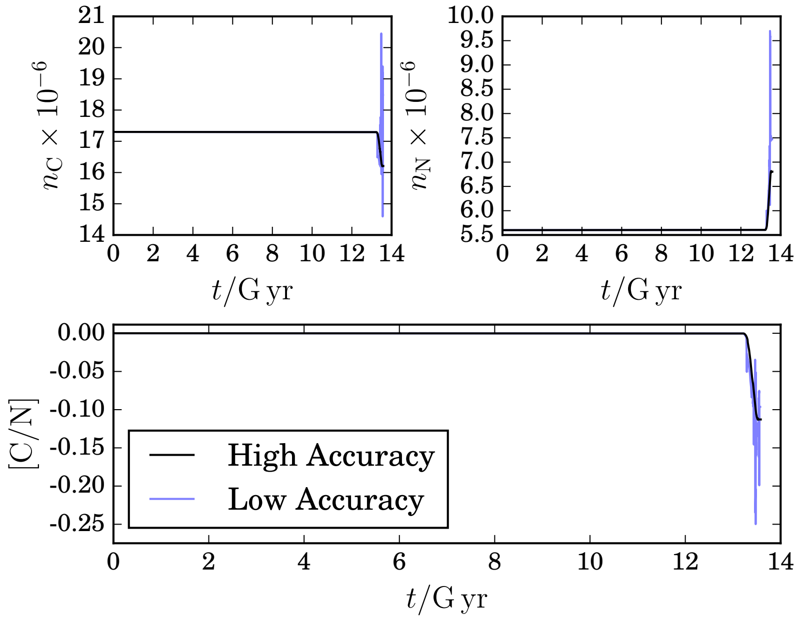

Fig. 2.7 The surface carbon abundance (top left) surface nitrogen abundance (top right) and ratio of carbon to nitrogen (bottom) all as a function of time for a $Z = 0.0001$, $0.8\,\mathrm{M}_\odot$ star. The blue line shows the models tracking C and N poorly. The black line shows the corrected models which solve the differential equations with greater accuracy.

2.3.4 Comparison of the First Dredge Up Result with the Terminal Age Main-Sequence Model

Theoretically, no nuclear burning occurs in the dredged regions between the TAMS and first dredge up. This means convective mixing can be approximated by averaging the composition of the TAMS model down to the depth of the envelope at its deepest extent during dredge up. It was discovered that the [C/N] ratio changed significantly between the TAMS and the first dredge up as can be seen in Figures 2.8 and 2.9. The nuclear energy generation rate $\varepsilon_{\mathrm{nuc}}$ was checked in the stars between the TAMS and first dredge up to confirm that no nuclear fusion occurred to account for this discrepancy.

The next attempted solution to this problem was to redefine the TAMS. Initially, the TAMS was defined as when core hydrogen abundance drops below 0.01, because it was thought that negligible burning would take place after this. I showed this assumption to be incorrect and so the TAMS was redefined as $\mathrm{X_H} < 10^{-7}$. This improved the situation but did not fully resolve it. Eventually I found the problem to be caused by numerical diffusion across the envelope boundary region.

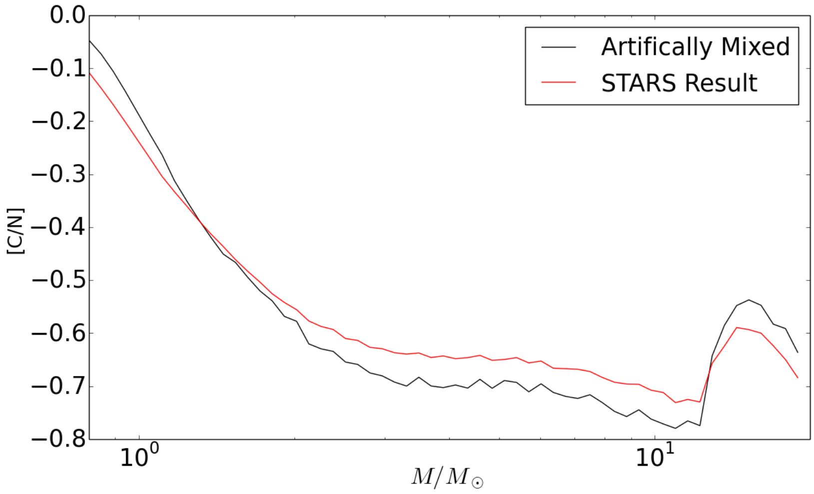

Fig. 2.8 The change in surface [C/N] for all the $Z = 0.02$ stars. The models artificially mixed at the terminal age main sequence (black) had ratios of up to 0.06 dex, or a factor of $10^{0.06}$, away from those computed after first dredge up (red).

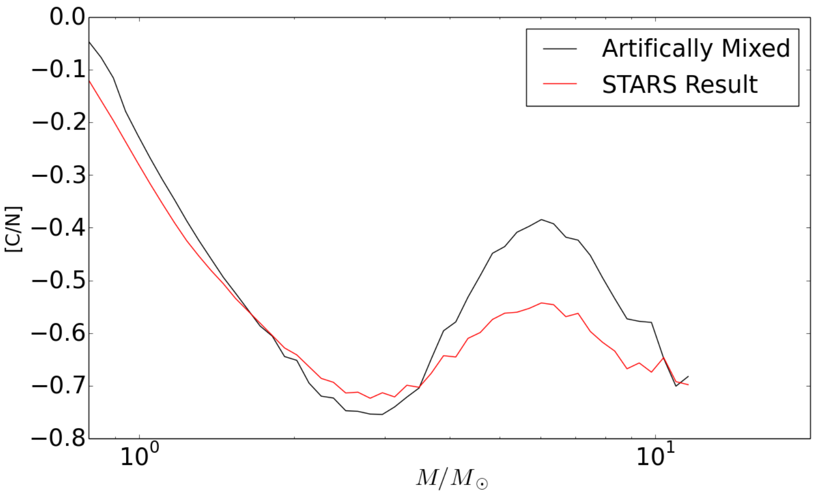

Fig. 2.9 The $Z = 0.004$ results in the same configuration as Figure 2.8. In this case the artificial results differed by up to, and in some cases over, 0.2 dex for the models over 4 $M_\odot$.

2.3.5 High Resolution Results

The STARS code suffers from numerical diffusion across boundary regions owing to the movement of the mesh points relative to mass shells as the model evolves. Increasing the number of shells evaluated significantly reduces the amount of numerical diffusion. Increasing the number of shells in the model altered the [C/N] ratios found both at the TAMS and during dredge up. A full data set with 999 meshpoints was created and all of the dredge up models varied by less than 2.3 % when compared to their artificially mixed TAMS counterparts as can be seen in Figures 2.10 and 2.11. This is a substantial improvement from the low resolution models in Figures 2.8 and 2.9. Figure 2.12 compares the high resolution and low resolution results of all the $Z = 0.004$ models which experienced a first dredge up. The $Z = 0.004$ data set is displayed here because the effects of numerical diffusion were most pronounced in the lower metallicity, higher mass stars because the abundances of the metals are lower.

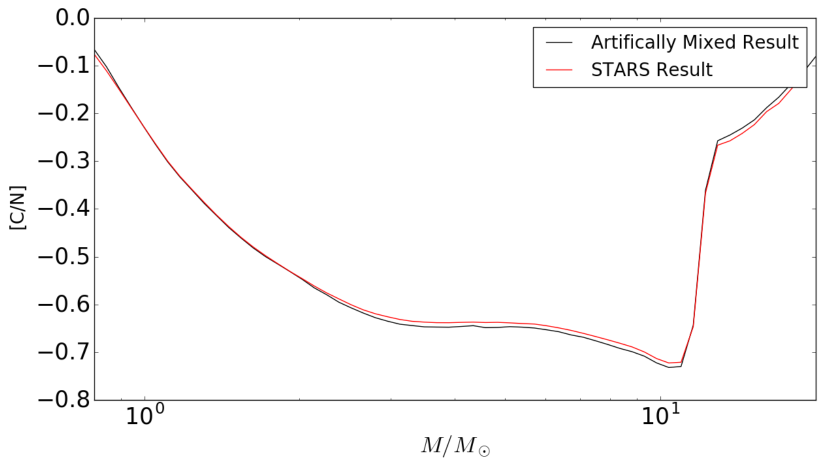

Fig. 2.10 The change in surface [C/N] for all the $Z = 0.02$ stars when run at high resolution. The models artificially mixed at the terminal age main sequence (black) had ratios of less than 0.01 dex away from the computed surface values after first dredge up (red).

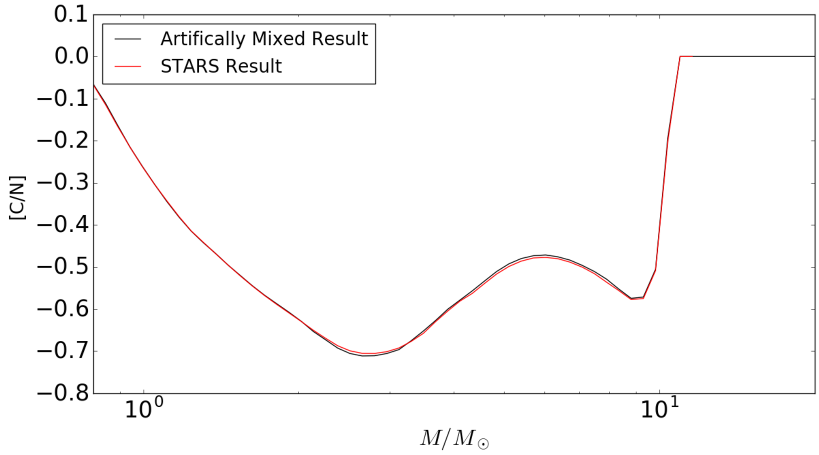

Fig. 2.11 The $Z = 0.004$ results in the same configuration as Figure 2.10.

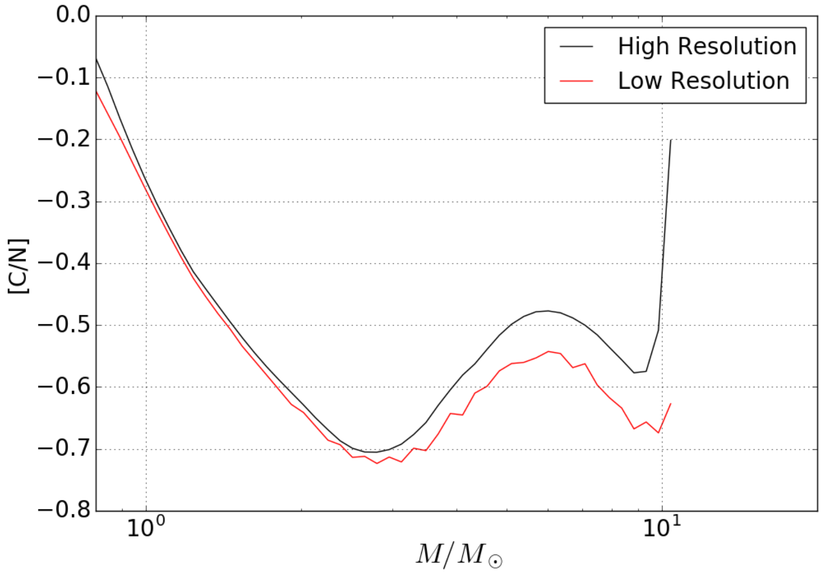

Fig. 2.12 The change in ratios of [C/N] for all the $Z = 0.004$ models experiencing first dredge up. The low resolution models (red) had 199 shells and the high resolution set had 999 shells (black). The higher resolution models have a systematically smaller [C/N] although the effect is most significant at higher masses.

In addition to changing the abundance profiles, adding more shells to the model had a small but noticeable effect on the evolution of the stars across the Hertzsprung gap. The code always makes the outer 25 meshpoints of the star convective for numerical stability. Changing the number of mesh points also changes the location of the outermost convective region and hence alters the surface evolution in phases which have rapidly changing quantities. The evolutionary tracks placed on an H-R diagram for a 5 $M_\odot$ star modelled with high and low resolution can be seen in Figure 2.13.

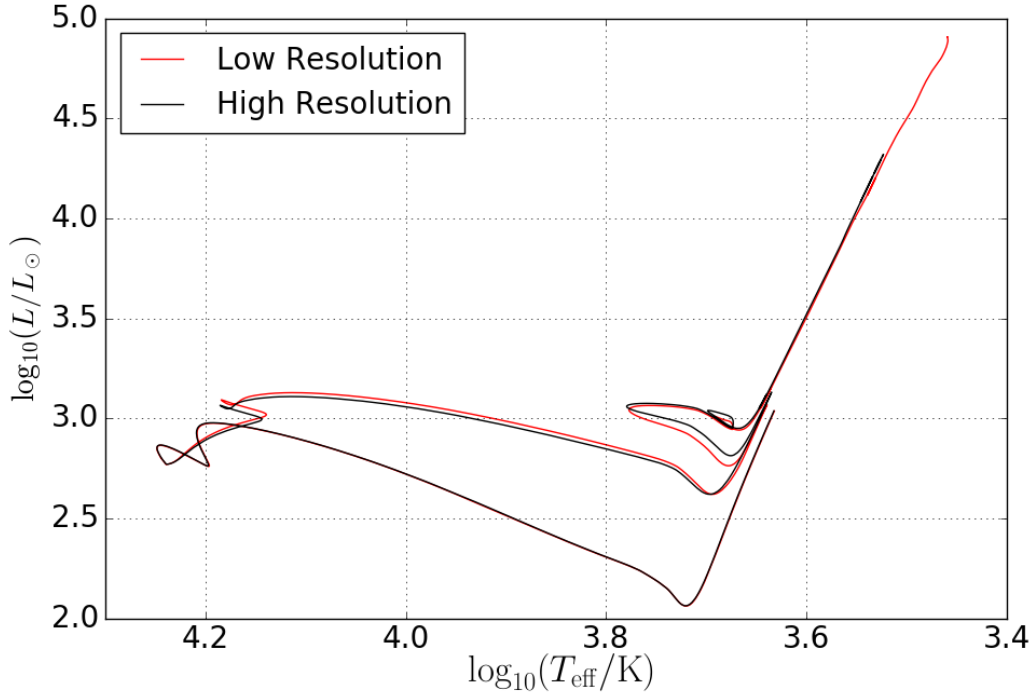

Fig. 2.13 Increasing the number of shells in the model has an effect on the macroscopic evolution. The high-resolution models (black) are less luminous between the late main-sequence and first dredge up than their low resolution counterparts (red).

2.3.6 Application of RGB Models to Binary Stars in the Thick Disc

Izzard et al. (2018) implemented abundance changes at first dredge up of the above `STARS` models into the `BINARY_C` population-nucleosynthesis code (de Mink et al., 2014; Izzard et al., 2004) to investigate the role of the binary interactions on the Galactic thick disc evolution. The combination of asteroseismologically measured masses with abundances from detailed analyses of stellar atmospheres challenges our fundamental knowledge of stars and our ability to model them. Ancient red-giant stars in the Galactic thick disc are proving to be most troublesome in this regard. They are older than 5 Gyr, a lifetime corresponding to an initial stellar mass of about 1.2 $M_\odot$. So why do the masses of a sizeable fraction of thick-disc stars exceed 1.3 $M_\odot$, with some as massive as 2.3 $M_\odot$? We answer this question by considering duplicity in the thick-disc stellar population using a binary population-nucleosynthesis model. We examine how mass transfer and merging affect the stellar mass distribution and surface abundances of carbon and nitrogen. We show that a few per cent of thick-disc stars can interact in binary star systems and become more massive than 1.3 $M_{\odot}$. Of these stars, most are single because they are merged binaries. Some stars more massive than 1.3 $M_{\odot}$ form in binaries by wind mass transfer. We compare our results to a sample of the APOKASC data set and find reasonable agreement except in the number of these thick-disc stars more massive than 1.3 $M_{\odot}$. This problem is resolved by the use of a logarithmically flat orbital-period distribution and a large binary fraction.

2.4 GYRE

GYRE is an open source, stellar oscillation code which solves the adiabatic and non-adiabatic pulsation equations with the Magnus Multiple Shooting numerical scheme for a given input model (Townsend et al., 2018; Townsend and Teitler, 2013). The code was created by Richard Townsend and Seth Tietler and was made publicly available in 2013. The adiabatic suite can be used to find the periods of the possible pulsation modes but does not calculate their stability. The non-adiabatic code uses the adiabatic eigenfrequencies as initial parameters and calculates the period and stability of the pulsation modes. GYRE accepts a number of different stellar model input formats but is not directly compatible with the STARS code output. To analyse the pulsations of STARS code models, I have designed a back end for the STARS code to output models in the appropriate format. Once GYRE accepts STARS models as inputs I can examine the stability and frequency spectrum of the models I have created. The quantities needed for GYRE inputs are shown in Table 2.2

I have modified the code such that all output models are written into two files, one in the format required for STARS and one which can be used as input for GYRE. Many of the required quantities are calculated in STARS or can be calculated without major modifications to the code. The necessary thermodynamic quantities can be calculated within the `statef` subroutine. The STARS opacity is read in as a temperature and density table. The code uses a bicubic spline interpolation to find κ for a given set of conditions within the star. Bicubic spline interpolation treats the table as a surface. The height of the surface $p(x, y)$ can be described with the sixteen nearest points as

$$p(x,y) = \sum_{i=0}^{3}\sum_{j=0}^{3} a_{ij}x^i y^j, \tag{2.17}$$

where x and y are the two dimensions of the table and a_{ij} are 16 coefficients which must be calculated. The partial derivatives of $p(x, y)$ with respect to x and y are then

$$p_x(xy) = \sum_{i=1}^{3}\sum_{j=0}^{3} a_{ij}ix^{i-1}y^j, \tag{2.18}$$

and

$$p_y(xy) = \sum_{i=0}^{3}\sum_{j=1}^{3} a_{ij}jx^i y^{j-1}. \tag{2.19}$$

Equations 2.15, 2.16 and 2.17 can be used to find κ_{T} and κ_ρ.

Table 2.2 Table of inputs required for GYRE.

Column	Variable	Datatype	Definition
Header	n	integer	Number of grid points
Header	M	real	Stellar mass /g
Header	R	real	Stellar radius /cm
Header	L	real	Stellar luminosity /erg s^{-1}
1	k	integer	Grid point index ($k = 1, \ldots, n$)
2	r	real	Radius /cm
3	M_r	real	Interior mass /g
4	L_r	real	Luminosity /ergs^{-1}
5	P	real	Total pressure /dyne cm^{-2}
6	T	real	Temperature /K
7	ρ	real	Density / $\mathrm{g\,cm}^{-3}$
8	∇	real	$d\ln T/d\ln p$
9	N^2	real	Brunt-Väisälä frequency squared /s^{-2}
10	Γ_1	real	$(\partial \ln P/\partial \ln \rho)_{\mathrm{ad}}$
11	∇_{ad}	real	$(d\ln T/d\ln P)_{\mathrm{ad}}$
12	δ	real	$-(\partial \ln \rho/\partial \ln T)_P$
13	κ	real	Opacity ($\mathrm{cm}^2\mathrm{g}^{-1}$)
14	κ_T	real	$(\partial \kappa/\partial \ln T)_\rho$ /$\mathrm{cm}^2\,\mathrm{g}^{-1}$
15	κ_ρ	real	$(\partial \kappa/\partial \ln \rho)_T$ /$\mathrm{cm}^2\,\mathrm{g}^{-1}$
16	ε	real	Energy generation/loss rate /erg $\mathrm{s}^{-1}\,\mathrm{g}^{-1}$
17	ε_T	real	$(\partial \varepsilon/\partial \ln T)_\rho$/erg $\mathrm{s}^{-1}\,\mathrm{g}^{-1}$
18	ε_ρ	real	$(\partial \varepsilon/\partial \ln \rho)_T$ /erg $\mathrm{s}^{-1}\,\mathrm{g}^{-1}$
19	Ω_{rot}	real	Rotation angular velocity /rad s^{-1}

The frequency spectrum for a model sdB star generated with the STARS code and pulsations analysed by GYRE is shown in Figs. 2.14 and 2.15.

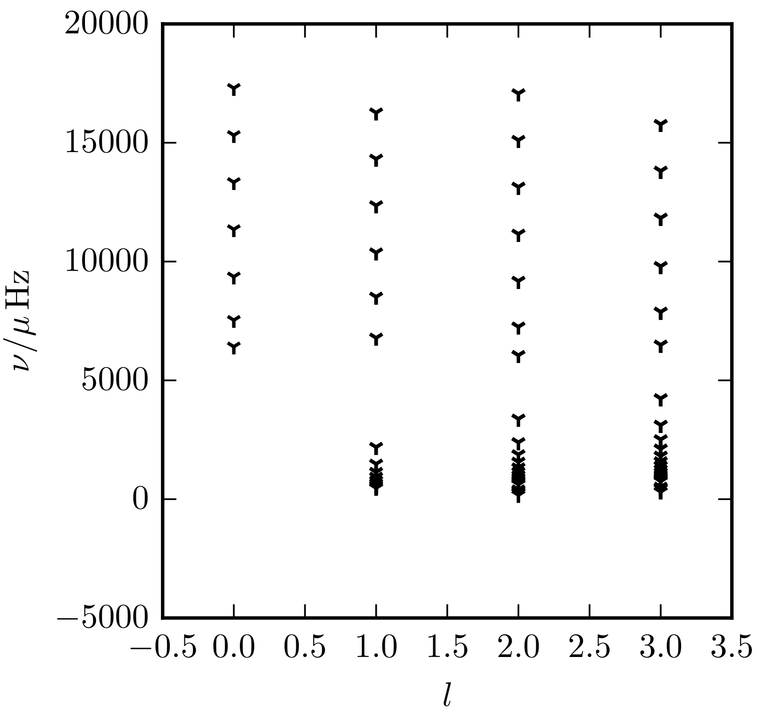

Fig. 2.14 Calculated pulsation frequency spectrum of a sdB star with $M = 0.47\,\mathrm{M}_\odot$ and $M_{\mathrm{env}} = 0.001\,\mathrm{M}_\odot$ as a function of degree l.

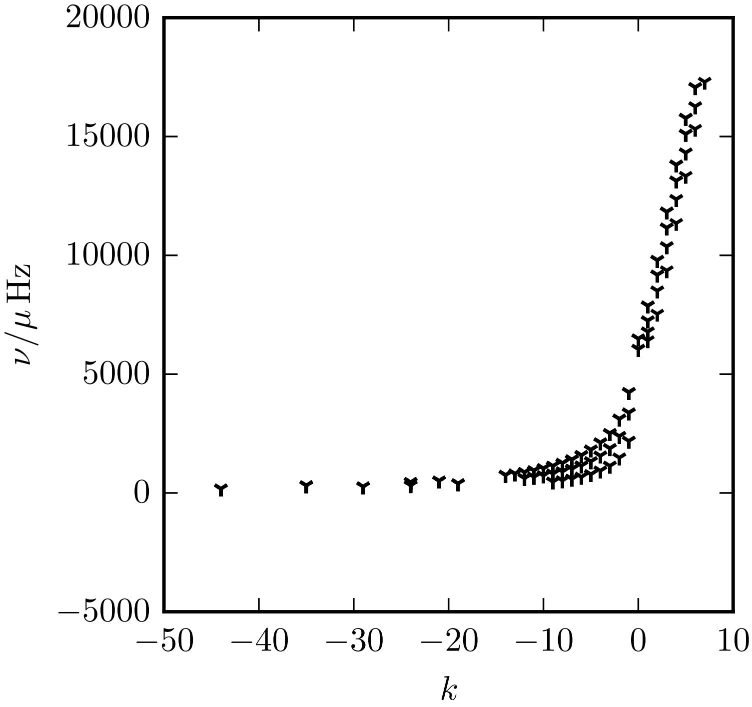

Fig. 2.15 Calculated pulsation frequency spectrum of a sdB star with $M = 0.47\,\mathrm{M}_\odot$ and $M_{\mathrm{env}} = 0.001\,\mathrm{M}_\odot$ as a function of k.

Chapter 3

Tidal Interactions in Post Common-Envelope sdB Binaries

Over half of all observed hot subdwarf B (sdB) stars are found in binaries, and over half of these are found in close configurations with orbital periods of 10 d or less. In order to estimate the companion masses in these predominantly single-lined systems, tidal locking has frequently been assumed for sdB binaries with periods less than half a day. Observed non-synchronicity of a number of close sdB binaries challenges that assumption and hence provides an ideal testbed for tidal theory. We solve the second-order differential equations for detailed 1D stellar models of sdB stars to obtain the tidal dissipation strength and hence to estimate the tidal synchronization time-scale owing to Zahn's dynamical tide. The results indicate synchronization time-scales longer than the sdB lifetime in all observed cases. Further, we examine the roles of convective overshooting and convective dissipation in the core of sdB stars and find no theoretical framework in which tidally-induced synchronization should occur [1].

3.1 Introduction

Hot subdwarf B (sdB) stars are compact sub-luminous stars. They have surface temperatures between 20 000 and 40 000 K and surface gravities $5 < \log_{10}(g_{\mathrm{surf}}/\mathrm{cm\,s^{-2}}) < 6$. The sdBs were first observed by Humason and Zwicky (1947) and their spectra were quantified by Sargent and Searle (1968). The stars are helium core burning with low-mass hydrogen envelopes. Typically the stars spend around 150 Myrs in their He burning phase. They are thought to be the cores of red giant branch (RGB) stars exposed by close binary-star

[1] Chapter 3 is Preece, H. P., Tout, C. A., and Jeffery, C. S. (2018). Tidal Interactions of Close Hot Subdwarf Binaries. MNRAS, 481:715–726.

interaction (Han et al., 2002). One of the proposed mechanisms for sdB formation is common envelope ejection. The sdBs produced in this manner are in binary systems with orbital periods less than 10 d. Observations suggest that about half of the observed sdB systems lie in such configurations (Copperwheat et al., 2011; Napiwotzki et al., 2004).

The close sdB binaries are spectroscopically single-lined with either white dwarf (WD) or low-mass main-sequence dM companions. Eclipsing post-common envelope sdBs with a dM companion are referred to as HW Vir type systems. Unless it is eclipsing it is generally not possible to find the inclination of a system. This means it can be difficult to estimate the component masses. By assuming tidal synchronization, a spectroscopic measurement of the projected rotation velocity and an assumed radius constrains the rotational period, the orbital inclination, and hence the companion mass. Kudritzki and Simon (1978) first applied this method to the subdwarf O star HD49798. Geier et al. (2010) further applied the same technique to a sample of 51 close sdB stars.

The fact that so many sdBs are in close binaries makes them an ideal test bed for tidal dissipation theories. These theories have always been controversial for stars with convective cores and radiative envelopes such as sdBs. Two competing theoretical prescriptions for dissipation in such stars are given by Zahn (1975, 1977) and Tassoul and Tassoul (1992). Giuricin et al. (1984) demonstrated that the dynamical tide proposed by Zahn (1977) is too inefficient to describe the observed level of synchronization of some early main-sequence spectroscopic binaries, particularly when the fractional radius of the convective region is below 0.05. Tassoul and Tassoul (1992) address this efficiency issue by suggesting that pumping across the Ekman boundary provides a mechanism for tidal dissipation. Rieutord and Zahn (1997) dispute the physical validity of Tassoul's mechanism.

In Section 3.2 we review the current observations and previous calculations of tidal synchronization. In Section 3.3 we address the methods used for this paper by discussing the numerical methods and the stellar models. In Section 3.4 we present our results and Section 3.5 concludes.

3.2 Observations and Previous Studies of Tidal Synchronization Time-scales

In a circular orbit, full tidal synchronization has been achieved when the entire star rotates as a solid body with a spin period equal to the binary orbital period. Until recently, only the surface rotation of sdBs could be determined from rotational broadening of spectral lines. The metal lines are used to determine the projected equatorial speed $v_{\rm rot} \sin i$. Pulsations

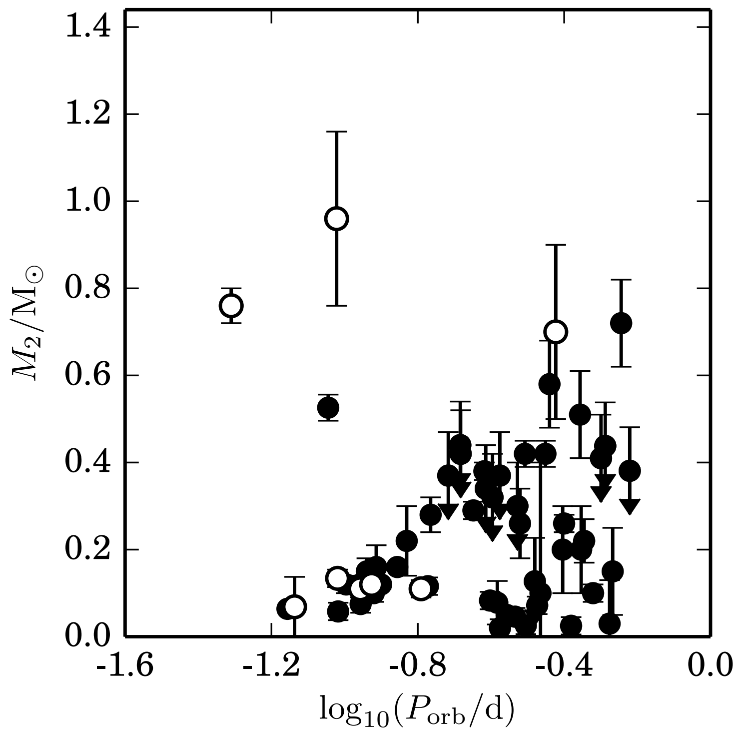

Fig. 3.1 Companion mass, M_2, versus orbital period for all observed sdB binary systems with orbital period less than 0.6 d. The masses of these systems have been estimated from spectroscopic orbits. The white points have assumed tidal synchronization.

of sdBs have been both predicted (Charpinet et al., 1996b) and observed (Kilkenny et al., 1997) making them candidates for asteroseismology. If the stars are rotating, one of the degeneracies of the pulsations is broken. This manifests itself as a small symmetric splitting of the pulsation modes. If this splitting can be resolved the internal rotation rate of the star can be determined. If the rotation period and orbital period are known tidal synchronization can be confirmed or dismissed.

3.2.1 Observational Context

About 65 sdB binaries with orbital periods below 0.6 d have been observed so far. The orbital periods and companion masses of this sample are shown in Fig. 3.1. Of this sample some have assumed tidal synchronization. The observations are summarised by Kupfer et al. (2015a) and in papers cited therein. Several pulsating sdBs have been observed with the *Kepler* mission (Østensen et al., 2010). The observed properties of the sdBs most relevant to this study are summarised in Table 3.1.

Table 3.1 Rotation and orbit properties of sdBs with orbital periods below 0.6 d and known spin periods.

Name	$P_{\rm orb}$/d	$P_{\rm rot}$/d
CD $-30°11223$	0.0489	0.0427 or 0.0646
J162256+473051	0.069789	0.1151563523
NY Vir	0.101016	0.101016
Feige 48	0.34375	?
KIC 11179657	0.394454167	7.4
B4	0.3985	9.63
KIC 02991403	0.443075	10.3

Of all observed sdB binaries, NY Vir is the only object for which the outer layers show evidence of synchronous rotation with the binary orbit from asteroseismology (Charpinet et al., 2008). If the star is in synchronous rotation it is a fast rotator which complicates asteroseismological analysis. Charpinet et al. (2008) obtained an sdB mass of $0.459 \pm 0.006\,M_\odot$ from asteroseismology. Vučković et al. (2007) solved for the binary properties of the system using multi-band photometric lightcurves and radial velocity curves from high-resolution spectra. Owing to the correlation between the large number of free parameters and degeneracies in the mass ratio of the binary, three equally probable solutions were obtained. These three solutions predict sdB masses of 0.530, 0.466 or $0.389\,M_\odot$. The companion mass M_2 is either 0.11 or $0.12\,M_\odot$ and the orbital period of the binary $P_{\rm orb} = 0.101016\,$d. Van Grootel et al. (2013)'s seismic analysis measured an sdB mass of $0.471 \pm 0.006\,M_\odot$.

Feige 48 was initially thought to be synchronized with $P_{\rm rot} = 9.02 \pm 0.07\,$hr (Van Grootel et al., 2008) and $P_{\rm orb} = 9.0 \pm 0.5\,$hr (O'Toole et al., 2004). This $P_{\rm rot}$ was determined from asteroseismology with a 6 night campaign at CFHT. Latour et al. (2014) remeasured $P_{\rm orb} = 8.24662\,$hr which challenges conclusion of tidal synchronization. In addition, Fontaine et al. (2014) carried out an extensive 5-month asteroseismic campaign which challenges the $P_{\rm rot}$ obtained by Van Grootel et al. (2008). The true $P_{\rm rot}$ remains unknown.

Rotational splitting was measured for the three HW Vir type systems B4 (Pablo et al., 2012a), KIC 02991403 and KIC 11179657 (Pablo et al., 2012b). All of these were found to be rotating substantially sub-synchronously. B4 is a sdB binary in the NGC 6791 open cluster. It has $P_{\rm orb} = 0.3985\,$d and $P_{\rm rot} = 9.63\,$d. The companion has been identified as a low-mass main-sequence star but its mass has not been further constrained. KIC 11179657 has $P_{\rm orb} = 9.4669\,$hr, $P_{\rm rot} = 7.4\,$d and $M_2 < 0.26\,M_\odot$. KIC 02991403 has $P_{\rm orb} = 10.6338\,$hr, $P_{\rm rot} = 10.3\,$d and $M_2 < 0.26\,M_\odot$.

The remaining sdB binaries observed with *Kepler* and with asteroseismically inferred rotation rates are PG1142-037 (Reed et al., 2016), KIC 7664467 (Baran et al., 2016), KIC 10553698 (Østensen et al., 2014), KIC 7668647 (Telting et al., 2014). These have $13\,\mathrm{hr} < \mathrm{P_{orb}} < 14\,\mathrm{d}$ and $35\,\mathrm{d} < \mathrm{P_{rot}} < 47\,\mathrm{d}$. Typical rotation rates for sdBs, without considering the effects of common envelope evolution, have been approximated with measurements from red clump stars, which are considered to have a similar evolutionary origin (Mosser et al., 2012). If we take initial spin periods from those of the red clump stars as lying between 30 and 300 d, the binaries in wider orbits aren't spun up while those in systems with $P_{\mathrm{rot}} \ll 30\,\mathrm{d}$ are somewhat spun up but predominantly not synchronized.

Further insight is provided by J162256+473051, the shortest period HW Vir system known, with $P_{\mathrm{orb}} = 0.069789\,\mathrm{d}$ (Schaffenroth et al., 2014). The system is eclipsing, so the inclination is known and the surface rotation rate can be directly measured from the line profiles. Combined with the measured radius, $P_{\mathrm{rot}} = 0.1151563523\,\mathrm{d}$ and so J162256+473051 is rotating non-synchronously. The mass of the sdB star was found to be between 0.28 and $0.64\,\mathrm{M_{\odot}}$, with $M_{\mathrm{sdB}} = 0.48 \pm 0.03\,\mathrm{M_{\odot}}$ giving the best results (Schaffenroth et al., 2014). With the orbit fully solved, the mass of the unseen companion is found to be $0.064\,\mathrm{M_{\odot}}$, well below the H-burning threshold. This is therefore evidence that sub-stellar companions can provide enough energy to remove the H-envelope during common envelope evolution but not enough torque to synchronize the sdB star.

To date, the shortest period sdB binary is CD $-30°$11223 with $P_{\mathrm{orb}} = 0.0489\,\mathrm{d}$. This system is eclipsing and displays clear signs of ellipsoidal variations. Spectroscopically, the projected surface rotation $v_{\mathrm{rot}} \sin i = 177 \pm 10\,\mathrm{km\,s^{-1}}$ and the inclination $i = 83.8° \pm 0.6$ (Vennes et al., 2012). The logarithmic surface gravity $\log(g_{\mathrm{surf}}/\mathrm{cm\,s^{-2}})$ of this sdB has been measured as 5.72 from high dispersion spectra and 5.36 from low dispersion spectra (Vennes et al., 2011). The higher solution gravity is consistent with the system being synchronized but the lower is not. If the canonical mass of $0.47\,\mathrm{M_{\odot}}$ is assumed for the sdB star, the companion mass $M_2 = 0.74\,\mathrm{M_{\odot}}$. A sdB mass of $0.54\,\mathrm{M_{\odot}}$ and companion mass of $M_2 = 0.79\,\mathrm{M_{\odot}}$ also provide a consistent solution. Because CD $-30°$11223 is an extreme system with both a short orbital period and a high companion mass, it is the sdB binary most likely to have been synchronized.

In many cases the detection of ellipsoidal variations with a period of half the orbital period have been used as confirmation of tidal synchronization. By definition, the tidal bulge forms in response to the presence of a companion and so should point towards it. Whilst the bulge may slightly lag or lead the orbit the angle of the lag is assumed constant over an orbit. In the case of Koen et al. (1998) ellipsoidal variations are detected but synchronization is assumed on the basis that the orbital period is short.

3.2.2 Previous Calculations

Geier et al. (2010) investigated whether the assumption of tidal synchronization could be used to determine the inclination and thus yield the companion mass for close spectroscopically single lined sdB binaries. They analysed a sample of 51 observed sdB stars in binaries with periods below 10 d. They calculated synchronization time-scales with the theoretical prescriptions described by Zahn (1977) and Tassoul and Tassoul (1992). Fig. 3.2 applies the calculations of synchronization due to Zahn's dynamical tide to the set of known sdBs with orbital periods less than 0.6 d assuming an EHB lifetime of 150 Myr.

The Tassouls' mechanism for dissipation predicts that all systems with $P_{\mathrm{orb}} < 10\,\mathrm{d}$ are synchronized which is not observed. Zahn's theory of dynamical tides describes tidal dissipation for stars with convective cores and radiative envelopes. The synchronization time-scales depend on the tidal coupling coefficient E_2 which is highly dependent on the structure of the star. The coefficient is laborious to calculate so Geier et al. (2010) used a scaling from main-sequence models and E_2 was approximated as $(r_{\mathrm{conv}}/R_{\mathrm{sdB}})^8$ (Claret and Cunha, 1997), where r_{conv} is the radius of the convective core and R_{sdB} is the total radius of the sdB star. Note that r_{conv} includes any semi-convective region. The sdB model used had $r_{\mathrm{conv}}/R_{\mathrm{sdB}} = 0.15$ and a canonical mass of $0.47\,\mathrm{M}_\odot$. The radii of the sdBs are calculated from observed spectroscopic g_{surf}. Zahn's dynamical tide doesn't consider dissipation via turbulent convection, this must be calculated separately.

Geier et al. (2010)'s calculations of Zahn's dynamical tide predicted that systems with orbital periods less than 0.39 d would synchronize within the EHB lifetime. The study found that the systems with orbital periods up to 1.2 d could be solved consistently under the assumption of tidal synchronization. However, using this approach they found a dearth of systems at high inclinations and also predicted some very large companion masses. The assumption of tidal locking is further contradicted by Schaffenroth et al. (2014) and the three Pablo observations. Follow up observations of some of the Geier et al. (2010) systems has shown that the observed companion masses are lower than those predicted.

In light of the asteroseismological results for sub-synchronously rotating sdB systems with orbital periods substantially below 1.2 d, Pablo (2012) recalculated the time-scales predicted by Zahn's dynamical tide. This approach was to solve the two required structural differential equations to get a precise E_2. He did this for one detailed stellar model with a mass of $0.478\,\mathrm{M}_\odot$, radius $0.298\,\mathrm{R}_\odot$ and $r_{\mathrm{conv}}/R_{\mathrm{sdB}} = 0.08$ and an undisclosed radius of gyration. These calculations found E_2 to be significantly smaller than $(r_{\mathrm{conv}}/R_{\mathrm{sdB}})^8$. Ultimately he predicted that systems with $P_{\mathrm{orb}} < 3.6\,\mathrm{hr}$ should be synchronized within a typical sdB lifetime of 150 Myr. Pablo's study looked at only one sdB model which has a

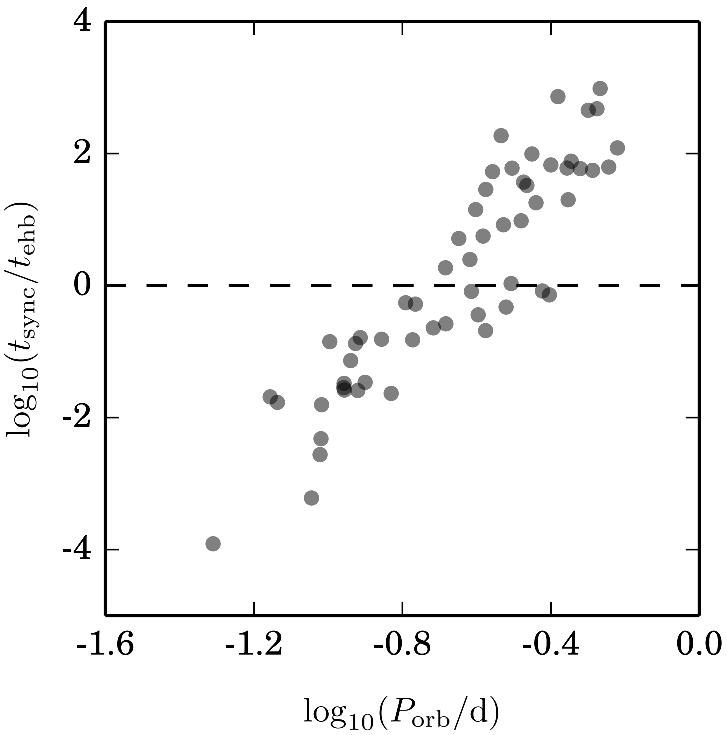

Fig. 3.2 The ratio of synchronization time-scale to the extreme horizontal branch lifetime as a function of the orbital period for the known close sdB binaries with orbital periods less than 0.6 d as calculated by Geier et al. (2010) using Zahn's mechanism. Geier's calculations of Zahn's dynamical tide suggest that sdB stars synchronize with orbital periods less than 0.39 d.

fairly large radius compared to most sdBs and only considered dissipation owing to excited, and subsequently damped, g-modes.

3.3 Methods

Calculation of the tidal effects for all dissipation mechanisms considered in this paper requires solving structural differential equations for detailed stellar models. A grid of stellar models was created for this purpose and differential equation solvers were written and included in the tidal dissipation calculation code.

3.3.1 Differential Equation Solvers

Both dissipation prescriptions require solutions to second-order differential equations for detailed 1D stellar models. Both differential equations are initial value problems that can be solved with integrator methods. We constructed an Euler solver, second order Runge-Kutta solver and a fourth order Runge-Kutta solver based on the algorithms presented by Conte and Boor (1980). These methods all allow for variable step sizes so errors introduced by interpolation can be avoided. The Euler solution is the fastest computationally but also the least accurate. However all the methods predicted the same time-scales to within 0.5 per cent.

3.3.2 Stellar Models

All the stellar models used were created with the Cambridge STARS code (Eggleton, 1971). STARS has been modified substantially since its inception (Stancliffe and Eldridge, 2009). It uses OPAL II type opacity tables, allows for binary evolution and follows the chemical evolution of ^{1}H, ^{3}He, ^{4}He, ^{12}C, ^{14}N, ^{16}O and ^{20}Ne. The code uses an adaptive non-Lagrangian mesh. Convection is treated with mixing-length theory (MLT) as described by Böhm-Vitense (1958) and uses a MLT parameter of $\alpha = 2.0$ (defined as the ratio of mixing length to pressure scale-height). Semi-convection is treated as a diffusive process (Eggleton, 1972). Convective overshooting as described by Schröder et al. (1997) is also included. Mass loss on the red giant branch (RGB) is described by Reimers' prescription (Reimers, 1977). The sdB star models were made with the method described by Hu et al. (2008, 2010) as follows.

The He Flash

The STARS code cannot evolve stars through the He-flash independently. To imitate this process, a star with just enough mass to ignite He quietly and non-degenerately is created

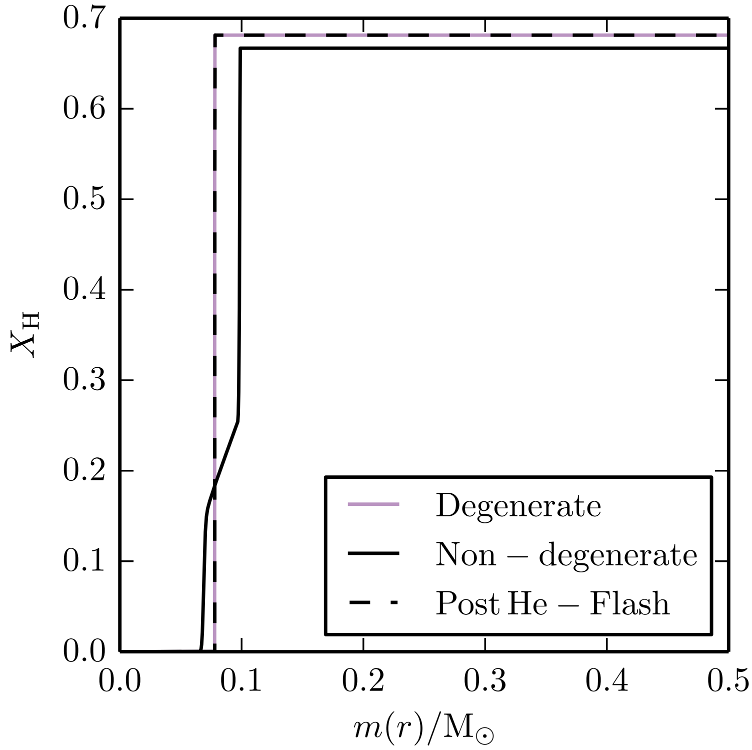

Fig. 3.3 The H composition profile through the post He-flash model. The purple line is the profile of the degenerate star just before He ignition. The black line is the profile of the He burning non-degenerate star before modifying the core or envelope. The purple points show the adjusted $1.75\,\mathrm{M}_{\odot}$ post He-flash model. The adjusted profile maintains the steep composition gradient formed during the red giant branch phase.

(Pols et al., 1998). This is allowed to evolve until just after He is ignited. Next, mass is removed from the star to give it the desired mass. The composition profile through the star is modified and the core is allowed to grow a little to give the same envelope profile and core mass as its degenerate counterpart. The H composition profile for the $1.75\,\mathrm{M}_{\odot}$ post He-flash star is displayed in Fig. 3.3. Piersanti et al. (2004) and Castellani and Castellani (1993) show that this treatment isn't fully correct as some extra carbon is produced during the He flash however the models suffice for this body of work.

The sdB Stars

The sdBs were made from three different mass progenitors, 1.25, 1.5 and $1.75\,\mathrm{M}_{\odot}$. These stars had respective core masses of 0.4680, 0.4614 and $0.4510\,\mathrm{M}_{\odot}$ at the tip of the RGB. Common envelope ejection was simulated with high mass-loss rates. During the common-envelope simulation the nuclear reactions were turned off and the star was kept in thermal equilibrium. The mass loss was stopped with envelope masses distributed between 0, where the hydrogen mass fraction reached 0.1, and $0.02\,M_\odot$ giving a range of resultant sdB masses distributed near the canonical mass of $0.47\,M_\odot$. Each sdB model was then allowed to relax on to the zero-age extreme horizontal branch (ZAEHB) and then to evolve through He burning. As discussed by Schindler et al. (2015), overshooting affects the mass of the sdB's convective region during its evolution. Models with no overshooting and an overshooting parameter of $\delta_{\rm ov} = 0.12$ (Schröder et al., 1997) were created. This results in a grid of over 800 stellar models with a range of envelope masses and evolutionary states. Fig. 3.4 shows the sdB models on a $T_{\rm eff} - \log g$ diagram with the observed close sdBs from Fig. 3.1. The radial growth of the convective core for a single sdB evolutionary sequence can be seen in Fig. 3.5 for an sdB model with $M_{\rm sdB} = 0.47\,M_\odot$ and envelope mass $10^{-4}\,M_\odot$ and no convective overshoot.

Boosting the overshooting parameter did not result in as much core growth as achieved by Schindler et al. (2015). Unlike the STARS code MESA defines semiconvective regions as those which are unstable to convection according to the Schwarzschild criterion but stable according to the Ledoux criterion (Paxton et al., 2011, 2013). The MESA overshooting region is defined as $l_{\rm ov} H_P$ where $l_{\rm ov}$ is user defined and H_P is the pressure scale height. Because $H_P \to \infty$ as $r \to 0$ the overshooting length can become very large for stars with small convective cores.

3.4 Results

We calculated synchronization time-scales for all of the modelled sdBs with companion masses below the Chandrasekhar mass limit and orbital periods less than 4 hr for dissipation by Zahn's prescription. Our results suggest that the sdBs cannot become tidally synchronized within the extreme horizontal branch (EHB) lifetime. Traditionally the dynamical tide assumes no dissipation via the equilibrium tide. In the case of sdBs this assumption may not be valid. The sdBs have had the majority of their envelope removed meaning that the convective core now occupies a much more substantial fraction of the star. The synchronization time and change in the rotational period due to the equilibrium tide is also calculated.

3.4.1 Zahn's Dynamical Tide

Previous studies of tidal synchronization for sdB stars have focused on Zahn's prescription of tidal dissipation which applies to stars with convective cores and radiative envelopes as

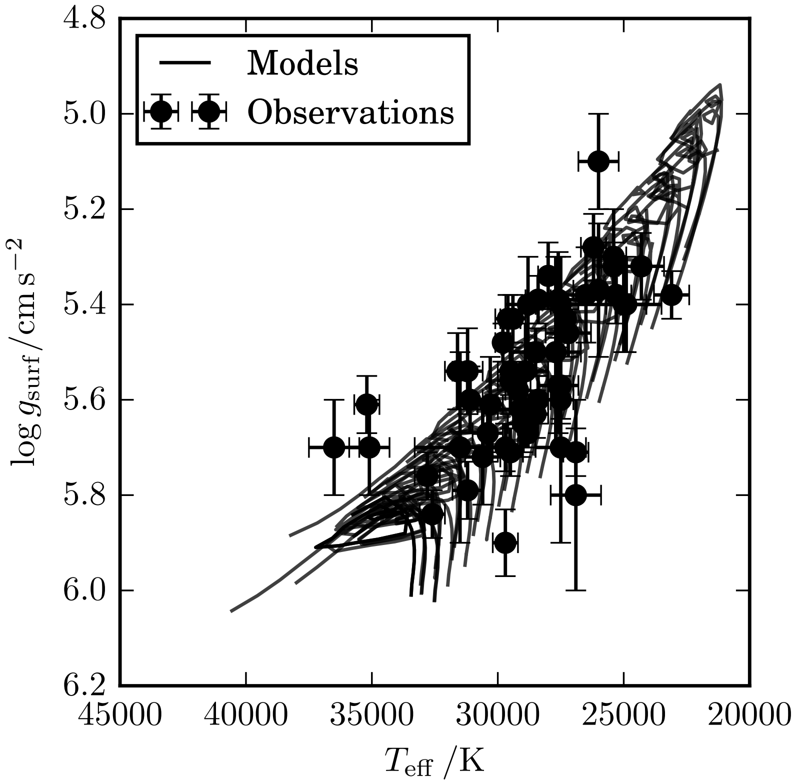

Fig. 3.4 The logarithm of the surface gravity as a function of effective temperature $T_{\rm eff}$. The tracks are the sdB models. The observed quantities for the known close sdB binaries shown in Fig. 1 are plotted in black with error bars. The sdBs with the largest envelope masses have the lowest effective temperatures and surface gravities.

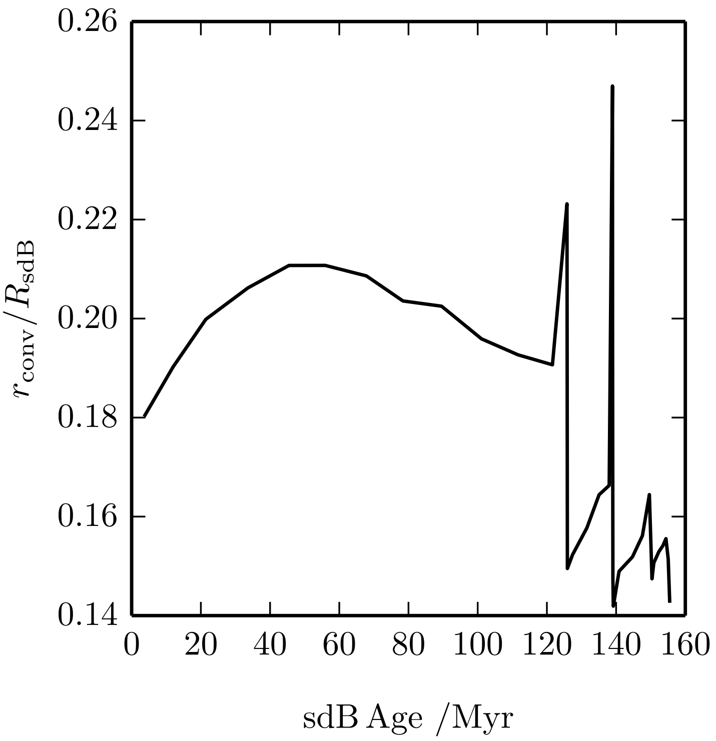

Fig. 3.5 The evolution of the fractional radial extent of the convective core over the sdB evolution for a single evolutionary sequence against time t measured from the start of the sdB phase. Towards the end of the sdB evolution core breathing pulses can be seen. The model is a $0.47\,\mathrm{M}_\odot$ sdB star with a $10^{-4}\,\mathrm{M}_\odot$ envelope.

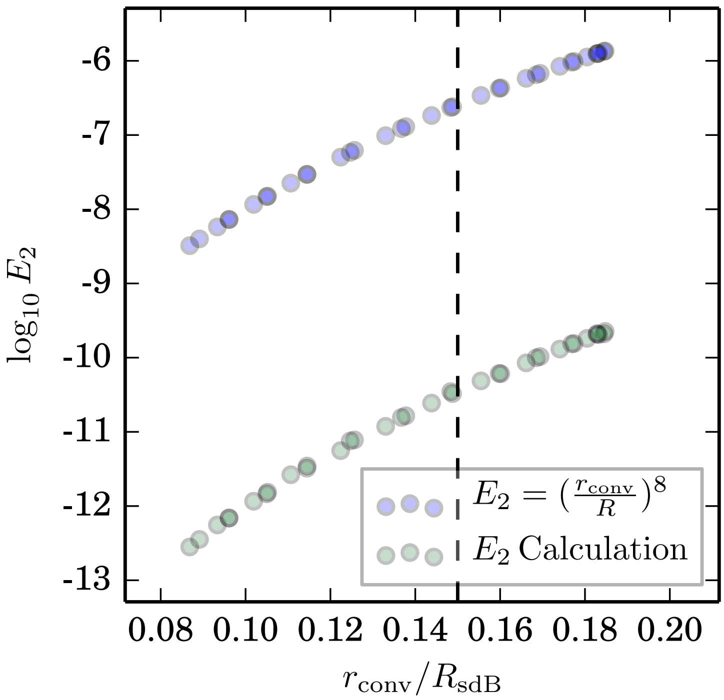

Fig. 3.6 E_2 as a function of the ratio of the radial extent of the convective zone of the ZAEHB sdB models. The blue circles are E_2 calculated as $(r_{\mathrm{conv}}/R_{\mathrm{sdB}})^8$ and the green circles are E_2 calculated by solving the required second order differential equations. The blue line is that used for Geier (2010)'s study. The two different methods for calculating E_2 give results that differ by an average of 4 orders of magnitude and show that scaling from main-sequence models doesn't work.

discussed in section 1.4.2. The grid of models discussed in section 3.3.2 was used to solve Eqs. 1.81 and 1.84 and then to find the tidal coefficient E_2. The results of these calculations are shown in Fig. 3.6. This re-calculation of E_2 shows that the main-sequence scaling treatment is a poor approximation. The parametrization over-predicts E_2 by at least a factor of 3000. In addition, E_2 is highly sensitive to the relative size of the convective region and spreads over two orders of magnitude.

Geier et al. (2010) assumed $r_{\mathrm{conv}}/R_{\mathrm{sdB}} = 0.15$. The ZAEHB sdB model with $r_{\mathrm{conv}}/R_{\mathrm{sdB}} = 0.15$ has $E_2 = 10^{-10.6}$. The results of applying this to the synchronization calculations can be seen in Fig. 3.7. None of the systems reach synchronization within the sdB lifetime and so the dynamical tide cannot explain any observed tidal synchronization. This approach assumes that all sdB stars have the same E_2, which has been demonstrated to be incorrect and will be addressed further in Sec. 3.4.3.

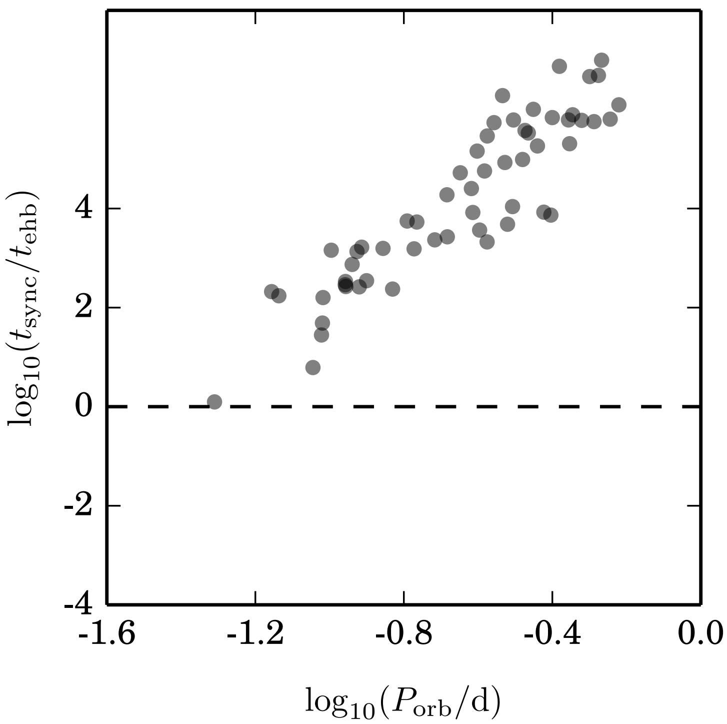

Fig. 3.7 As Fig. 2 with $t_{\rm sync}$ computed via Zahn's mechanism with $E_2 = 10^{-10.6}$.

3.4.2 Basic Convective Dissipation

We consider convective dissipation as discussed in section 1.4.1 in the model of a zero-age extended horizontal-branch (ZAEHB) star with $M_{\text{sdb}} = 0.47\,\text{M}_{\odot}$ and $M_{\text{env}} = 10^{-4}\,\text{M}_{\odot}$. As a preliminary investigation into the significance of convective dissipation, the P_{orb} and M_2 parameter space for tidal synchronization within the EHB lifetime for a single sdB model has been computed and is shown in Fig. 3.8. This plot shows the results for convective dissipation assuming an initial rotation period of 100 d based on observations of rotation rates of red clump stars (Mosser et al., 2012). As can be seen, synchronization is not achieved within the EHB lifetime by this mechanism except for the shortest period systems with relatively high-mass white dwarf companions. These systems rapidly reach a state of tidal synchronization. The model was selected because it has the canonical mass of $0.47\,\text{M}_{\odot}$ and one of the lower-mass envelopes of the grid. Owing to its influence on the overall stellar radius, the envelope mass is the main factor governing the fractional radial extent of the convective region. A model with a low envelope mass synchronizes more quickly than one with a higher envelope mass. Closer examination of the mixing length and velocity of this model shows that the convective turnover time is substantially longer than the orbital period. This results in the tidal forces being significantly less effective because convective elements do not travel over the full mixing length during one orbital revolution (Goldreich and Nicholson, 1977). The implications of fast tides are discussed the next section.

3.4.3 Synchronization Time-scales

Convective dissipation approximates the convective viscosity as $\nu = wl$ where w is the local velocity of MLT convective cells and l is the size of these cells. The convective turnover time was found to be orders of magnitude longer than the orbital periods at which tides are most effective. This means the dissipation is substantially less efficient. A corrective factor is introduced to the equation for finding the viscosity of the convective region such that

$$\nu = wl\Psi(r), \tag{3.1}$$

and Eq. 1.68 is updated to

$$\frac{1}{\tau_{\text{visc}}} = \frac{1}{M_1 R_1^2} \int_0^{M_1} wl\gamma(r)\Psi(r)dm. \tag{3.2}$$

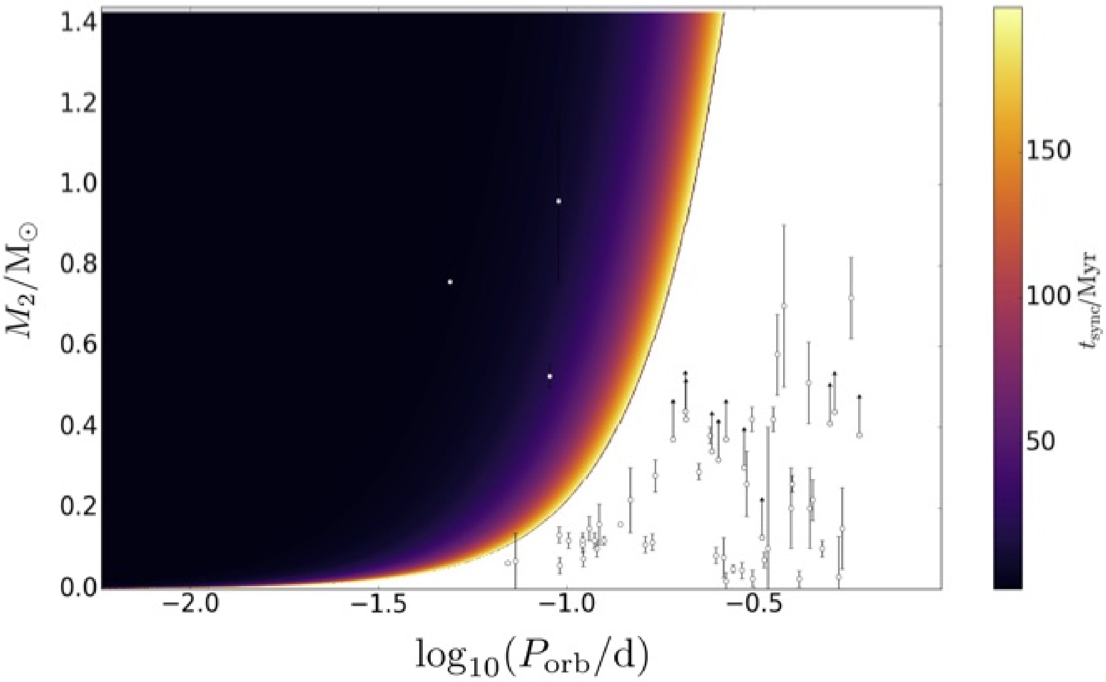

Fig. 3.8 Plot of synchronization time-scales by convective dissipation for a single ZAEHB sdB model with $M_{\rm sdb} = 0.47\,\mathrm{M}_\odot$, $M_{\rm env} = 10^{-4}\,\mathrm{M}_\odot$. Companion masses less than the Chandrasekhar mass limit and orbital periods less than 0.5 d were calculated. Observed stars are open points with error bars. The synchronization time is shown in the colour bar. Only the closest sdBs with intermediate-mass white dwarf companions are expected to synchronize within the sdB lifetime.

Zahn (1966, 2008) introduced

$$\Psi_1(r) = \left|\frac{P_{\rm orb}}{2t_{\rm turnover}}\right|^1, \tag{3.3}$$

which corrects for the distance that the convective material moves in half an orbital period. Goldreich and Nicholson (1977); Hurley et al. (2002) define the corrective factor $\Psi(r)$ as

$$\Psi_2(r) = \left|\frac{P_{\rm orb}}{2t_{\rm turnover}}\right|^2. \tag{3.4}$$

as even though the largest convective eddies move a distance described by Ψ_1 they do not exchange momentum with the mean flow on this time-scale. Assuming that the Kolmogorov spectrum applies to convective turbulence they arrived at Ψ_2. Goodman and Oh (1997); Penev et al. (2007) carried out 3D hydrodynamical simulations to investigate the effect of fast tides and obtained results more in agreement with $\Psi_2(r)$. They suggest that these results are most applicable to tidal dissipation in gaseous planets owing to uncertainties in stellar convection feedback. We compare the two cases here.

The mixing length in the core of the star tends to infinity when defined as $l = \alpha P/\rho g$ where α is the mixing length parameter, P is the pressure, ρ is the density and g is the gravity. It is unphysical for l to exceed the radius of the convective region so several different approximations were used to study the effect on the tidal synchronization times. The four mixing lengths examined are as follows:

1. MLT1 is l as predicted by traditional mixing length theory
2. MLT2 is l restricted to the distance to the edge of the convective region. This is the most necessary constraint.
3. MLT3 has l limited so that the convective turnover time is just less than the orbital period and so the tides are not fast. Typically $l = r_{\rm conv}/20$ satisfies this.
4. MLT4 has $l = r_{\rm conv}/50$.

CD $-30^\circ 11223$

The effects of initial rotation rate and different corrective factors are considered for the full set of ZAEHB models and applied to the CD $-30^\circ 11223$ system in Fig. 3.9. Properties of CD $-30^\circ 11223$ can be found in Table 3.1. The majority of models predict synchronization time-scales longer than the typical EHB lifetime. In the most efficient cases, with a modified MLT, synchronization via convective dissipation, is predicted within the EHB lifetime for some models. Even the models which predict synchronization within the EHB lifetime do so on times comparable to this evolutionary stage meaning assumptions of tidal synchronization should be made with extreme care. An initial rotation rate of 1 d only has a very small effect on the synchronization time-scales.

The equilibrium tidal dissipation time-scales are generally longer than dynamical tide dissipations unless MLT3 or MLT4 are used as can be seen in Fig. 3.9. Calculation by Geier et al. (2010)'s method predicts synchronization well within the EHB lifetime of 150 Myr. However detailed calculation of E_2 does not predict this system to be synchronized. The results are slightly different to those predicted in section 3.4.1 because E_2 is calculated individually for each model.

Without taking the effects of fast tides on the tidal dissipation into consideration, shorter mixing lengths predict longer synchronization times because the viscosity in the convective region is smaller. However, the fastest synchronization predictions are for MLT3 because the convective turnover time for this scheme is just below the threshold for the tides to be fast. If the mixing length is longer than this the tides are fast and if the mixing length is shorter the viscosity decreases. When $\Psi_1(r)$ is used the dependence on the mixing length is decreased for MLT1 and MLT2. MLT3 and MLT4 have convective turnover times shorter than the orbital period and so are not affected by fast tides. MLT4 predicts slightly longer synchronization times than MLT3 because it has a lower viscosity.

The synchronization time as a function of sdB age for a $0.47\,\mathrm{M}_\odot$ sdB star with a $10^{-4}\,\mathrm{M}_\odot$ envelope can be seen in Fig. 3.10. The ZAEHB models predict the shortest synchronization time-scales. For these calculations a corrective factor of $\Psi(r)_1$ and an initial rotation rate of 1 d were used.

3.4.4 Change in Rotational Period Over sdB Lifetime

At this stage, it is apparent that sdB stars do not synchronize in the EHB lifetime. Despite this, the tides may still cause the stars to be spun up to some degree. The change in the angular velocity $\Omega(t)$ of the sdB star as it evolves can be calculated by integrating Eq. 1.70 where k_r, R and τ_{tide} are all functions of time.

These calculations were applied to the systems CD $-30°$ 11223, J162256+473051 and NY Vir to find the rotational period at the TAEHB. J162256+473051 is the shortest period sdB binary not observed to be tidally synchronized. It has $P_{\mathrm{orb}} = 0.069\,\mathrm{d}$ and sub-stellar companion mass $M_2 = 0.064\,\mathrm{M}_\odot$. Neither convective dissipation nor radiative dissipation predict the synchronization of this system. NY Vir is the only sdB with asteroseimsological evidence suggesting that it is rotating synchronously. The rotational period at the TAEHB

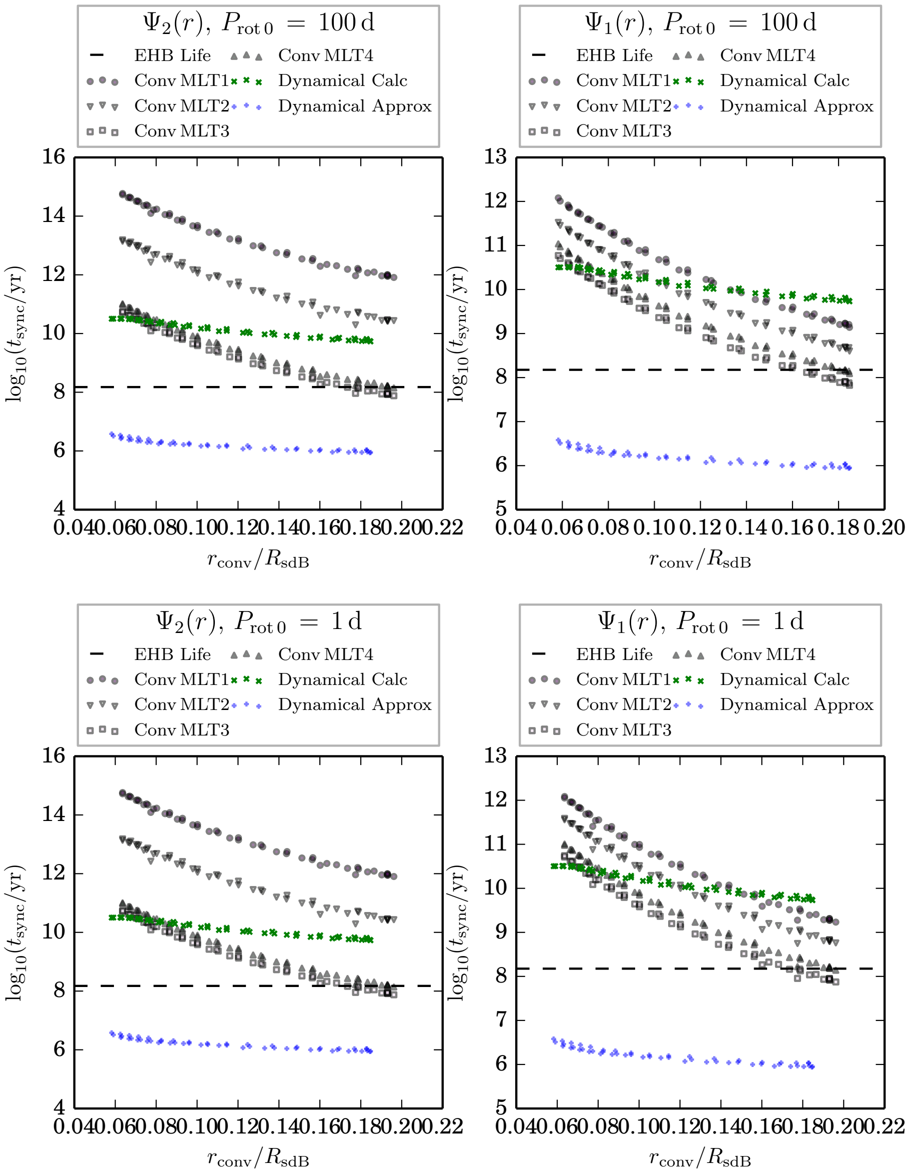

Fig. 3.9 The synchronization time for CD $-30°11223$ as a function of the fractional size of the convective region for the ZAEHB models. The different mixing length (MLT) prescriptions are defined in Sec. 3.4.3. The initial rotation period ($P_{\mathrm{rot}\,0}$) and choice of corrective factor ($\Psi_1(r)$ or $\Psi_2(r)$) are shown in the legend for each panel. MLT3 predicts the shortest time-scales whilst MLT1 predicts the longest. Dynamical calc refers to Zahn's calculations with E_2 calculated as discussed in the text. Dynamical approx refers to Zahn's calculations with $E_2 = (r_{\mathrm{conv}}/R_{\mathrm{sdB}})^8$.

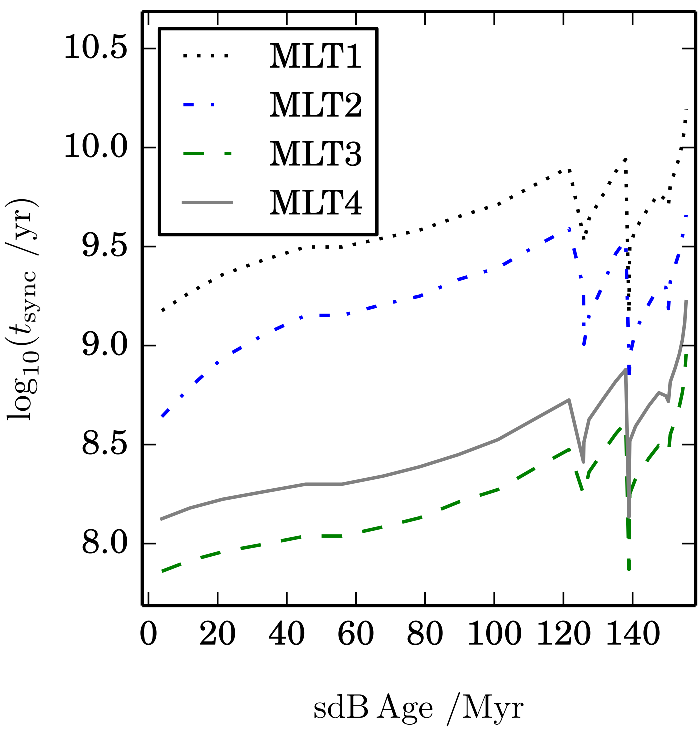

Fig. 3.10 The synchronization time as a function of sdB age for a $0.47\,\mathrm{M}_\odot$ sdB star with a $10^{-4}\,\mathrm{M}_\odot$ envelope. An initial rotation period of 1 d and a corrective factor $\Psi(r)_1$ were used. Even though the fractional convective radius increases, the total radius and the mass of the convective region also increase. The combination of these effects somewhat counter intuitively increases the synchronization time as the star evolves.

was calculated using $\Psi_1(r)$ and $\Psi_2(r)$ and multiple mixing length schemes and can be seen in Fig. 3.11.

In contradiction to the observations, J162256+473051 is predicted to be spun up more than NY Vir by the time it reaches the TAEHB. This is due to the fact that the orbital period of J162256+473051 is substantially shorter than that of NY Vir. Using (Böhm-Vitense, 1958)'s mixing length theory or restricting the mixing length to the distance to the edge of the convective zone, we find the stars not to be spun up at all. If the mixing length is limited so that the convective turnover time is shorter than the tides and the tidal forces are no longer dissipated, all three systems considered are spun up to some degree. If $\Psi_1(r)$ is used the mixing length dependence becomes less strong. MLT3 and MLT4 are independent of $\Psi(r)$ because they have sufficiently short convective turnover times.

3.4.5 Convective Cores and Associated Uncertainties

The models presented above use standard convection theories widely implemented in stellar evolution codes. However, the extent of the convective core measured in some asteroseismic studies, $\log(1-m_{\rm conv}/M_{\rm sdB}) = -0.30$ (Charpinet et al., 2011; Van Grootel et al., 2010b), is somewhat larger than that seen in our models. Additional evidence from white dwarf asteroseismology (Giammichele et al., 2018) suggests even more of the core of the post horizontal-branch star has been homogenized, presumably by additional convective processes. Evidence suggests that red clump stars also have larger convective regions than predicted by standard stellar models (Constantino et al., 2015). A newly adopted maximal overshooting scheme must be used to reproduce the period spacings of the g-dominated mixed modes observed in these stars. However the physical validity of such a scheme is still in question.

Recent theoretical investigations show that extreme care must be taken when determining edges of convective regions in stellar evolution codes (Gabriel et al., 2014; Paxton et al., 2018). Both studies find that the exact method used to find the convective boundary has consequences for the subsequent evolution of a model.

In summary, the physics of helium burning cores is still not well established. In the context of tidal interactions, a larger convective core mass implies a larger fractional convective core radius and hence a shorter tidal synchronization time. However, in the absence of a self-consistent framework in which to compute extreme-horizontal branch models with larger convective cores, it is not possible to compute the effect directly. A parametric investigation would make a worthwhile study.

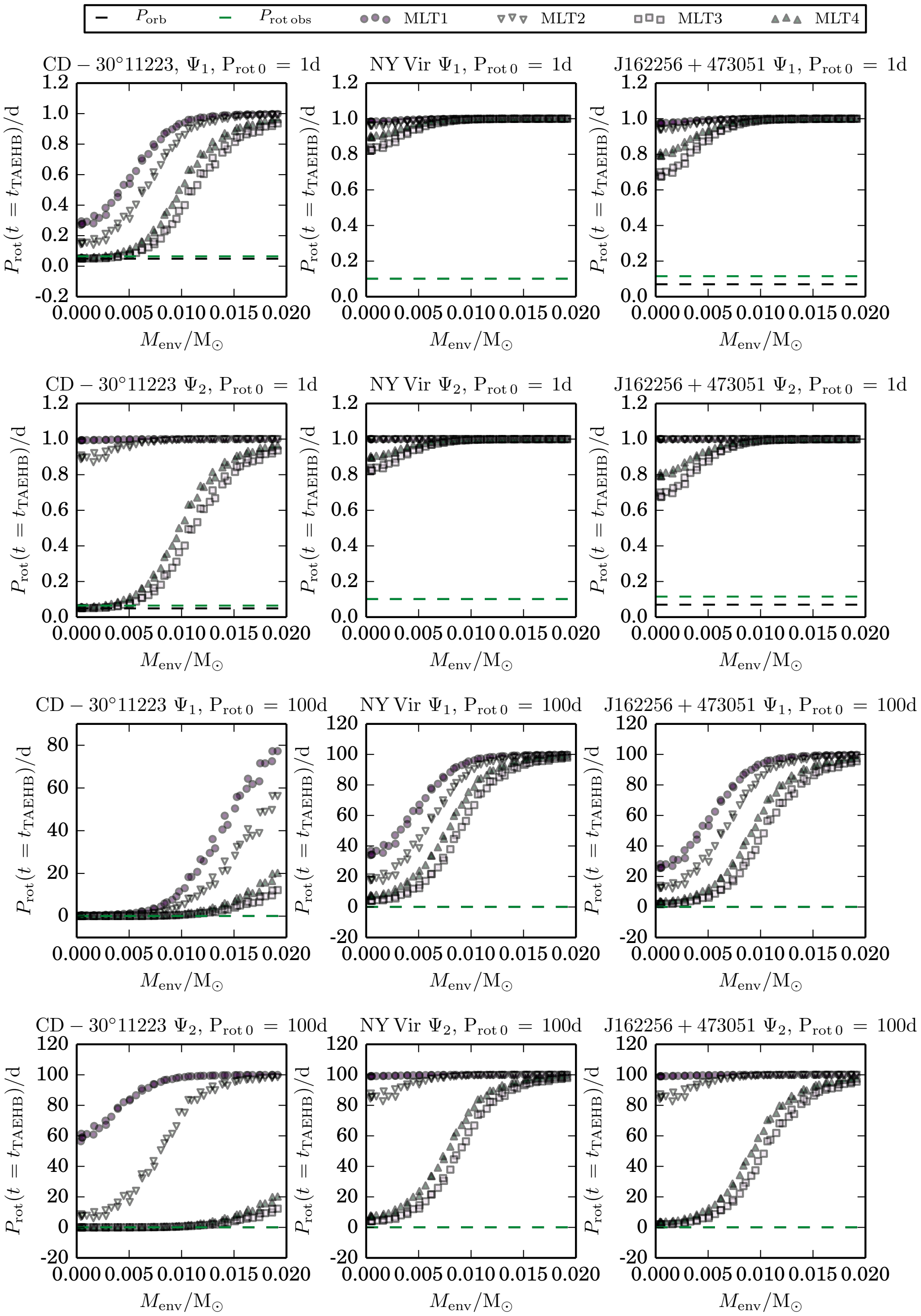

Fig. 3.11 The rotational period of the sdB evolutionary sequences at the TAEHB is shown as a function of the envelope mass of the model. The MLT and viscosity corrective factors are described in Sec. 3.4.3. Whilst the envelope mass does not directly influence the radius of the convection zone it is the main factor governing the stellar radius $R_{\rm sdB}$. Tidal interactions are strongly dependent on $r_{\rm conv}/R_{\rm sdB}$. The data points shown here are for evolutionary sequences with an $r_{\rm conv}/R_{\rm sdB}$ which varies.

3.5 Conclusions

The goal of this study was to find synchronization time-scales for short period sdB binary systems. A grid of sdB models was created with the STARS code for a variety of progenitor masses, envelope masses and treatments of convection. Previous studies have predominantly used Zahn's theory of dynamical tides with a scaling from main-sequence models to find the synchronization times. Recalculating the tidal coefficient E_2 for the grid of sdBs shows scaling from main-sequence models overpredicts E_2 by a factor of at least 3000. The synchronization time-scales should be several orders of magnitude longer. As a result, estimates of Zahn's dynamical tide synchronization time-scales are longer than EHB lifetimes, even for the extreme case of CD $-30°11223$.

The sdB stars have convective cores which provide a mechanism for tidal dissipation. By solving Clairaut's equation the tidal synchronization times owing to turbulent convection have been calculated. Initial calculations of the convective tides predicted that the three sdB systems with the most massive WD companions should be synchronized. Closer examination revealed that the orbital period is typically shorter than the convective turnover time. This causes the convective dissipation of the tides to become substantially less efficient. The corrective factor depends on the turnover time for convective elements within the star and is calculated with mixing length theory. The corrective factor causes estimates of synchronization time-scales to increase by several orders of magnitude so that no sdB binary systems are conclusively predicted to be synchronized.

Böhm-Vitense (1958)'s mixing length theory predicts a singularity at the stellar centre. The effects on tidal synchronization time-scales when the mixing length was altered to remove this singularity were examined. Reducing the mixing length to avoid the central singularity generally increases the synchronization time because the estimated viscosity decreases. The optimal case for tidal dissipation is to reduce the mixing such that the convective turnover time is slightly shorter than the orbital period so that the tidal dissipation is not affected by fast tides. Even in this case synchronization is not achieved because the viscosity is substantially reduced and the tidal interactions are less efficient.

The rotational periods of sdB stars at the TAEHB were calculated to investigate the impact of the tides. The models with the optimally chosen mixing length and with envelope masses less than $0.01\,\mathrm{M}_{\odot}$ are most substantially affected by the tides. The convective region accounts for a larger fractional volume in the sdBs with the lowest mass envelopes so tides are more effectively dissipated.

With the theoretical framework presented, tidal synchronization times for EHB stars are long, but not excessively so, compared with nuclear lifetimes. With evidence from asteroseismology that convective core sizes may be larger than those predicted by classical convection theory, and with the possibility that the tides could induce differential rotation with the EHB star, these avenues of exploration still open.

Chapter 4

Convection physics and tidal synchronization of the subdwarf binary NY Virginis

Asteroseismological analysis of NY Vir suggests that at least the outer 55 per cent of the star (in radius) rotates as a solid body and is tidally synchronized to the orbit. Detailed calculation of tidal dissipation rates in NY Vir fails to account for this synchronization. Recent observations of He core burning stars suggest that the extent of the convective core may be substantially larger than that predicted with theoretical models. We conduct a parametric investigation of sdB models generated with the Cambridge STARS code to artificially extend the radial extent of the convective core. These models with extended cores still fail to account for the synchronization. Tidal synchronization may be achievable with a non-MLT treatment of convection [1].

4.1 Introduction

Hot subdwarf B (sdB) stars are core-helium burning stars which have had their hydrogen-rich envelopes stripped, most likely in a binary interaction. The stars are typically slow rotators. However, those in close binaries are somewhat spun up. The sdB stars in close binaries, with orbital periods less than 10 d, have either low-mass main-sequence or white dwarf companions. The companions are unseen so it is not possible to measure the inclination of the observed systems unless they are eclipsing. If the system is tidally locked then the spin

[1] Chapter 4 is Preece, H. P., Tout, C. A., and Jeffery, C. S. (2019). Convection physics and tidal synchronization of the subdwarf binary NY Virginis. MNRAS, 485(2):2889–2894.

period and orbital period of the binaries should be the same and an observed rotation velocity would allow the inclination to be measured. Several observed sdB systems challenge this assumption (Pablo et al., 2012a,b; Schaffenroth et al., 2014). Theoretical calculations of tidal synchronization time-scales for sdB stars fail to account for synchronization via either the equilibrium or dynamical dissipation mechanisms (Preece et al., 2018).

Of the observed pulsating sdB binaries, the eclipsing HW Vir type binary NY Vir (PG 1336−018) is the only object whose outer layers show evidence of synchronous rotation with the binary orbit (Charpinet et al., 2008). The star oscillates with p-modes in its outer 55 per cent. Rotation in the deep interior is not constrained owing to the lack of sensitivity of p-modes to these regions.

Charpinet et al. (2008) obtained a mass for the sdB component of $0.459 \pm 0.006\,\mathrm{M}_\odot$ from asteroseismology, while Van Grootel et al. (2013) measured an asteroseismic mass of $0.471 \pm 0.006\,\mathrm{M}_\odot$. Vučković et al. (2007) obtained three equally probable solutions from photometry and radial velocities. These give sdB masses of 0.530, 0.466 or $0.389\,\mathrm{M}_\odot$. The companion mass M_2 is either 0.11 or $0.12\,\mathrm{M}_\odot$ and the orbital period of the binary $P_{\mathrm{orb}} = 0.101016\,\mathrm{d}$.

The tidal synchronization time-scale is inversely proportional to the ratio of the radius of the dissipative region to the binary separation to the sixth power (Darwin, 1879; Eggleton, 2006). Increasing the radius of the convective region reduces the tidal synchronization time. Observational asteroseismic data suggest the radial extent of the He burning core, as illustrated in Fig. 4.1, is substantially underestimated in stellar models (Charpinet et al., 2011; Giammichele et al., 2018; Van Grootel et al., 2010a,b). We investigate whether increasing the radius of the convective zone could reduce synchronization times sufficiently to account for the observed synchronization of NY Vir. We examine the effect that increasing the extent of the convective region has on all the quantities which go into the tidal synchronization calculations.

4.2 Stellar Models

The evolutionary models used in this study were all constructed with the Cambridge STARS code as first described by Eggleton (1971) and subsequently updated by Pols et al. (1995) and Stancliffe and Eldridge (2009). Three classes of model were created, one with overshoot (labelled: $\delta_{\mathrm{ov}} = 0.12$), one without overshoot ($\delta_{\mathrm{ov}} = 0$) and one without overshooting but with a modified Schwarzschild criterion ($\Delta\nabla + 0.15$), where $\Delta\nabla \equiv \nabla_{\mathrm{r}} - \nabla_{\mathrm{a}}$, the difference between radiative and adiabatic thermodynamic gradients $\mathrm{d}\ln T/\mathrm{d}\ln P$. Under the standard Schwarzschild criterion, the convective region is defined as that where $\Delta\nabla > 0$ and hence

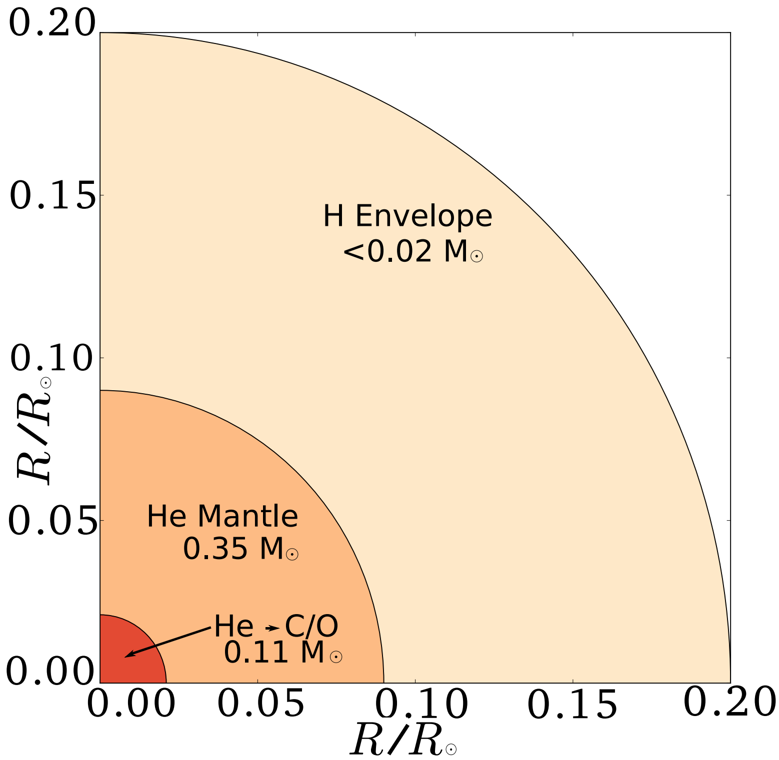

Fig. 4.1 Scale diagram of a typical sdB star as predicted by stellar models. He $\rightarrow$ C/O (red) indicates the convective zone.

includes the semi-convective region. The super-adiabacity of the convective region that develops as the star evolves is very low and is in fact more likely a semi-convective region. For each of these classes, an early and a late model were compared. The early model was defined as the model obtained when the fractional core He abundance by mass drops to 0.9. The late model was defined to be the model where the convective core reached its maximal radial extent. The initial models were constructed without a modified Schwarzschild criterion by the same method used by Preece et al. (2018). We introduce several mechanisms for artificially increasing the convective region. For the models labelled $\Delta\nabla + 0.15$, the extent of the convective region was artificially extended by modifying the Schwarzschild criterion for stability against convection from $\nabla_\mathrm{r} - \nabla_\mathrm{a} > 0$ to $\nabla_\mathrm{r} - \nabla_\mathrm{a} + 0.15 > 0$. This has the effect of forcing convection to occur in regions near to convective boundaries which would otherwise be radiative. The increment 0.15 was chosen because this was the largest which produced stable evolutionary models.

4.3 Convective Tidal Dissipation

The most efficient mechanism for tidal dissipation in sdB stars in close binaries is convective dissipation. Convection implies the bulk movement of material over large distances within the star. Turbulent viscosity in the convective region causes the tidal bulge to move away from the line connecting the centres of mass of the two stars.

The tidal synchronization time-scale τ_sync, owing to convective dissipation, as described by Eggleton (2006) and Eggleton et al. (1998), is

$$\tau_\mathrm{sync} = \frac{2}{9}\log\left(\frac{\omega - \Omega_0}{\omega - \Omega}\right)\left(\frac{M_1}{M_2}(1-Q)\right)^2\left(\frac{I}{M_1 R_1^2}\right)\frac{a^6}{R_1^6}\tau_\mathrm{visc}, \tag{4.1}$$

where I is the moment of inertia of the star, τ_visc is the viscous time, Q is the dimensionless quadrupole moment, a is the binary separation radius, R_1 is the radius of the dissipative region, M_1 is the mass of the dissipative region, M_2 is the mass of the companion, ω is the angular frequency of the binary, Ω_0 is the initial spin angular frequency of the primary and Ω is the final spin angular frequency. The viscous time τ_visc is

$$\tau_\mathrm{visc} = \frac{M_1 R_1^2}{\int_0^{M_1} wl\gamma(r)\Psi(r)dm.}, \tag{4.2}$$

where $\gamma(r)$ is a dimensionless structural property related to the coupling of the tides. The tides are described as fast when the orbital period is faster than the convective turnover time. In this circumstance the turbulent viscosity of the convective region reduces and the

Table 4.1 Convective mass, radius, dimensionless quadrupole moment and synchronization time for the models considered.

Model	$R_1/R_\odot$	$M_1/M_\odot$	Q	$(1-Q)^2$	$\tau_{\rm sync}(\Psi_1)/\mathrm{Gyr}$	$\tau_{\rm sync}(\Psi_2)/\mathrm{Gyr}$
Early $\delta_{\rm ov}=0$	0.021	0.113	0.01385	0.97250	36.47	588.63
Late $\delta_{\rm ov}=0$	0.033	0.280	0.00890	0.98228	65.31	2448.11
Early $\delta_{\rm ov}=0.12$	0.021	0.107	0.01389	0.97241	32.76	492.56
Late $\delta_{\rm ov}=0.12$	0.024	0.151	0.00802	0.98402	62.78	1007.95
Early $\Delta\nabla+0.15$	0.042	0.317	0.01078	0.97856	74.02	4222.01
Late $\Delta\nabla+0.15$	0.053	0.441	0.00867	0.98274	12.52	60.24

dissipation of the tides is less efficient. The turbulent viscosity is

$$\nu = wl\Psi(r). \tag{4.3}$$

Zahn (1966, 2008) uses a corrective factor to viscosity of $\Psi(r)$

$$\Psi_1(r) = \left|\frac{wP_{\rm orb}}{2l}\right|, \tag{4.4}$$

and Hurley et al. (2002) uses

$$\Psi_2(r) = \left|\frac{wP_{\rm orb}}{2l}\right|^2. \tag{4.5}$$

Goodman and Oh (1997); Penev et al. (2007) revisited the problem with 3D hydro-dynamical simulations and found better agreement between theory and observation with $\Psi_2(r)$.

4.3.1 The Tidal Synchronization Time-scale

As can be seen in Table 4.1, tidal synchronization time-scales for NY Vir predicted from standard models of sdB stars are close to or longer than the Hubble time. Tidal synchronization cannot occur before these models exhaust their core helium supplies, move off the EHB and on to a white dwarf cooling track. Because $\tau_{\rm sync}$ is inversely proportional to the radius of the dissipative region to the sixth power, simple calculations suggest that increasing the convective radius $r_{\rm conv}$ should substantially decrease the synchronization time. Somewhat surprisingly, increasing $r_{\rm conv}$ by a factor of 2.5 by modifying the Schwarzschild criterion only reduces the synchronization time by about an order of magnitude. The changes in the structural properties of the star affect the quadrupole tensor and so too the tides. Increases in the viscous time and mass of the convective region and decreases in the quadrupole moment and moment of inertia term counteract the effect of increasing the fractional convective radius.

The equation for tidal synchronization has multiple terms, all of which have an allowed physically constrained ranges. The dependence of the radial extent of the convective zone on the individual terms and their allowed ranges is now examined.

4.3.2 The Dimensionless Quadrupole Moment

The mass quadrupole tensor of an object describes the spatial distribution of the matter. If the object is a point source the quadrupole tensor vanishes. The dimensionless quadrupole moment Q is given in Table 4.1. Varying $r_{\rm conv}/R_{\rm sdB}$ does not particularly change Q because the early and late models with convective overshooting have the same fractional convective radius. However Q is sensitive to the total radius and density of the star and Q doesn't particularly change for the evolving models with no overshooting and a modified Schwarzschild criterion ($\Delta\nabla + 0.15$). For the models tested $(1-Q)^2$ is between 0.97 and 0.99. Because $(1-Q)^2$ is close to unity in all cases considered it does not have a substantial influence on the tidal synchronization time-scale.

4.3.3 The Mass and Radius of the Convective Region

The sdB star He cores are small but dense. The H-rich envelope is radially extended but accounts for a small amount of the mass. The mass as a function of radius can be seen in Fig. 4.2. The outer regions of the star expand as the star evolves. In addition the high internal density means a small increase in the convective radius substantially increases the convective mass. When convective overshooting is used the radius of the convective region stays approximately the same but the mass increases by half. It is worth noting that whether a region is convective or radiative has little impact on the density profile. The models with the modified Schwarzschild criterion are denser than the standard models. Furthermore, the mass and radius term in Eq. 4.1 can be plotted as in Fig. 4.3. From this the mass and radius term can be constrained to be between 10^8 and $7\times10^9\,\mathrm{g^2\,cm^{-6}}$. The lower limits are found by looking at the value when $r/R_{\rm sdB} = 0.45$ as the outer 55% as this region has been probed with asteroseismic observations and is not convective.

4.3.4 Moment of Inertia Term

For tidal calculations the ratio of the moment of inertia at the edge of the convective core to the moment of inertia if the mass were confided to a shell at the same radius is required. The overall dependence of the moment of inertia term on the fractional convective radius is displayed in Fig. 4.4. This term lies between 0.15 and 0.37. The lower limits are found by

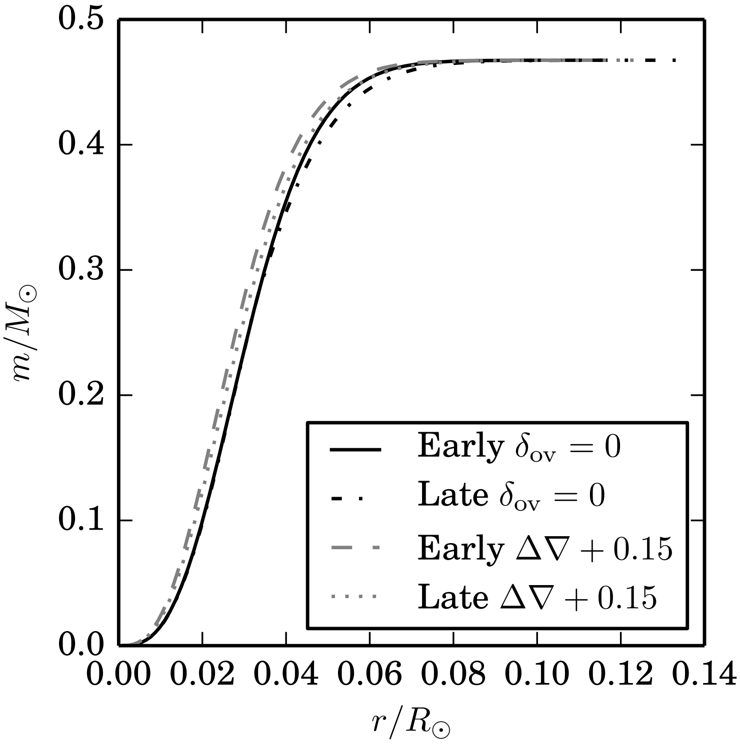

Fig. 4.2 The mass *m* contained within a sphere of radius *r*. The models with semi-convection and no convective overshooting are plotted in black and labelled $\delta_{\rm ov} = 0$. The models with no convective overshooting had the same profiles and thus are not plotted. The modified Schwarzschild criterion models, labelled $\Delta\nabla + 0.15$ and plotted in grey, are denser.

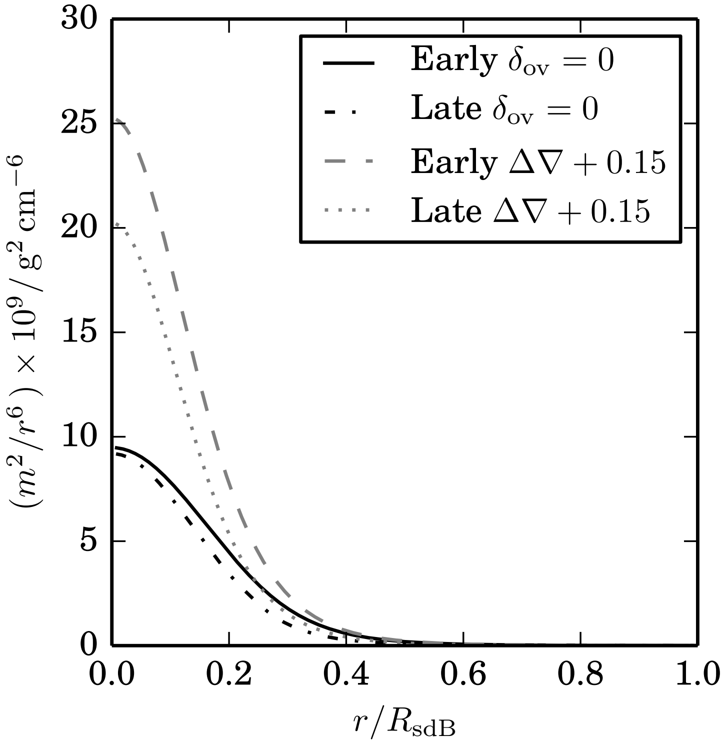

Fig. 4.3 The mass to the second power over the radius to the sixth power as a function of fractional radius for the same models as in Fig. 4.2.

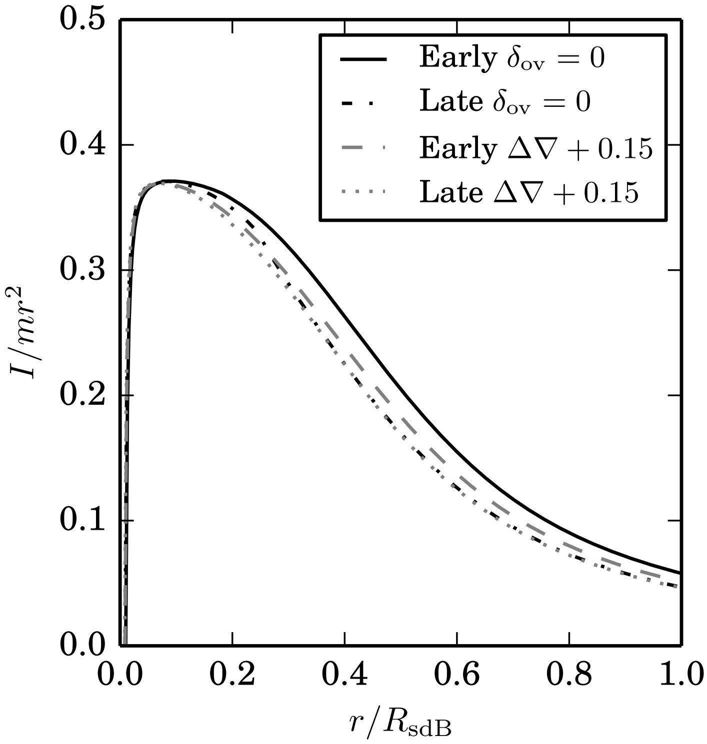

Fig. 4.4 The ratio of the moment of inertia of the region enclosed to the moment of inertia if the matter were confined to a shell placed at the same radius as a function of fractional sdB radius.

looking at the value when $r/R_{\rm sdB} = 0.45$ as the outer 55% as this region has been probed with asteroseismic observations and is not convective.

4.3.5 The Viscous Time

Tidal interactions convert kinetic energy from tidal distortions into heat by dissipative processes whilst conserving angular momentum. This dissipation can be calculated from the square of the variation in the quadrupole tensor over time. As the companion moves around the sdB star the gravitational potential through the star changes cyclically. This changes the matter distribution and so affects the quadrupole tensor. If not synchronized, the tidal bulge moves around the star following the companion. This introduces a time dependent velocity field in the dissipative regions. The dissipation has a time-scale of $\tau_{\rm visc}$.

The viscous time as calculated by Eq. 4.2 with Ψ_1 is shown in Fig. 4.5 for convective regions modified to extend throughout the star. The mixing length l used is the distance to the edge of the convective region such that at $r = 0$, $l = R_1$ and at $r = R_1$, $l = 0$. The

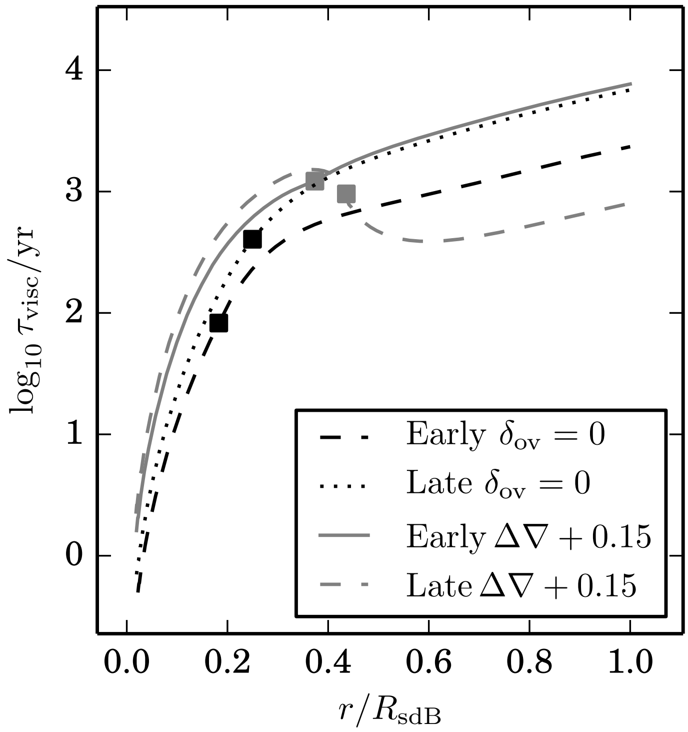

Fig. 4.5 The viscous time-scale as a function of the convective radius as a fraction of the total radius. Each line represents a single evolutionary model. The points plotted are the viscous times predicted by the stellar models with each model's convective core radius. Increasing the radius of the convective region increases the viscous time-scale. A corrective factor of Ψ_1 is used.

time-scales at the models' convective boundaries are also plotted. The $\delta_{\mathrm{ov}} = 0.12$ models are again omitted because they are almost identical to the $\delta_{\mathrm{ov}} = 0$ models. The mixing velocity w is not well defined for regions which would be radiative. If $r < R_1$ we use w from the models. If $r > R_1$, w was given the same distribution but over the extended region. The dip in the Late $\Delta\nabla + 0.15$ models is due to a large peak in $\gamma(r)$ at the convective boundary. This is most likely an artefact of our modification to the Schwarzschild criterion. Without this peak the τ_{visc} profile is almost identical to the Early $\Delta\nabla + 0.15$ profile. Overall, larger convective cores have longer viscous times.

4.3.6 Critical Viscous Time

All terms on the right hand side of Eq. 4.1 are known for any given mass and radius. The equation can be rearranged for the desired synchronization time. The maximum τ_{visc} to synchronize the system in this time as a function of convective radius can be derived. The upper limit to the viscous time for synchronization within the EHB lifetime $\tau_{\mathrm{EHB}} = 10^8\,\mathrm{yr}$ is plotted in Fig. 4.6. The viscous time as calculated with Eq. 4.2 for each of the evolutionary models in Table 4.1 is also plotted.

The τ_{visc} calculated for the models with Eq. 4.2 and the usual mixing theory estimates for the convective velocity are above the upper limits even when the corrective factor is ignored. The τ_{visc} increases as the convective core grows for all models with increasing radius owing to the high density of the material in the helium mantle. The corrective factor to the turbulent viscosity in the fast tides regime is the most influential parameter. The choice of Ψ stratifies τ_{visc} by orders of magnitude. When the corrective factor is excluded τ_{visc} does not vary much between the models and is about 10 yr. Fig. 4.6 shows that doubling the radial extent of the convective region increases the viscous time-scale by approximately an order of magnitude. If the mixing velocity is increased such that $w = l/P_{\mathrm{orb}}$ the tides are no longer considered fast and dissipation is more efficient. The convective velocity is driven by the heat flux. Increasing the velocity would cause a substantial increase in the heat flux which would then change the temperature gradient and hence the structure in other significant ways. If the convective cells turnover without releasing all of their energy to the surroundings higher velocities can be reached without changing the overall heat flux. Some 3D hydro-dynamical simulations of convective regions in stars have typical velocities which are much larger than those predicted by mixing length theory (Arnett et al., 2009; Gilkis and Soker, 2016).

The derived upper limits are all within an order of magnitude of each other. If the radius of the dissipative region is small the viscous time must be less than a year for synchronization to be achieved. For convective regions which take up more than half of the sdB star by radius the critical viscous time is less than 10 yr. This is more than the viscous time predicted when no correction to the turbulent viscosity is included.

4.4 Discussion

$J162256+473051$ is another HW Vir type system with a lower mass companion in a shorter-period orbit than NY Vir. Observations show that this star is rotating sub-synchronously. Calculations of the tidal synchronization time indicate that this system should synchronize more rapidly than NY Vir owing to its substantially smaller orbital separation. If $J162256+473051$ is neither expected nor observed to be synchronized, why should NY Vir appear to be synchronized?

HW Vir type systems are most likely formed via a common-envelope interaction (Han et al., 2002). The spin of the outer regions of the sdB star that subsequently forms are affected

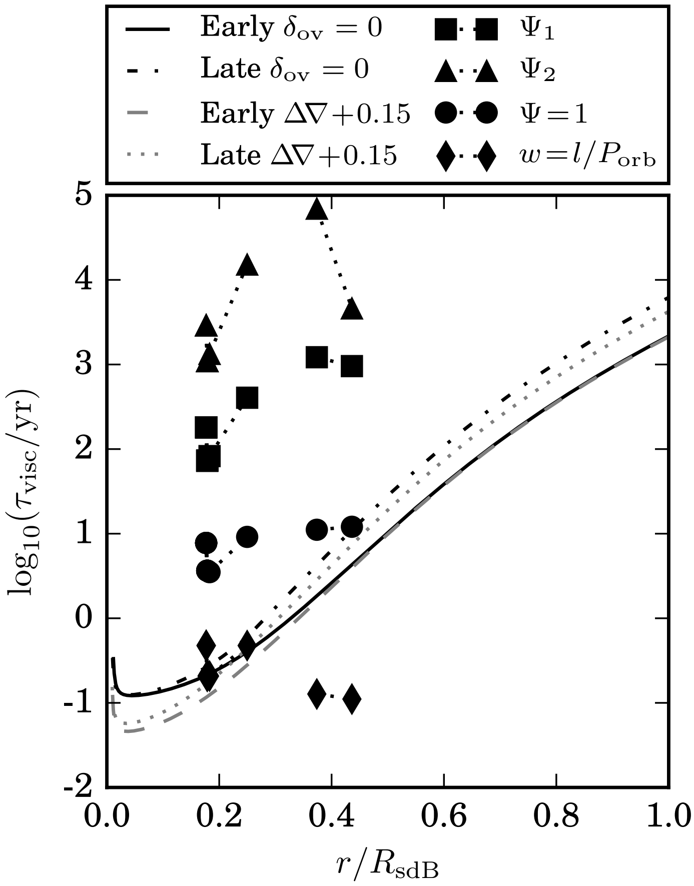

Fig. 4.6 The viscous time-scale τ_{visc} as a function of the fractional convective radius. The curves show the critical viscous time, for each convective radius, to achieve tidal synchronization during the EHB lifetime. Each line represents a single evolutionary model. The points plotted and connected with dotted lines are the viscous times predicted by the stellar models. The dotted lines connect the end points of evolutionary sequences with the same input physics ($\delta_{ov} = 0$ and $\Delta\nabla + 0.15$). For completeness the evolutionary models with convective overshoot are also plotted. The early models without a modified Schwarzschild criterion both start at almost identical places. The spread in the points is due to different corrective factors. The squares use Ψ_1, the triangles Ψ_2 and the circles $\Psi = 1$. The diamonds have the convective velocity $w = l/P_{orb}$, the minimum velocity required for the tides not to be considered fast. Increasing the fractional convective region increases the viscous time-scale.

during this process. NY Vir has p-modes which propagate through the outer 55 per cent of the star. These p-modes are consistent with synchronization. However, synchronization could have been achieved during the common-envelope phase. NY Vir's companion is more massive and more radially extended than that of $J162256+473051$ so its companion should have had more of an effect during this phase.

4.5 Conclusions

Asteroseismic evidence for rotational and orbital synchronization in the hot subdwarf binary NY Vir is at variance with our previous theoretical predictions of tidal synchronisation in such stars. Because the tidal synchronization time-scale is inversely proportional to the radius of the convective region to the sixth power artificial extensions to the convection boundary have been examined to see whether a larger convective region could account for the observed synchronization. Increasing the radius of the convective region by a factor of 2.5 decreases tidal synchronization times by less than one order of magnitude, insufficient to bring NY Vir close to synchronization within its core-helium burning (or extended horizontal-branch) lifetime. When the radius of the convective region is increased the mass also increases significantly owing to the density of the material in the vicinity. The mass increase cancels out most of the contribution from the radius. Furthermore, the moment of inertia term decreases as you move out of the star which makes the synchronization time longer.

The individual terms of Eq. 4.1 were examined to test how much each contributes to the synchronization time and what constraints may be placed on the quantities contained in them. The boundary of the convective core was moved outwards to see if there was a radius at which tidal synchronization could occur without any modifications to the theory. It was found that even making the stars fully convective would not be sufficient because the orbital periods are shorter than the convective turnover time and consequently dissipation of the tides is less efficient. The corrective factor and choice of mixing length theory are the areas of largest uncertainty. If the convective mixing velocity is increased such that $w > l/P_{\rm orb}$ all the models predict tidal synchronization within the EHB lifetime. Some 3D hydro-dynamical simulations of convective regions predict sufficiently fast convective eddies however these calculations are not enormously reliable. If these calculations prove correct, tidal synchronization might result from invocation of non-classical convection physics.

In seeking an alternative explanation for the synchronization of NY Vir, we note that the common-envelope phase is not well understood. If the tides do not synchronize on the EHB it is possible that at least the outer layers of the sdB star were synchronized during the common-envelope phase.

Chapter 5

Asteroseismology of tidally distorted sdB stars

Most subdwarf B stars are located in post common-envelope binaries. Many are in short-period systems subject to tidal influence, and many show pulsations useful for asteroseismic inference. In combination, one must quantify when and how tidal distortion affects the normal modes. We present a method for computing tidal distortion and associated frequency shifts. Validation is by application to polytropes and comparison with previous work. For typical sdB stars, a tidal distortion to the radius of between 0.2 per cent and 2 per cent is generated for orbital periods of 0.1 d. Application to numerical helium core-burning stars identifies the period and mass-ratio domain where tidal frequency shifts become significant and quantifies those shifts in terms of binary properties and pulsation modes. Tidal shifts disrupt the symmetric form of rotationally split multiplets by introducing an asymmetric offset to modes. Tides do not affect the total spread of a rotationally split mode unless the stars are rotating sufficiently slowly that the rotational splitting is smaller than the tidal splitting. [1]

5.1 Introduction

Hot subdwarf B, sdB, stars are compact He burning stars with masses of about $0.5\,\mathrm{M}_\odot$ (Heber et al., 1986). The stars have lost their H envelopes through binary evolution mechanisms (Han et al., 2002). Indeed, many of the observed systems are single lined spectroscopic binaries with orbital periods less than 10 d. Some of them are extremely close with orbital periods of only a few hours (Kupfer et al., 2015b). Whether such stars are tidally synchronized is

[1] Chapter 5 is Preece, H. P., Jeffery, C. S., and Tout, C. A. (2019a). Asteroseismology of tidally distorted sdB stars. MNRAS, 489(3):3066–3072.

debated by Preece et al. (2018). However the closest of these systems certainly experience significant tidal interactions.

A subset of the sdB stars are intrinsic variables with pulsations excited by the κ mechanism (Charpinet et al., 1996b; Kilkenny et al., 1997). Asteroseismology often relies on the assumption of spherical symmetry. The closest binary systems are sufficiently distorted by tidal interactions to break this symmetry. We investigate the significance of this on the observable pulsation frequencies of detailed numerical models.

We develop a method to estimate the perturbations to the observed eigenfrequencies owing to the tides. We compare our method to previous work in the field, mostly involving polytrope calculations, and then apply the method to detailed numerical models of sdB stars. We consider the model dependence of the results and comment upon which systems are most affected by tidal interactions.

5.2 Theoretical Background

We present a brief overview of the tidal and asteroseismological theory used in this paper.

5.2.1 Tidal Distortion

The geometric shape of the tidal distortion, to lowest order, is modelled by the second Legendre polynomial (Darwin, 1879). It is assumed that all physical properties of the star are constant along equipotential surfaces. The radius variable r which defines these equipotential surfaces

$$r = \bar{r}(1 - \alpha(\bar{r})P_2(\cos\tilde{\theta})), \tag{5.1}$$

where $\bar{r}$ is the radius of the undistorted star, $P_2(\cos\tilde{\theta})$ is the second Legendre polynomial and the angle $\tilde{\theta}$ is measured from the tidal axis. The tidal axis is directed towards the companion. The function $\alpha(\bar{r})$ can be obtained by solving Eggleton (2006)'s form of Clairaut's equation

$$\bar{r}^2\alpha'' + 4\bar{r}\alpha' - 2\alpha + 2\bar{r}\frac{\Phi''}{\Phi'}(\bar{r}\alpha' + \alpha) = 0, \tag{5.2}$$

where Φ is the gravitational potential of the star and primes denote derivatives with respect to $\bar{r}$. For a detailed, undistorted, non-rotating stellar evolution model, with a known density profile $\rho(\bar{r})$, Clairault's equation can be solved numerically. The quadrupole moment Q is defined by

$$Q = \frac{1}{5M_1R^2\alpha(R)}\int_0^R (5\alpha + \bar{r}\alpha')4\pi\rho\bar{r}^4 d\bar{r}. \tag{5.3}$$

From equation 5.1 we find at the surface $\alpha(R)$ obeys

$$\alpha(R) = \frac{-2\Delta R}{3R}, \tag{5.4}$$

where ΔR is the difference between the polar and equatorial radii. With these equations, the distortion parameter α can be determined as a function of $\bar{r}$ and a detailed distorted 2D star can be created for small α.

The Relative Magnitude of Tidal and Rotational Distortions

A three dimensional tidally and rotationally distorted star is a triaxial ellipsoid (Song et al., 2009). The tidal distortion is again prolate while the rotational distortion is oblate. If the spin is aligned with the orbital angular momentum, as is generally assumed to be the case with post-common envelope systems such as sdBs, the distortions are about different axes. For small, linear, distortions the rotational and tidal distortions are linearly additive and so can be separated.

For a synchronously rotating system the orbital and spin periods are the same. In this case a companion mass which satisfies $M_2 > M_1/2$ creates a larger tidal distortion than rotational distortion. Generally speaking, this is not the case for sdB + dM binaries so they have larger rotational distortions than tidal distortions in the event that they are synchronized. However observational results (Pablo et al., 2012a,b; Schaffenroth et al., 2014) and theoretical calculations (Preece et al., 2018, 2019) suggest that these systems may not synchronize. Even if synchronously rotating, the sdB + WD binaries have more substantial tidal deformations than rotational unless the WD mass is particularly small.

5.2.2 Polytrope Calculations

Perturbative methods applied to the pulsations of tidally distorted polytrope models give important insight into our methodology.

Pulsations in Tidally Distorted Polytrope Models

Saio (1981) calculated solutions of the rotational and tidal perturbations of non-radial oscillations in a polytropic star using perturbation theory. Ultimately, he found that the observed pulsation frequency ν obeys

$$\nu = \nu_0 - (1 - C_1)m\Omega + C_2\nu_0\left(\frac{\Omega}{\nu_0}\right)^2, \tag{5.5}$$

where Ω is the angular frequency of the star. The star is assumed to be co-rotating so this is also the orbital angular frequency. The azimuthal order of the pulsation is denoted m and ν_0 is the pulsation frequency for the undistorted star, which can be expressed as

$$\nu_0^2 = \omega_0^2 G M_1 / R_1^3, \tag{5.6}$$

where ω_0 is the dimensionless frequency, R_1 is the radius of the star, G is the gravitational constant and M_1 is the mass of the star. The second order coefficient can be expressed as

$$C_2 = X_1 + m^2 Y_1 + Z + \left(1 + \frac{3}{2}\frac{M_2}{M_1 + M_2}\right)(X_2 + m^2 Y_2). \tag{5.7}$$

For a polytrope of index $n = 3$ and an adiabatic gradient of $\gamma = 5/3$, the quantities ω_0^2, C_1, X_1, Y_1, Z, X_2 and Y_2 can be evaluated numerically. As a general result, Saio (1981) found that the p-modes are more affected by the structural perturbation owing to the tides than the g-modes. Isolating the terms proportional to M_2 from equation 5.5 shows the perturbation owing to the tides.

Application of Polytrope Results to Estimate Higher-order Effects owing to Tidal and Rotational Distortion for the Pulsating Binary System NY Virginis

Charpinet et al. (2008) applied the polytrope based calculations of Saio (1981) to evaluate the second order effects owing to tidal and rotational effects for the binary hot subdwarf system NY Virginis. These methods are non-perturbative and so have exact solutions for the pulsation frequencies. Whilst polytropes are only approximate representations of stars they give insight into which processes are important. They found that the p-modes were typically disrupted by a few μ Hz which is above detection thresholds. Both the rotation and the distortion impact the frequency splittings. Predictions from the tidal correction suggest that the different m modes are split asymmetrically. Given the ever increasing precision of observational measurements these perturbations need to be quantified for future analysis.

Perturbative Methods

Reyniers and Smeyers (2003) predict the mode splitting for tidal perturbations of linear isentropic oscillations in components of circular-orbit close binaries with perturbative methods. They predict the ratios of eigenfrequencies for the tidally perturbed stars. They make their calculations without considering rotation and thus leave open the question as to whether or not the companion is in synchronous rotation with the orbit. Fig. 5.1 depicts the ratio of the eigenfrequency splitting owing to tidal distortions. They find a difference by a factor of -2

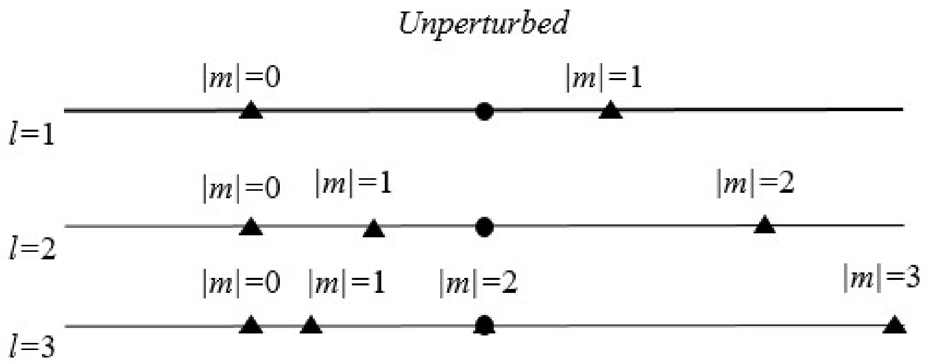

Fig. 5.1 Schematic diagram of the ratios of the eigenfrequency shifts to tidally distorted stars as presented by Reyniers and Smeyers (2003) Figs. 1,2 and 3. The perurbation to the eigenfrequencies are shown in triangular points and the unperturbed frequency is the circular point. Reyniers and Smeyers (2003) predict that the $|m| = 0$ modes are shifted to negative frequencies then the increasing $|m|$ modes cascade to higher frequencies. Saio (1981) predicts the same ratios between line splitting but the amplitudes differ by a factor of -2 meaning the $|m| = 0$ mode is higher frequency and the increasing $|m|$ modes have decreasing frequencies.

in the predicted frequency splitting compared to the results of Saio (1981). Our results agree with Saio (1981).

5.3 Methods

Detailed stellar models are computed, tidally distorted and then analysed for pulsations.

5.3.1 Stellar Evolution Code

Evolved sdB models are created with the Cambridge STARS code (Eggleton, 1971). The code uses an adaptive non-Lagrangian mesh to calculate the structure. The mesh points redistribute themselves as the star evolves. During the evolution the structure and composition are solved simultaneously. The code has been updated several times since its creation in the early 1970s. One update deals with the equation of state (Eldridge and Tout, 2004). Stancliffe and Eldridge (2009) modified the code to evolve both components in binary systems.

For this work we consider an sdB star to be a core helium burning extreme horizontal branch (EHB) star which evolved from the zero-age EHB (ZAEHB). We consider EHB models with no H envelope and models with a $0.01\,M_\odot$ H envelope. With these two evolutionary sequences the observed surface gravity $\log g_{\rm surf}$ parameter space for these objects is encompassed. As the models evolve their radii increase until a maximum is reached part way through He burning. After this point they steadily contract until He is exhausted and they settle on to the WD cooling track. We consider the ZAEHB models and the evolved models at maximum radius.

5.3.2 Tidal Distortion

The first stage is to create a single, undistorted, non-rotating sdB model as did Preece et al. (2018). Its density profile $\rho(r)$ is used to construct Clairaut's equation which is solved for $\alpha(r)$. The quadrupolar tidal distortion of a non-rotating star makes it a prolate spheroid relative to the spin axis, the equatorial radius through the axisymmetric tidal bulge (high tide) is larger than the polar radius and the equatorial radius at low tide which are equal.

The three dimensional distorted star, shown in Fig. 5.2, is generated with equation 5.1, in which $\tilde{\theta}$ is the angle from the tidal axis, directed towards the companion. A right angled triangle can be projected on to the surface of the 3D star to find $\tilde{\theta}(\theta,\phi)$ where θ and ϕ are the usual spherical co-ordinates with the z-axis aligned with the spin axis. The axisymmetric tidal bulges are at $\theta=\pi/2$, $\phi=0,\pi$. Application of the spherical cosine rule gives $\cos(\tilde{\theta})=-\sin(\theta)\cos(\phi)$. The radius of the equipotentials $r(\theta,\phi)$ is then

$$r(\theta,\phi)=\bar{r}[1-\alpha(\bar{r})P_2(-\sin\theta\cos\phi)]. \tag{5.8}$$

The previously spherical shells of the model are treated as equipotential surfaces. The tidal distortion is applied to every shell. It is assumed that the physical properties of the object are constant along equipotential surfaces of the tidally distorted star. Recall that for a synchronously rotating system the tidal distortion is greater than the rotational distortion if the companion mass satisfies $M_2>M_1/2$.

5.3.3 Obtaining Asteroseismic Eigenfrequencies

We obtain our asteroseismic eigenfreqencies using the open source oscillation code GYRE (Townsend et al., 2018; Townsend and Teitler, 2013). GYRE is a 1D code that solves the adiabatic and non-adiabatic pulsation equations to obtain eigenfrequencies and eignenfunctions for a given stellar model. We developed a back end for the STARS code which allows STARS models to be analysed by GYRE. For convenience of comparison the STARS models are written in the same format as MESA models (Paxton et al., 2011, 2013). For each point (θ,ϕ) on the surface of the tidally distorted star a set of local eigenfrequencies $\nu(\theta,\phi)$ can be found by applying the GYRE analysis to a spherically symmetric star with local radius $r=r(\alpha(\bar{r}),\theta,\phi)$. For p-modes the models at the rotation poles have higher pulsation frequencies than those at the equator. Fig. 5.2 shows the local fractional shift in the eigenfrequency on the surface of a tidally distorted polytrope model for a selected p mode.

5.3.4 Volume Averaged Frequency

Exploiting the azimuthal symmetry of the bulge, the m degenerate global volume averaged frequency $\bar{\nu}$ can be found by integrating $\nu(\theta,\phi)$ over the surface of the entire star. We find that the global average frequency is the same as that of the undistorted model. This is the case for the $l=0$ mode. Asteroseismic pulsations are described by the spherical harmonics with radial order k, number of node lines on the surface l and number of node lines passing through the equator m. For each l there are $2l+1$ possible m modes. When the star is spherically symmetric, the m modes are all degenerate for a given l. When the spherical symmetry is broken the degeneracy of the m modes is also broken. With the spherical harmonics, $Y_l^m(\theta,\phi)$, we estimate the frequency for each m mode with

$$\bar{\nu} = \frac{\int_0^{2\pi}\int_0^{\pi} |Y_l^m(\theta,\phi)|^2 \nu(\theta,\phi) \sin\theta d\theta d\phi}{\int_0^{2\pi}\int_0^{\pi} |Y_l^m(\theta,\phi)|^2 \sin\theta d\theta d\phi}, \tag{5.9}$$

which reduces to

$$\bar{\nu} = \frac{\int_0^{2\pi}\int_0^{\pi} |P_l^m(\cos\theta)|^2 \nu(\theta,\phi) \sin\theta d\theta d\phi}{\int_0^{2\pi}\int_0^{\pi} |P_l^m(\cos\theta)|^2 \sin\theta d\theta d\phi}. \tag{5.10}$$

where $P_l^m(\cos\theta)$ are the associated Legendre polynomials.

5.3.5 Magnitude of the Tidal Distortion

The magnitude of the tidal distortion depends on the orbital period and the mass ratio of the two stars. The percentage magnitude ($100\Delta R/R$) is plotted in Fig. 5.3 for three evolutionary models. The radius of the star is the most important parameter for calculating the magnitude of the distortion. Doubling the radius of the star increases the distortion by a factor of 5. For systems with $P_{\mathrm{orb}} > 0.5\,\mathrm{d}$ the distortion is less than 0.02 per cent.

The post common envelope sdB systems have either dM or WD companions. We consider two companion masses for the remainder of this work $M_{2\mathrm{a}} = 0.11\,\mathrm{M}_\odot$ and $M_{2\mathrm{b}} = 0.4\,\mathrm{M}_\odot$ which correspond to the two peaks of the observed bimodal companion mass distribution (Kupfer et al., 2015b). The mass $M_{2\mathrm{a}}$ is typical of an sdB + dM and $M_{2\mathrm{b}}$ is more representative of an sdB + WD system. Furthermore, $M_{2\mathrm{a}}$ is the same as that predicted for the system NY Virginis which is one of the closest binary systems containing a pulsating sdB star observed to date.

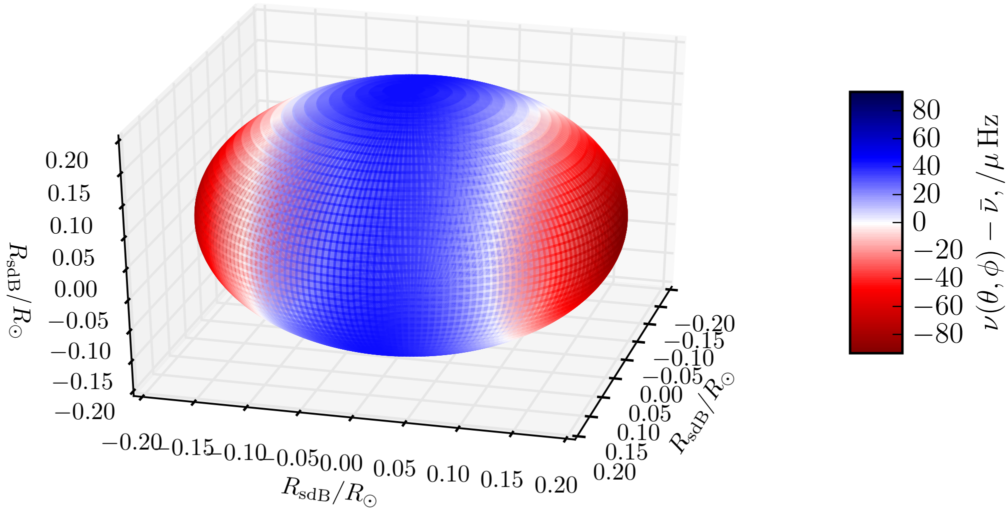

Fig. 5.2 Tidal distortion of a sdB numerical model with the binary properties of NY Virginis. The contour shows the radial distortion of the star in 3D. The colour of the surface shows the fractional frequency shift $(\nu(\theta,\phi)-\bar{\nu})/\bar{\nu}$. The tidal bulge, which has the largest radius, is shifted to lower frequencies. The pole and the low-tide region are shifted to higher frequencies. The white ring shows the location of undistorted frequencies. The frequency shift around any cross-section with fixed $\tilde{\theta}$ is constant.

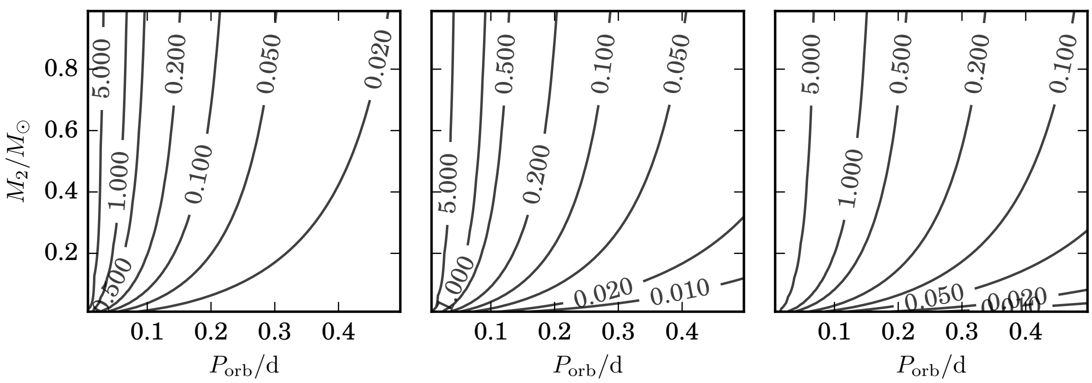

Fig. 5.3 A contour plot in orbital period P_{orb} and companion mass M_2 of the percentage of the tidal distortion. The contours show the percentage of the tidal distortion ($100\Delta R/R$). The left hand panel is a ZAEHB model with no H envelope and $\log_{10}(g_{\mathrm{surf}}/\mathrm{cm\,s^{-2}}) = 5.982$. The middle panel is an sdB with no envelope which has evolved until the radius is at the evolutionary maximum and has $\log_{10}(g_{\mathrm{surf}}/\mathrm{cm\,s^{-2}}) = 5.809$. The right hand panel is a ZAEHB detailed evolutionary model of an sdB star with canonical mass $0.47\,\mathrm{M}_{\odot}$, radius of $0.19\,\mathrm{R}_{\odot}$, $M_{\mathrm{env}} = 0.01\,M_{\odot}$ and $\log_{10}(g_{\mathrm{surf}}/\mathrm{cm\,s^{-2}}) = 5.515$.

5.4 Results

Averaging $\nu(\theta,\phi)$ for polytropic models with the spherical harmonics gives the same ratios of m splitting as predicted by both Saio (1981) and Reyniers and Smeyers (2003) for the $l=1$ to $l=3$ modes. The magnitudes and directions of the frequency shifts are in agreement with Saio (1981). We compare the polytrope mode to a detailed numerical model of an sdB star. We also predict the $l=4$ and $l=5$ mode splitting owing to tidal effects in this work. This mode is observed in p-mode pulsating sdB stars. The $l=0$ mode is unaffected by tidal interactions.

5.4.1 Calibration of Polytrope Models

Saio (1981) numerically evaluated the required quantities for equation 5.5 with an $n=3$ but $\gamma=5/3$ polytropic stellar model. The results of these calculations test the effectiveness of our method. We numerically solve the Lane-Emden equation to generate our own polytropic model to make a comparison.

The eigenfrequency of a pulsation mode in a star with given mass and radius can be found with equation 5.6. The m dependent shift $\delta\nu_m$ in the eigenfrequency follows

$$\delta\nu_m = \left(\frac{3}{2}\frac{M_2}{(M_1+M_2)}\right)(X_2+m^2Y_2)\nu_0\left(\frac{\omega}{\nu_0}\right)^2, \tag{5.11}$$

where X_2 and Y_2 are calculated numerically and tabulated by Saio (1981).

We obtain frequencies for our tidally distorted numerical polytrope model using the full methodology laid out in section 5.3. The positive and negative m modes for a given l and k have the same perturbation to the frequency owing to tidal perturbations. The different m modes have different tidal frequency perturbation magnitudes which result in asymmetric mode splitting.

To cast more light on whether the magnitude of the shift of the frequency predicted by Saio (1981) or Reyniers and Smeyers (2003) is correct, the polytrope $\nu(\theta,\phi)$ obtained from GYRE can be compared to their respective results. Fig. 5.4 shows our method compared to Saio (1981). Whilst not identical there is a good agreement. Saio's lower radial order modes are perturbed more than ours and our higher radial order modes are perturbed more than his but the difference is always within a few micro-Hertz. No corrective factor is required for these results. The magnitude and direction of our frequency shift agrees with Saio (1981).

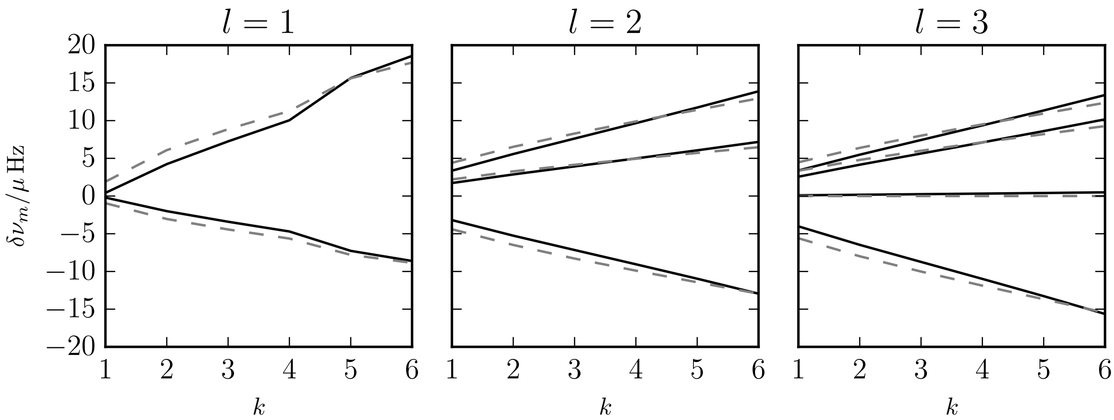

Fig. 5.4 Comparison of our (solid black) polytrope calculations to those of Saio (dashed grey) for a polytrope model with the binary parameters of NY Virginis. As illustrated in Fig. 5.1, the $m=0$ line is most positively shifted, the increasing $|m|$ eigenfrequencies linearly cascade down until the $|m|=l$ eigenfrequency which is shifted the most negatively. The magnitude of our frequency perturbations differ from Reyniers and Smeyers (2003) by a factor of -2. The frequencies used for our polytrope model are output by GYRE. No corrective factor is applied to the frequency magnitudes.

5.4.2 Comparison of Polytropic and Numerical Models

Fig. 5.5 shows the comparison of our polytrope to our detailed stellar model. The magnitude of the frequency perturbation owing to tidal interactions for the polytrope is larger than that for the detailed stellar model even though the surface tidal distortion is the same. This particularly applies to the higher radial order modes so that an $n=3$, $\gamma=5/3$ polytrope is not the best approximation for an sdB star. If the system is tidally synchronized, the tidally induced splitting is smaller than the rotational splitting. For the numerical models the frequency splitting is generally far smaller than the rotational splitting. However the rotation period of the star is not as well constrained as the orbital period.

5.4.3 Tidal and Rotational Splitting

The rotation rate of sdB stars in close binaries is not well constrained. Table 3.1 shows the close sdB binary population with known orbital and spin periods. *Kepler* observations of pulsating systems with orbital periods greater than 0.3 d show that these systems rotate with periods of the order of days and thus are certainly rotating sub-synchronously. The observed pulsation frequencies of these longer period close binaries show symmetric rotational splitting. This means the measured rotation periods are precise. Another implication is that the tides do not operate strongly in these regimes. The presence of significant tidal interactions spins up

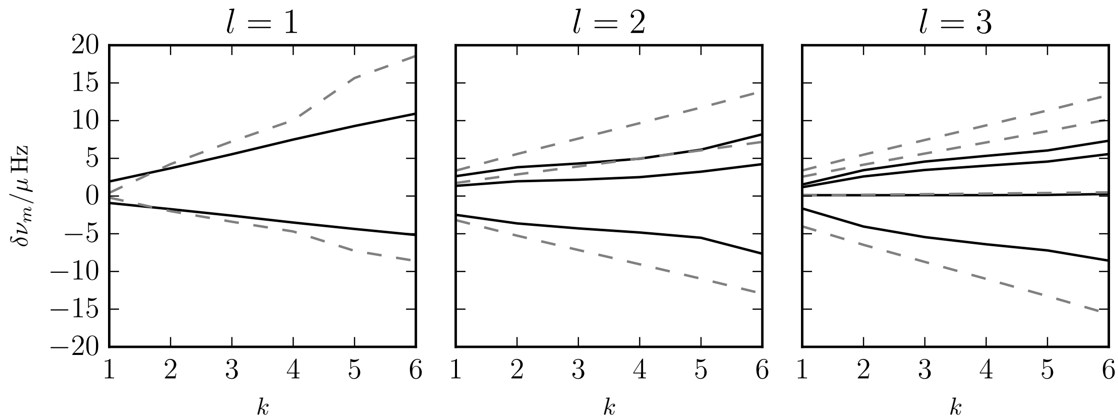

Fig. 5.5 As Fig. 5.4, comparing our numerical (solid black) calculations to our polytrope models (dashed grey).

the star and introduces asymmetric splitting. The closest of the sdB systems are rotationally spun up relative to their longer period counterparts. However, assuming current convection theory, they are still unlikely to be synchronized to their orbits (Preece et al., 2019).

Observational and theoretical results both suggest that the sdB stars are not synchronously rotating, even when in the closest configurations. This makes including rotational effects more complicated. Were the stars co-rotating with the orbit then the rotational splitting would be well constrained. Knowing the best rotation period to apply is a tricky business!

Whilst most likely sub-synchronous, the stars are still rotating. The rotational splitting is constant for all modes assuming the star is rotating as a solid body in the regions probed by the pulsations. This may not be a good assumption for these systems. Fig. 5.6 shows the rotation and tidal splitting of the modes for a companion mass of $0.1\,\mathrm{M}_{\odot}$ for a star with a rotation period equal to double the orbital period. The $m = 0$ mode is influenced the most. The splitting of the modes becomes asymmetric. At short orbital periods the tides become more significant. At the shortest periods the asymmetry of the modes becomes quite substantial. This has significant implications for the mode identification of an observed pulsation spectrum.

Whilst the splitting becomes asymmetric, the total spread of a mode owing to rotation doesn't change with the introduction of tides. The $m = \pm l$ modes both experience the same frequency perturbation owing to the tides and so the total spread of a multiplet remains constant. This may be helpful in the identification of modes. This also means it is still possible to infer the rotation rate of the region from the multiplet splitting.

Because the rotation periods are generally not well constrained for the short period systems we consider a system with fixed orbital period and companion mass and alter the rotation period. The results of these calculations can be seen in Fig.5.7. We approximate the

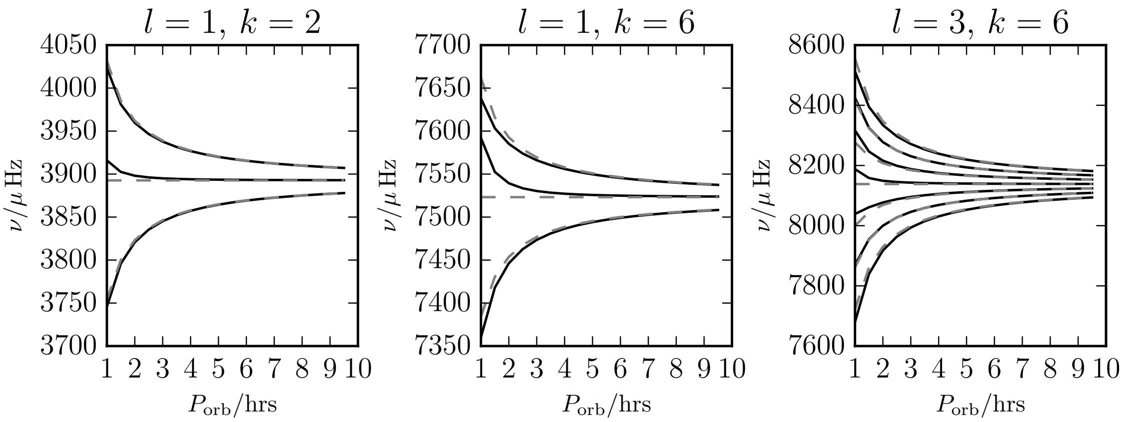

Fig. 5.6 The frequency perturbation for selected eigenmodes as a function of orbital period. For these plots it is assumed that the stars are rotating with a spin period double the orbital period. The companion mass is $0.1\,M_\odot$. When the rotational splitting is added, the $m = 0$ line is the central line. The higher m eigenfrequencies then split around the $m = 0$ line in the typical pattern. The dashed grey lines show only rotational splitting for reference.

rotational eigenfrequency splitting $\delta\nu_{\rm rot} \approx 1/P_{\rm rot}$. The observed order of the modes changes as the stars spin up. If the star isn't rotating the $|m|$ modes are degenerate. As rotation is introduced this $|m|$ degeneracy is slowly broken. At spin periods greater than 18 hr for the $m = 0$ the tidal effects dominate and the order of the modes from positive to negative frequency perturbation is $m = 0$, then $m = -1$ then $m = 1$. At rotation periods of less than 18 hr the rotation starts to dominate and the observed order of the modes becomes $m = -1$, then $m = 0$ then $m = 1$. The equator is the rotational axis which is perpendicular to the axis with the tidal bulge.

5.4.4 Higher Order Modes

The splitting of $l = 4$ and $l = 5$ modes owing to the tidal distortion has not previously been computed. However, this mode is sometimes identified in observed pulsation spectra so is of some interest. Table 5.1 shows the frequency perturbation relative to the $m = 0$ mode, $\delta\nu_0$ for $m > 0$ and $l = 4$ and $l = 5$. Recall that $\delta\nu_m = \delta\nu_{-m}$.

5.5 Discussion

The sdB stars have $5 < \log_{10}(g_{\rm surf}/{\rm cm\,s^{-2}}) < 6$ and masses sharply peaked at $0.47\,M_\odot$. The radii of these stars varies substantially depending on the H envelope mass. The envelope is low mass but radially extended. A ZAEHB sdB star with no H envelope experiences a tidal

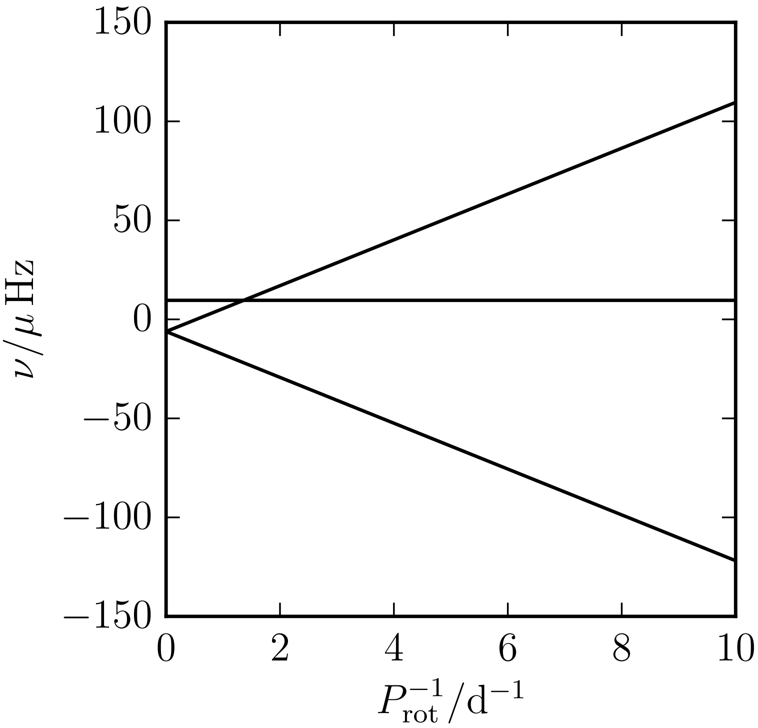

Fig. 5.7 The frequency perturbation for the $l = 1$, $k = 6$ eigenmode with a fixed orbital period and variable rotation period as a function of $1/P_{\rm rot}$ for a binary system with $P_{\rm orb} = 0.1\,{\rm d}$ and $M_2 = 0.1\,{\rm M}_\odot$. The $m = 0$ mode is unaffected by the spin. As the star spins up the tidal degeneracy between the $m = \pm 1$ modes is broken.

Table 5.1 Predicted $|m|$ dependent frequency perturbation owing to tidal interactions for the $l = 4$ and $l = 5$ modes.

Mode	$l = 4$	$l = 5$
$\delta\nu_1$	0.828 $\delta\nu_0$	0.885 $\delta\nu_0$
$\delta\nu_2$	0.312 $\delta\nu_0$	0.541 $\delta\nu_0$
$\delta\nu_3$	-0.548 $\delta\nu_0$	-0.034 $\delta\nu_0$
$\delta\nu_4$	-1.752 $\delta\nu_0$	-0.837 $\delta\nu_0$
$\delta\nu_5$	-	-1.871 $\delta\nu_0$

distortion 5 times smaller than a ZAEHB sdB with $M_{\rm env} = 0.01\,\mathrm{M}_\odot$. As an sdB star evolves the He burning region increases in mass. The star also expands for a period of time until $\log g_{\rm surf}$ reaches a minimum and then contracts again. Fig. 5.3 compares three models with different envelopes and at different evolutionary stages to characterize these effects. Our results suggest that if the distortion is less than 1 per cent the frequencies are not significantly altered.

The version of the STARS code used in this work does not include atomic processes such as radiative levitation and gravitational settling. The inclusion of convective overshooting alters the evolution of the models. With no overshooting a large semi-convective region forms around the convective He fusing core. The models with overshooting typically have smaller radii in which case pulsations would be less influenced by the tides.

5.6 Conclusions

Tides play an important role in binary star interactions. The sdB systems typically do not experience tides strong enough to synchronize the systems during their extreme horizontal branch evolution but the closest systems are still significantly distorted and spun up. The pulsations observed for these systems are influenced by the tidal distortions. The perturbations to the frequencies owing to the tides are typically smaller than the rotational effects if the stars are significantly spun up, particularly for the sdB + dM systems. Whilst often subtle, the tides still have an observable effect on the *m* splitting. At high spin rates the observed order of the modes, and total spread of the multiplet, is not affected by the tides but the splitting becomes asymmetric and this has important implications for the mode identification. At low spin rates the order of the modes is altered.

Chapter 6

Conclusions

Post common-envelope binary stars can be used as test-beds for tidal synchronization theories. During common-envelope evolution the orbital period substantially shrinks on a dynamical time-scale. The orbital shrinkage means any synchronization achieved on the the RGB is broken and this determines the initial spin period. Observational data confirm that sdBs in sdB+dM systems with orbital periods of about half a day are not significantly spun-up relative to their red clump counterparts and have spin periods of the order of 10 d.

The sdB stars in the closest binaries are certainly spun-up but neither dynamical nor equilibrium tidal theory predicts synchronization within the EHB lifetime with standard input physics. The only way synchronization of the cores could be achieved in this study was to speed up the convecting material in the star such that the convective turnover time was shorter than the orbital period. The required convective velocity is far smaller than the sound speed in the core but still needs to be enhanced by a factor of about 20 without modifying the overall energy flux. Some 3D hydro-dynamical simulations reach the required velocities. However the results are somewhat unreliable and haven't been applied to He burning cores. It may be possible for the common-envelope evolution phase to spin-up the outer regions of the star – in particular the remaining low-mass radially-extended H envelope. Unfortunately, the common-envelope phase is not well understood and this hypothesis remains beyond robust testing with existing theories.

Without considering the contributions of resonances, the dynamical tide for the sdB stars predicts synchronization time-scales on the order of the Hubble time even for systems such as CD-30°11223. Studies investigating white dwarf tidal synchronization show that resonance of the tidal potential with a g-mode in the star becomes significant at orbital periods of less than an hour (Fuller and Lai, 2012). These systems only approach spin-orbit synchronization such that $\omega/\Omega > 0.8$ when the orbital period is less than 20 min. Even at orbital periods less than 10 min some of the white dwarf models still maintain some degree of asynchronicity.

The white dwarf binary systems are far closer than any observed sdB system and thus it seems safe to conclude that this mechanism is no more efficient than the convective dissipation.

Tidal deformations influence the asteroseismic pulsations of a star by breaking spherical symmetry. We showed that it is possible to recover analytical predictions of the shifts to the m mode eigenfrequencies. The aim of this project was to answer the question of whether the tides affect the pulsations of the stars to an observable degree. The shifts to the eigenfrequencies depend on a multi-dimensional parameter space including the radius of the star, the radius of the convective region, the mass of the star, the mass of the companion, the separation of the stars and the k, l and m of a pulsation mode. The higher k modes are effected substantially more than the lower k modes and certainly to an observable degree if the orbital periods are less than a few hours. For an $l = 1$, $k = 6$ mode the splitting between the $m = 0$ and $m = -1$ mode is four times smaller than between the $m = 0$ and $m = 1$ mode. The tidal contribution becomes more substantial when the stars are rotating sub-synchronously. In many cases the tidal perturbations are small. However they can significantly alter the architecture of a rotationally split multiplet.

The mode analysis, in particular the mode identification process, for observed pulsating stars is highly non-trivial. To simplify it one generally only considers the first order rotational splitting and neglects the tidal contribution. Recent space missions including *Kepler*, *TESS* and the future mission *PLATO* have hugely increased the precision of asteroseismological measurements. Observations are now able to observe with μHz precision making the tidal contribution, for the first time, observable. Unfortunately, none of the *TESS* candidate sdB stars have observable rotational splitting to date.

To better understand the influence of the tides more close binary sdB systems must be observed. Currently there are several systems with orbital periods of 0.1 d which have been observed and are sufficiently influenced by the tides to be spun-up, even if not totally synchronized. There are also a collection of systems at orbital periods of about 0.4 d which are observed not to be spun up. To further parameterize the effect of tides on the pulsation properties of the stars ellipsoidal variations may be useful. Ellipsoidal variations give insights into the magnitude of the tidal distortion. As shown in Chapter 5 the magnitude of the distortion is linearly related to the perturbation to the pulsations. Furthermore, the ellipsoidal variations may be further disrupted if the stars also experience rotational distortion. Tidally distorted rapidly rotating stars are triaxial ellipsoids. Future work should demonstrate how this geometry affects the light-curve both with and without the presence of pulsations.

References

Aerts, C., Christensen-Dalsgaard, J., and Kurtz, D. W. (2010). *Asteroseismology*. Springer.

Ahmad, A. and Jeffery, C. S. (2005). Discovery of pulsation in a helium-rich subdwarf B star. *A&A*, 437(3):L51–L54.

Anders, E. and Grevesse, N. (1989). Abundances of the elements - Meteoritic and solar. *GCA*, 53:197–214.

Arnett, D., Meakin, C., and Young, P. A. (2009). Turbulent Convection in Stellar Interiors. II. The Velocity Field. *ApJ*, 690:1715–1729.

Baker, N. and Kippenhahn, R. (1962). The Pulsations of Models of δ Cephei Stars. With 17 Figures in the Text. *ZAP*, 54:114.

Baran, A. S., Telting, J. H., Németh, P., Østensen, R. H., Reed, M. D., and Kiaeerad, F. (2016). A subsynchronously rotating pulsating subdwarf B star in a short-period binary with a white dwarf companion. *A&A*, 585:A66.

Battich, T., Miller Bertolami, M. M., Córsico, A. H., and Althaus, L. G. (2018). Pulsational instabilities driven by the $\in$ mechanism in hot pre-horizontal branch stars. I. The hot-flasher scenario. *A&A*, 614:A136.

Bloecker, T. (1995). Stellar evolution of low and intermediate-mass stars. I. Mass loss on the AGB and its consequences for stellar evolution. *A&A*, 297:727.

Bloemen, S., Hu, H., Aerts, C., Dupret, M. A., Østensen, R. H., Degroote, P., Müller-Ringat, E., and Rauch, T. (2014). The blue-edge problem of the V1093 Herculis instability strip revisited using evolutionary models with atomic diffusion. *A&A*, 569:A123.

Böhm-Vitense, E. (1958). Über die Wasserstoffkonvektionszone in Sternen verschiedener Effektivtemperaturen und Leuchtkräfte. Mit 5 Textabbildungen. *Zeitschrift fuer Astrophysik*, 46:108.

Brickhill, A. J. (1991). The pulsations of ZZ Ceti stars. III - The driving mechanism. *MNRAS*, 251:673–680.

Burrows, A., Marley, M., Hubbard, W. B., Lunine, J. I., Guillot, T., Saumon, D., Freedman, R., Sudarsky, D., and Sharp, C. (1997). A Nongray Theory of Extrasolar Giant Planets and Brown Dwarfs. *ApJ*, 491(2):856–875.

Castellani, M. and Castellani, V. (1993). Mass Loss in Globular Cluster Red Giants: an Evolutionary Investigation. *ApJ*, 407:649.

Charpinet, S., Fontaine, G., Brassard, P., Chayer, P., Green, E. M., and Randall, S. K. (2007). Ten years of asteroseismic modelling of pulsating B subdwarf stars: achievements, challenges, and prospects. *Communications in Asteroseismology*, 150:241.

Charpinet, S., Fontaine, G., Brassard, P., and Dorman, B. (1996a). The Potential of Asteroseismology for Hot, Subdwarf B Stars: A New Class of Pulsating Stars? *ApJ Letters*, 471:L103.

Charpinet, S., Fontaine, G., Brassard, P., and Dorman, B. (1996b). The Potential of Asteroseismology for Hot, Subdwarf B Stars: A New Class of Pulsating Stars? *ApJ Letters*, 471:L103.

Charpinet, S., Van Grootel, V., Fontaine, G., Brassard, P., Green, E. M., and Randall, S. K. (2013). g-Mode Oscillations in Hot B Subdwarf Stars. In Shibahashi, H. and Lynas-Gray, A. E., editors, *Progress in Physics of the Sun and Stars: A New Era in Helio- and Asteroseismology*, volume 479 of *Astronomical Society of the Pacific Conference Series*, page 263.

Charpinet, S., Van Grootel, V., Fontaine, G., Green, E. M., Brassard, P., Randall, S. K., Silvotti, R., Østensen, R. H., Kjeldsen, H., Christensen-Dalsgaard, J., Kawaler, S. D., Clarke, B. D., Li, J., and Wohler, B. (2011). Deep asteroseismic sounding of the compact hot B subdwarf pulsator KIC02697388 from Kepler time series photometry. *A&A*, 530:A3.

Charpinet, S., Van Grootel, V., Reese, D., Fontaine, G., Green, E. M., Brassard, P., and Chayer, P. (2008). Testing the forward modeling approach in asteroseismology. II. Structure and internal dynamics of the hot B subdwarf component in the close eclipsing binary system PG 1336-018. *Astron. Ap.*, 489:377–394.

Christensen-Dalsgaard, J. and Gough, D. O. (1976). Towards a heliological inverse problem. *Nature*, 259:89–92.

Claret, A. and Cunha, N. C. S. (1997). Circularization and synchronization times in Main-Sequence of detached eclipsing binaries II. Using the formalisms by Zahn. *A&A*, 318:187–197.

Clausen, D. and Wade, R. A. (2011). How to Make a Singleton sdB Star via Accelerated Stellar Evolution. *ApJ*, 733:L42.

Constantino, T., Campbell, S. W., Christensen-Dalsgaard, J., Lattanzio, J. C., and Stello, D. (2015). The treatment of mixing in core helium burning models - I. Implications for asteroseismology. *MNRAS*, 452:123–145.

Conte, S. D. and Boor, C. W. D. (1980). *Elementary Numerical Analysis: An Algorithmic Approach*. McGraw-Hill Higher Education, 3rd edition.

Copperwheat, C. M., Morales-Rueda, L., Marsh, T. R., Maxted, P. F. L., and Heber, U. (2011). Radial-velocity measurements of subdwarf B stars. *MNRAS*, 415(2):1381–1395.

Copperwheat, C. M., Morales-Rueda, L., Marsh, T. R., Maxted, P. F. L., and Heber, U. (2011). Radial-velocity measurements of subdwarf B stars. *MNRAS*, 415:1381–1395.

Cowling, T. G. (1941). The non-radial oscillations of polytropic stars. *MNRAS*, 101:367.

Cox, J. P. (1967). The Linear Theory: Initiation of Pulsational Instability in Stars. In Thomas, R. N., editor, *Aerodynamic Phenomena in Stellar Atmospheres*, volume 28 of *IAU Symposium*, page 3.

Darwin, G. H. (1879). On the Bodily Tides of Viscous and Semi-Elastic Spheroids, and on the Ocean Tides upon a Yielding Nucleus. *Philosophical Transactions of the Royal Society of London Series I*, 170:1–35.

D'Cruz, N. L., Dorman, B., Rood, R. T., and O'Connell, R. W. (1996). The Origin of Extreme Horizontal Branch Stars. *ApJ*, 466:359.

de Mink, S. E., Sana, H., Langer, N., Izzard, R. G., and Schneider, F. R. N. (2014). The Incidence of Stellar Mergers and Mass Gainers among Massive Stars. *Astrophysical Journal*, 782:7.

Duchêne, G. and Kraus, A. (2013). Stellar Multiplicity. *ARAA*, 51(1):269–310.

Edelmann, H., Heber, U., Altmann, M., Karl, C., and Lisker, T. (2005). High resolution spectroscopy of bright subdwarf B stars. *A&A*, 442(3):1023–1030.

Eggleton, P. (2006). *Evolutionary Processes in Binary and Multiple Stars*. Cambridge Astrophysics. Cambridge University Press.

Eggleton, P. P. (1971). The evolution of low mass stars. *MNRAS*, 151:351.

Eggleton, P. P. (1972). Composition changes during stellar evolution. *MNRAS*, 156:361.

Eggleton, P. P. (1983). Approximations to the radii of Roche lobes. *ApJ Supplement*, 268:368.

Eggleton, P. P., Kiseleva, L. G., and Hut, P. (1998). The Equilibrium Tide Model for Tidal Friction. *ApJ*, 499:853–870.

Eldridge, J. J. and Tout, C. A. (2004). A more detailed look at the opacities for enriched carbon and oxygen mixtures. *MNRAS*, 348:201–206.

Fernandes, C. S., Van Grootel, V., Salmon, S. J. A. J., Aringer, B., Burgasser, A. J., Scuflaire, R., Brassard, P., and Fontaine, G. (2019). Evolutionary Models for Ultracool Dwarfs. *ApJ*, 879(2):94.

Fontaine, G., Brassard, P., Charpinet, S., Green, E. M., Randall, S. K., and Van Grootel, V. (2012). A preliminary look at the empirical mass distribution of hot B subdwarf stars. *ApJ*, 539:A12.

Fontaine, G., Green, E., Charpinet, S., Latour, M., Randall, S., Van Grootel, V., and Brassard, P. (2014). Observational Asteroseismology of Hot Subdwarf Stars with the Mont4K/Kuiper Combination at the Steward Observatory Mount Bigelow Station. In van Grootel, V., Green, E., Fontaine, G., and Charpinet, S., editors, *6th Meeting on Hot Subdwarf Stars and Related Objects*, volume 481 of *Astronomical Society of the Pacific Conference Series*, page 19.

Fuller, J. and Lai, D. (2012). Dynamical tides in compact white dwarf binaries: tidal synchronization and dissipation. *MNRAS*, 421(1):426–445.

Gabriel, M., Noels, A., Montalbán, J., and Miglio, A. (2014). Proper use of Schwarzschild Ledoux criteria in stellar evolution computations. *A&A*, 569:A63.

Geier, S. and Heber, U. (2012). Hot subdwarf stars in close-up view. *A&A*, 543:A149.

Geier, S., Heber, U., Podsiadlowski, P., Edelmann, H., Napiwotzki, R., Kupfer, T., and Müller, S. (2010). Hot subdwarf stars in close-up view. I. Rotational properties of subdwarf B stars in close binary systems and nature of their unseen companions. *A&A*, 519:A25.

Giammichele, N., Charpinet, S., Fontaine, G., Brassard, P., Green, E. M., Van Grootel, V., Bergeron, P., Zong, W., and Dupret, M.-A. (2018). A large oxygen-dominated core from the seismic cartography of a pulsating white dwarf. *Nature*, 554:73–76.

Gilkis, A. and Soker, N. (2016). Angular Momentum Fluctuations in the Convective Helium Shell of Massive Stars. *ApJ*, 827:40.

Giuricin, G., Mardirossian, F., and Mezzetti, M. (1984). Synchronization in early-type spectroscopic binary stars. *A&A*, 135:393–396.

Goldreich, P., Murray, N., and Kumar, P. (1994). Excitation of solar p-modes. *ApJ*, 424:466–479.

Goldreich, P. and Nicholson, P. D. (1977). Turbulent Viscosity and Jupiter's Tidal Q. *ICARUS*, 30(2):301–304.

Goodman, J. and Oh, S. P. (1997). Fast Tides in Slow Stars: The Efficiency of Eddy Viscosity. *ApJ*, 486(1):403–412.

Gough, D. O. (1996). Asteroseismology. *The Observatory*, 116:313–315.

Green, E. M., Fontaine, G., Reed, M. D., Callerame, K., Seitenzahl, I. R., White, B. A., Hyde, E. A., Østensen, R., Cordes, O., Brassard, P., Falter, S., Jeffery, E. J., Dreizler, S., Schuh, S. L., Giovanni, M., Edelmann, H., Rigby, J., and Bronowska, A. (2003). Discovery of A New Class of Pulsating Stars: Gravity-Mode Pulsators among Subdwarf B Stars. *ApJ Letter*, 583:L31–L34.

Green, E. M., Guvenen, B., O'Malley, C. J., O'Connell, C. J., Baringer, B. P., Villareal, A. S., Carleton, T. M., Fontaine, G., Brassard, P., and Charpinet, S. (2011). The Unusual Variable Hot B Subdwarf LS IV-14 deg 116. *ApJ*, 734:59.

Green, R. F., Schmidt, M., and Liebert, J. (1986). The Palomar-Green catalog of ultraviolet-excess stellar objects. *ApJ, Supplement*, 61:305–352.

Greenstein, J. L. and Sargent, A. I. (1974). The Nature of Faint Blue Stars in the Halo. II. *ApJ Supplement*, 28:157.

Guzik, J. A., Kaye, A. B., Bradley, P. A., Cox, A. N., and Neuforge, C. (2000). Driving the Gravity-Mode Pulsations in γ Doradus Variables. *ApJ*, 542(1):L57–L60.

Han, Z., Podsiadlowski, P., Maxted, P. F. L., and Marsh, T. R. (2003). The origin of subdwarf B stars - II. *MNRAS*, 341(2):669–691.

Han, Z., Podsiadlowski, P., Maxted, P. F. L., Marsh, T. R., and Ivanova, N. (2002). The origin of subdwarf B stars - I. The formation channels. *MNRAS*, 336:449–466.

Heber, U. (2009). Hot Subdwarf Stars. *Annual Review of Astron and Astrophys*, 47:211–251.

Heber, U. (2016). Hot Subluminous Stars. *ASP*, 128(8):082001.

Heber, U., Kudritzki, R. P., Caloi, V., Castellani, V., and Danziger, J. (1986). A spectroscopic study of HB stars in the galactic globular cluster NGC 6752. *A&A*, 162:171–179.

Hu, H., Dupret, M. A., Aerts, C., Nelemans, G., Kawaler, S. D., Miglio, A., Montalban, J., and Scuflaire, R. (2008). A seismic approach to testing different formation channels of subdwarf B stars. *A&A*, 490(1):243–252.

Hu, H., Glebbeek, E., Thoul, A. A., Dupret, M.-A., Stancliffe, R. J., Nelemans, G., and Aerts, C. (2010). Gravitational settling in pulsating subdwarf B stars and their progenitors. *A&A*, 511:A87.

Humason, M. L. and Zwicky, F. (1947). A Search for Faint Blue Stars. *ApJ, Supplement*, 105:85.

Hurley, J. R., Tout, C. A., and Pols, O. R. (2002). Evolution of binary stars and the effect of tides on binary populations. *MNRAS*, 329:897–928.

Iben, I. (1968). Age and Initial Helium Abundance of Stars in the Globular Cluster M15. *Nature*, 220(5163):143–146.

Iglesias, C. A. and Rogers, F. J. (1996). Updated Opal Opacities. *ApJ*, 464:943.

Ivanova, N. et al. (2013). Common Envelope Evolution: Where we stand and how we can move forward. *Astron. Astrophys. Rev.*, 21:59.

Izzard, R. G., Preece, H., Jofre, P., Halabi, G. M., Masseron, T., and Tout, C. A. (2018). Binary stars in the Galactic thick disc. *MNRAS*, 473:2984–2999.

Izzard, R. G., Tout, C. A., Karakas, A. I., and Pols, O. R. (2004). A new synthetic model for asymptotic giant branch stars. *MNRAS*, 350:407–426.

Jeffery, C. S. (2008). The impact of asteroseismology on the theory of stellar evolution. *Communications in Asteroseismology*, 157:240–248.

Jeffery, C. S. and Saio, H. (2006). Fe-bump instability: the excitation of pulsations in subdwarf B and other low-mass stars. *MNRAS*, 371:659–672.

Jeffery, C. S. and Saio, H. (2007). Improved opacities and pulsation stability in subluminous B and O stars. *MNRAS*, 378:379–383.

Kawaler, S. D., Reed, M. D., Østensen, R. H., Bloemen, S., Kurtz, D. W., Quint, A. C., Silvotti, R., Baran, A. S., Green, E. M., Charpinet, S., Telting, J., Aerts, C., Handler, G., Kjeldsen, H., Christensen-Dalsgaard, J., Borucki, W. J., and Koch, D. G. (2010). First Kepler results on compact pulsators - V. Slowly pulsating subdwarf B stars in short-period binaries. *MNRAS*, 409:1509–1517.

Kilkenny, D., Koen, C., O'Donoghue, D., and Stobie, R. S. (1997). A new class of rapidly pulsating star - I. EC 14026-2647, the class prototype. *MNRAS*, 285:640–644.

Koen, C., Orosz, J. A., and Wade, R. A. (1998). KPD 0422+5421: a new short-period subdwarf B/white dwarf binary. *MNRAS*, 300:695–704.

Kopal, Z., editor (1989). *The Roche problem and its significance for double-star astronomy*, volume 152 of *Astrophysics and Space Science Library*.

Kudritzki, R. P. and Simon, K. P. (1978). Non-LTE analysis of subluminous O-star. The hydrogen-deficient subdwarf O-binary HD 49798. *A&A*, 70:653–663.

Kuiper, G. P. (1941). On the Interpretation of β Lyrae and Other Close Binaries. *ApJ*, 93:133.

Kupfer, T., Geier, S., Heber, U., Østensen, R. H., Barlow, B. N., Maxted, P. F. L., Heuser, C., Schaffenroth, V., and Gänsicke, B. T. (2015a). Hot subdwarf binaries from the MUCHFUSS project. Analysis of 12 new systems and a study of the short-period binary population. *A&A*, 576:A44.

Kupfer, T., Geier, S., Heber, U., Østensen, R. H., Barlow, B. N., Maxted, P. F. L., Heuser, C., Schaffenroth, V., and Gänsicke, B. T. (2015b). Hot subdwarf binaries from the MUCHFUSS project. Analysis of 12 new systems and a study of the short-period binary population. *A&A*, 576:A44.

Latour, M., Dorsch, M., and Heber, U. (2019). Heavy metal enrichment in the intermediate He-sdOB pulsator Feige 46. *A&A*, 629:A148.

Latour, M., Fontaine, G., and Green, E. (2014). Updates on the Pulsating sdB Star Feige 48 through Spectroscopy. In van Grootel, V., Green, E., Fontaine, G., and Charpinet, S., editors, *6th Meeting on Hot Subdwarf Stars and Related Objects*, volume 481 of *Astronomical Society of the Pacific Conference Series*, page 91.

Ledoux, P. (1947). Stellar Models with Convection and with Discontinuity of the Mean Molecular Weight. *ApJ*, 105:305.

Ledoux, P. (1951). The Nonradial Oscillations of Gaseous Stars and the Problem of Beta Canis Majoris. *ApJ*, 114:373.

Maxted, P. F. L., Marsh, T. R., Heber, U., Morales-Rueda, L., North, R. C., and Lawson, W. A. (2002). Photometry of four binary subdwarf B stars and the nature of their unseen companion stars. *MNRAS*, 333:231–240.

Miller Bertolami, M. M., Córsico, A. H., and Althaus, L. G. (2011). On the Challenging Variability of LS IV-14°116: Pulsational Instabilities Excited by the epsilon-Mechanism. *ApJ Letter*, 741(1):L3.

Moe, M. and Di Stefano, R. (2017). Mind Your Ps and Qs: The Interrelation between Period (P) and Mass-ratio (Q) Distributions of Binary Stars. *ApJ Supplement*, 230(2):15.

Mosser, B., Goupil, M. J., Belkacem, K., Marques, J. P., Beck, P. G., Bloemen, S., De Ridder, J., Barban, C., Deheuvels, S., Elsworth, Y., Hekker, S., Kallinger, T., Ouazzani, R. M., Pinsonneault, M., Samadi, R., Stello, D., García, R. A., Klaus, T. C., Li, J., Mathur, S., and Morris, R. L. (2012). Spin down of the core rotation in red giants. *A&A*, 548:A10.

Napiwotzki, R., Karl, C. A., Lisker, T., Heber, U., Christlieb, N., Reimers, D., Nelemans, G., and Homeier, D. (2004). Close binary EHB stars from SPY. *Astrophysics and Space Science*, 291:321–328.

Nugis, T. and Lamers, H. J. G. L. M. (2000). Mass-loss rates of Wolf-Rayet stars as a function of stellar parameters. *A&A*, 360:227–244.

Østensen, R. H., Silvotti, R., Charpinet, S., Oreiro, R., Handler, G., Green, E. M., Bloemen, S., Heber, U., Gänsicke, B. T., Marsh, T. R., Kurtz, D. W., Telting, J. H., Reed, M. D., Kawaler, S. D., Aerts, C., Rodríguez-López, C., Vučković, M., Ottosen, T. A., Liimets, T., Quint, A. C., Van Grootel, V., Randall, S. K., Gilliland, R. L., Kjeldsen, H., Christensen-Dalsgaard, J., Borucki, W. J., Koch, D., and Quintana, E. V. (2010). First Kepler results on compact pulsators - I. Survey target selection and the first pulsators. *MNRAS*, 409:1470–1486.

Østensen, R. H., Telting, J. H., Reed, M. D., Baran, A. S., Nemeth, P., and Kiaeerad, F. (2014). Asteroseismology revealing trapped modes in KIC 10553698A. *A&A*, 569:A15.

O'Toole, S. J., Heber, U., and Benjamin, R. A. (2004). Detection of a companion to the pulsating sdB Feige 48. *A&A*, 422:1053–1058.

Pablo, H., Kawaler, S. D., and Green, E. M. (2012a). Exploring B4: A Pulsating sdB Star, in a Binary, in the Open Cluster NGC 6791. *ApJ Letters*, 750:L26.

Pablo, H., Kawaler, S. D., Reed, M. D., Bloemen, S., Charpinet, S., Hu, H., Telting, J., Østensen, R. H., Baran, A. S., Green, E. M., Hermes, J. J., Barclay, T., O'Toole, S. J., Mullally, F., Kurtz, D. W., Christensen-Dalsgaard, J., Caldwell, D. A., Christiansen, J. L., and Kinemuchi, K. (2012b). Seismic evidence for non-synchronization in two close sdb+dM binaries from Kepler photometry. *MNRAS*, 422:1343–1351.

Pablo, H. W. (2012). *Formation and tidal synchronization of sdB stars in binaries an asteroseismic investigation using Kepler Observations*. PhD thesis, Iowa State University.

Paxton, B., Bildsten, L., Dotter, A., Herwig, F., Lesaffre, P., and Timmes, F. (2011). Modules for Experiments in Stellar Astrophysics (MESA). *ApJ, Supplement*, 192:3.

Paxton, B., Cantiello, M., Arras, P., Bildsten, L., Brown, E. F., Dotter, A., Mankovich, C., Montgomery, M. H., Stello, D., Timmes, F. X., and Townsend, R. (2013). Modules for Experiments in Stellar Astrophysics (MESA): Planets, Oscillations, Rotation, and Massive Stars. *ApJ, Supplement*, 208:4.

Paxton, B., Schwab, J., Bauer, E. B., Bildsten, L., Blinnikov, S., Duffell, P., Farmer, R., Goldberg, J. A., Marchant, P., Sorokina, E., Thoul, A., Townsend, R. H. D., and Timmes, F. X. (2018). Modules for Experiments in Stellar Astrophysics (MESA): Convective Boundaries, Element Diffusion, and Massive Star Explosions. *ApJ*, 234:34.

Penev, K., Sasselov, D., Robinson, F., and Demarque, P. (2007). On Dissipation inside Turbulent Convection Zones from Three-dimensional Simulations of Solar Convection. *ApJ*, 655:1166–1171.

Pesnell, W. D. (1987). A new driving mechanism for stellar pulsations. *ApJ*, 314:598–604.

Piersanti, L., Tornambé, A., and Castellani, V. (2004). Zero-age horizontal branch structures: pseudo versus fully evolutionary models. *MNRAS*, 353(1):243–248.

Pols, O. R., Schröder, K.-P., Hurley, J. R., Tout, C. A., and Eggleton, P. P. (1998). Stellar evolution models for Z = 0.0001 to 0.03. *MNRAS*, 298:525–536.

Pols, O. R., Tout, C. A., Eggleton, P. P., and Han, Z. (1995). Approximate input physics for stellar modelling. *MNRAS*, 274:964–974.

Preece, H. P., Tout, C. A., and Jeffery, C. S. (2018). Tidal Interactions of Close Hot Subdwarf Binaries. *MNRAS*, 481:715–726.

Preece, H. P., Tout, C. A., and Jeffery, C. S. (2019). Convection physics and tidal synchronization of the subdwarf binary NY Virginis. *MNRAS*, 485(2):2889–2894.

Reed, M. D., Baran, A. S., Østensen, R. H., Telting, J. H., Kern, J. W., Bloemen, S., Blay, P., Pursimo, T., Kuutma, T., Slumstrup, D., Saajasto, M., Nielsen, L. D., Harmanen, J., Winans, A. J., Foster, H. M., and Rowe, L. (2016). A pulsation analysis of K2 observations of the subdwarf B star PG 1142-037 during Campaign 1: A subsynchronously rotating ellipsoidal variable. *MNRAS*, 458:1417–1426.

Reimers, D. (1975a). Circumstellar absorption lines and mass loss from red giants. *Memoires of the Societe Royale des Sciences de Liege*, 8:369–382.

Reimers, D. (1975b). Circumstellar absorption lines and mass loss from red giants. *Memoires of the Societe Royale des Sciences de Liege*, 8:369–382.

Reimers, D. (1977). On the absolute scale of mass-loss in red giants. I - Circumstellar absorption lines in the spectrum of the visual companion of Alpha-1 HER. *A&A*, 61:217–224.

Reyniers, K. and Smeyers, P. (2003). Tidal perturbations of linear, isentropic oscillations in components of circular-orbit close binaries. I. Synchronously rotating components. *A&A*, 404:1051–1065.

Rieutord, M. and Zahn, J.-P. (1997). Ekman Pumping and Tidal Dissipation in Close Binaries: A Refutation of Tassoul's Mechanism. *ApJ*, 474:760–767.

Rosseland, S. and Randers, G. (1938). On the Stability of Pulsating Stars. *Astrophysica Norvegica*, 3:71.

Saio, H. (1981). Rotational and tidal perturbations of nonradial oscillations in a polytropic star. *ApJ*, 244:299–315.

Saio, H. and Jeffery, C. S. (2019). The excitation of g-mode pulsations in hot helium-rich subdwarfs. *MNRAS*, 482(1):758–761.

Sargent, W. L. W. and Searle, L. (1968). A Quantitative Description of the Spectra of the Brighter Feige Stars. *ApJ*, 152:443.

Schaffenroth, V., Barlow, B., Geier, S., Vučković, M., Kilkenny, D., and Schaffenroth, J. (2017). News From The Erebos Project. *Open Astronomy*, 26(1):208–213.

Schaffenroth, V., Geier, S., Heber, U., Kupfer, T., Ziegerer, E., Heuser, C., Classen, L., and Cordes, O. (2014). Binaries discovered by the MUCHFUSS project. SDSS J162256.66+473051.1: An eclipsing subdwarf B binary with a brown dwarf companion. *A&A*, 564:A98.

Schindler, J.-T., Green, E. M., and Arnett, W. D. (2015). Exploring Stellar Evolution Models of sdB Stars using MESA. *ApJ*, 806:178.

Schröder, K.-P., Pols, O. R., and Eggleton, P. P. (1997). A critical test of stellar evolution and convective core 'overshooting' by means of zeta Aurigae systems. *MNRAS*, 285:696–710.

Schwarzschild, M. (1958). *Structure and evolution of the stars.*

Schwarzschild, M. and Härm, R. (1958). Evolution of Very Massive Stars. *ApJ*, 128:348.

Song, H. F., Zhong, Z., and Lu, Y. (2009). Structure and evolution of rotationally and tidally distorted stars. *A&A*, 504:161–170.

Stancliffe, R. J. and Eldridge, J. J. (2009). Modelling the binary progenitor of Supernova 1993J. *MNRAS*, 396:1699–1708.

Tassoul, J.-L. (1987). On synchronization in early-type binaries. *ApJ*, 322:856–861.

Tassoul, J.-L. and Tassoul, M. (1992). A comparative study of synchronization and circularization in close binaries. *ApJ*, 395:259–267.

Telting, J. H., Baran, A. S., Nemeth, P., Østensen, R. H., Kupfer, T., Macfarlane, S., Heber, U., Aerts, C., and Geier, S. (2014). KIC 7668647: a 14 day beaming sdB+WD binary with a pulsating subdwarf. *A&A*, 570:A129.

Tout, C. A., Wickramasinghe, D. T., Liebert, J., Ferrario, L., and Pringle, J. E. (2008). Binary star origin of high field magnetic white dwarfs. *MNRAS*, 387(2):897–901.

Townsend, R. H. D., Goldstein, J., and Zweibel, E. G. (2018). Angular momentum transport by heat-driven g-modes in slowly pulsating B stars. *MNRAS*, 475:879–893.

Townsend, R. H. D. and Teitler, S. A. (2013). GYRE: an open-source stellar oscillation code based on a new Magnus Multiple Shooting scheme. *MNRAS*, 435:3406–3418.

Van Grootel, V., Charpinet, S., Brassard, P., Fontaine, G., and Green, E. M. (2013). Third generation stellar models for asteroseismology of hot B subdwarf stars. A test of accuracy with the pulsating eclipsing binary PG 1336-018. *A&A*, 553:A97.

Van Grootel, V., Charpinet, S., Fontaine, G., and Brassard, P. (2008). Asteroseismology in action: a test of spin-orbit synchronism in the close binary system Feige 48. *A&A*, 483:875–885.

Van Grootel, V., Charpinet, S., Fontaine, G., Brassard, P., Green, E. M., Randall, S. K., Silvotti, R., Østensen, R. H., Kjeldsen, H., Christensen-Dalsgaard, J., Borucki, W. J., and Koch, D. (2010a). Early Asteroseismic Results from Kepler: Structural and Core Parameters of the Hot B Subdwarf KPD 1943+4058 as Inferred from g-mode Oscillations. *ApJ, Letters*, 718:L97–L101.

Van Grootel, V., Charpinet, S., Fontaine, G., Green, E. M., and Brassard, P. (2010b). Structural and core parameters of the hot B subdwarf KPD 0629-0016 from CoRoT g-mode asteroseismology. *A&A*, 524:A63.

Vassiliadis, E. and Wood, P. R. (1993). Evolution of low- and intermediate-mass stars to the end of the asymptotic giant branch with mass loss. *ApJ*, 41:641–657.

Vennes, S., Kawka, A., and Németh, P. (2011). A selection of hot subluminous stars in the GALEX survey - I. Correlation with the Guide Star Catalog. *MNRAS*, 410:2095–2112.

Vennes, S., Kawka, A., O'Toole, S. J., Németh, P., and Burton, D. (2012). The Shortest Period sdB Plus White Dwarf Binary CD-30 11223 (GALEX J1411-3053). *ApJ Letters*, 759:L25.

Vos, J., Vučković, M., Chen, X., Han, Z., Boudreaux, T., Barlow, B. N., Østensen, R., and Németh, P. (2019a). The orbital period-mass ratio relation of wide sdB+MS binaries and its application to the stability of RLOF. *MNRAS*, 482(4):4592–4605.

Vos, J., Vučković, M., Chen, X., Han, Z., Boudreaux, T., Barlow, B. N., Østensen, R., and Németh, P. (2019b). Using wide hot subdwarf binaries to constrain Roche-lobe overflow models. *Contributions of the Astronomical Observatory Skalnate Pleso*, 49(2):264–270.

Vučković, M., Aerts, C., Östensen, R., Nelemans, G., Hu, H., Jeffery, C. S., Dhillon, V. S., and Marsh, T. R. (2007). The binary properties of the pulsating subdwarf B eclipsing binary <ASTROBJ>PG 1336-018</ASTROBJ> (NY Virginis). *A&A*, 471:605–615.

Zahn, J. P. (1966). Les marées dans une étoile double serrée (suite). *Annales d'Astrophysique*, 29:489.

Zahn, J.-P. (1975). The dynamical tide in close binaries. *A&A*, 41:329–344.

Zahn, J.-P. (1977). Tidal friction in close binary stars. *A&A*, 57:383–394.

Zahn, J. P. (2008). Tidal dissipation in binary systems. In Goupil, M. J. and Zahn, J. P., editors, *EAS Publications Series*, volume 29 of *EAS Publications Series*, pages 67–90.

Zhang, X. and Jeffery, C. S. (2012). Evolutionary models for double helium white dwarf mergers and the formation of helium-rich hot subdwarfs. *MNRAS*, 419:452–464.